

11-9-2021

Challenges of Inductive Electric Vehicle Charging Systems in both Stationary and Dynamic Modes

Hassan Jafari Mr

Florida International University, hjafa002@fiu.edu

Follow this and additional works at: <https://digitalcommons.fiu.edu/etd>



Part of the [Power and Energy Commons](#)

Recommended Citation

Jafari, Hassan Mr, "Challenges of Inductive Electric Vehicle Charging Systems in both Stationary and Dynamic Modes" (2021). *FIU Electronic Theses and Dissertations*. 4895.

<https://digitalcommons.fiu.edu/etd/4895>

This work is brought to you for free and open access by the University Graduate School at FIU Digital Commons. It has been accepted for inclusion in FIU Electronic Theses and Dissertations by an authorized administrator of FIU Digital Commons. For more information, please contact dcc@fiu.edu.

FLORIDA INTERNATIONAL UNIVERSITY

Miami, Florida

CHALLENGES OF INDUCTIVE ELECTRIC VEHICLE CHARGING
SYSTEMS IN STATIONARY AND DYNAMIC OPERATIONAL MODES

A dissertation submitted in partial fulfillment of the
requirements for the degree of

DOCTOR OF PHILOSOPHY

in

ELECTRICAL AND COMPUTER ENGINEERING

by

Hassan Jafari

2021

To: Dean John L. Volakis
College of Engineering and Computing

This dissertation, written by Hassan Jafari, and entitled Challenges of Inductive Electric Vehicle Charging Systems in Stationary and Dynamic Operational Modes, having been approved in respect to style and intellectual content, is referred to you for judgment.

We have read this dissertation and recommend that it be approved.

Osama Mohammad

Jean Andrian

Nezih Pala

Priyanka Alluri

Arif I. Sarwat, Major Professor

Date of Defense: November 9, 2021

The dissertation of Hassan Jafari is approved.

Dean John L. Volakis
College of Engineering and Computing

Andrés G. Gil
Vice President for Research and Economic Development
and Dean of the University Graduate School

Florida International University, 2021

© Copyright 2021 by Hassan Jafari

All rights reserved.

DEDICATION

To the dearest person of my life Maryam (my wife),

To my mother Rakhshandeh,

To my father Mahdi,

Who have devoted their lives for me to reach where I am standing now.

ACKNOWLEDGMENTS

I would like to express my sincere gratitude to my advisor Dr. Arif Sarwat for his continuous support of my Ph.D study and related research, for his patience, and motivation. Besides my advisor, I would like to thank the rest of my thesis committee: tric Vehicle Charging Systems in St Dr. Osama Mohammed, Dr. Jean Andrian, Dr. Nezhil Pala, and Dr. Priyanka Alluri, for their insightful comments and encouragement to widen my research from various perspectives. This dissertation was supported by the National Science Foundation under grant number 1541108 and FIU Graduate School Dissertation Year Fellowship (DYF).

ABSTRACT OF THE DISSERTATION
CHALLENGES OF INDUCTIVE ELECTRIC VEHICLE CHARGING
SYSTEMS IN STATIONARY AND DYNAMIC OPERATIONAL MODES

by

Hassan Jafari

Florida International University, 2021

Miami, Florida

Professor Arif I. Sarwat, Major Professor

Inductive power transfer as an emerging technology has become applicable in wide power ranges including Electric Vehicle, Electric Aircraft, wheelchair, cellphone, scooter and so on. Among them, inductive Electric Vehicle (EV) charging has gained great interest in the last decade due to many merits namely contactless technology, more convenience, full automotive charging process. However, inductive EV charging systems could bring about so many issues and concerns which are addressed in this dissertation. One of the critical challenges addressed in this dissertation is a virtual inertia based IPT controller to prevent the undesirable dynamics imposed by the EVs increasing number in the grid. Another adverse issue solved in this dissertation is detecting any metal object intrusions into the charging zone to the Inductive Power Transfer (IPT) systems before leading to heat generation on the metal or risk of fire.

Moreover, in this dissertation, a new self-controlled multi-power level IPT controller is developed that enables EV charging level regulation in a wide range of power; suitable for different applications from golf-cart charging system (light duty EV) to truck (heavy duty EV). The proposed controller has many merits including easy to be implemented, cost-effective, and the least complexities compared to conventional PWM methods. Additionally, in this dissertation, the online estimation of IPT parameters using primary measurement including coupling factor, battery current and battery voltage is introduced; the developed method can

find immediate applications for the development of adaptive controllers for static and dynamic inductive charging systems. Finally, the last objective of this research is physics-based design optimization techniques for the magnetic structures of inductive EV charging systems for dynamic application (getting charged while in motion). New configuration of IPT transmitting couplers with objective of high-power density, low power loss, low cost and less electromagnetic emission are designed and developed in the lab.

TABLE OF CONTENTS

CHAPTER	PAGE
1. INTRODUCTION	1
1.1 Motivation	1
1.2 General Statement of Problem Area	1
2. Foreign Object Detection in Inductive Charging Systems Based on Primary Side Measurements	6
2.1 Introduction	6
2.2 Theoretical Formulation of Proposed Methodology	7
2.3 Simulation Results and Analysis	9
2.3.1 Foreign Object Intrusion and Detection	10
2.3.2 Misalignment of Transmitter and Receiver Pads	12
2.4 discrimination of FOD and misalignment	12
2.5 Conclusion	14
2.6 Introduction	14
2.7 FEA analysis of conductive foreign Object intrusion in IPT Systems . .	17
2.8 theoretical analysis for the proposed FOD Method	18
2.8.1 FEA Analysis for Magnetic/Non-magnetic Conductive Object	26
2.8.2 Foreign Object Detection At Standby Mode	26
2.8.3 IPT-System Losses In Standby Mode	27
2.8.4 Online Foreign Object Detection In IPT Operational Mode	27
2.9 Discrimination Of FOI From Misalignment	28
2.10 Speed analysis of the proposed FOD method	31
2.11 Experimental Analysis	33
2.11.1 Verification Of The Proposed FOD Method For Two Case Studies: 5-Cent Coin And Beverage Can	33
2.11.2 Experimental Verification For Discrimination of FOI From Misalign- ment	35
2.11.3 Experimental Verification of the Proposed FOD Method For Standby Mode	37
2.12 Summary	39
3. Virtual Inertia-Based Multi-Power Level Controller for Inductive Electric Vehicle Charging Systems	41
3.1 Introduction	41
3.2 Power-Frequency Model Formulation	44
3.3 IPT multi-power level resonant controller	45
3.3.1 Control Logic Design	47
3.3.2 Switching control Logic	49
3.3.3 Fundamental Harmonic Analysis of converter's Voltage	52
3.4 Circular IPT Case Study	54
3.5 Simulation Analysis	55
3.6 Experimental Analysis	57
3.6.1 VIC Implementation on IPT Multi-power Level charger	61

3.6.2	Case1: The grid frequency decreases From $f = 60z$ (Normal) to $f = 58.38z$	63
3.6.3	Case2: The grid frequency increases from $f = 60z$ (normal) to $f = 61.22z$	64
3.7	efficiency analysis of the proposed multi-power level IPT system	66
3.8	Summary	67
4.	AC-AC Matrix Converter for Inductive Power Transfer Systems	69
4.1	Switching control Logic	70
4.1.1	Fundamental Harmonic Analysis of converter's Voltage	72
4.2	Simulation Analysis	76
4.3	Experimental Validation for the multi-power level controller with Zero states	77
4.4	Summary	79
5.	An Accurate Online Parameter Estimation Technique for Inductive Electric Vehicle Charging Systems	81
5.1	Introduction	81
5.1.1	Magnetic Coupling Coefficient Estimation	84
5.1.2	Battery Charging Current Estimation	85
5.1.3	Battery Voltage Estimation	86
5.2	Simulation Analysis	88
5.3	Experimental Analysis	89
5.4	Conclusions	89
6.	Comparison Analysis of Bipolar and Double D-shape Configurations in Inductive Power Transfer Electric Vehicle Chargers	91
6.1	Introduction	91
6.2	Power transfer calculation	93
6.3	Comparison of performance of BPP and DD couplers	95
6.3.1	EMC comparison of DD and BPP couplers	95
6.3.2	Electromagnetic characteristics comparison of DD and BPP	98
6.4	Summary	99
7.	Optimal Design of IPT Bipolar Power Pad for Roadway-Powered EV Charging Systems	100
7.1	Introduction	100
7.2	Power Calculation in double coils IPT systems	102
7.3	Multi-Objective Design of BPP coupler for dynamic IPT systems	104
7.3.1	Objective Functions of MOOP	104
7.3.2	Cost function	106
7.3.3	Horizontal Misalignment Tolerance	107
7.3.4	MOOP Constraints	107
7.4	MOOP Implementation	108
7.5	Validation of the proposed Algorithm	111
7.6	Dynamic IPT system based on "POS-6" arameters	115

7.7	Multi-Level Power Controller Design for Dynamic Wireless Electric Vehicle Charging Systems	116
7.8	Finite Element Analysis(FEA) for DWPT	117
7.9	Proposed Control Methodology based on resonant current discretization	119
7.9.1	Control Logic Design	120
7.9.2	Matrix Converter power controller logic	121
7.9.3	output power Calculation for IPT as function of selected level	122
7.10	Simulation and Result Analysis	122
7.11	summary	124
8.	FPGA-Based IPT power Controller	126
8.1	Introduction	126
8.2	Multi-Level Power level controller for AC-AC Matrix Converter	127
8.2.1	Resonant Frequency-based Power controller Design	128
8.2.2	Switching logic	130
8.3	Power and Voltage Calculation using Fundamental Harmonic Analysis .	132
8.4	Experimental Validation for the multi-power level controller with Zero states	136
8.5	efficiency analysis of the proposed multi-power level IPT system	142
8.6	summary	143
9.	CONCLUSIONS AND FUTURE WORK	144
9.1	Future Works	147
VITA	172

LIST OF FIGURES

FIGURE	PAGE
1.1 The Dynamic wireless power system for EV charging systems.	2
1.2 Proposed Multi-power level controller for dynamic inductive electric vehicle charging using estimated position	4
2.1 Schematic diagram of the simulated IPT system	7
2.2 3D Model of the studies IPT system for Misalignment and FOI	7
2.3 FOI and Detection (a) Primary/Secondary Self Inductance (b) Mutual Inductance (c) resonance frequency (d) Frequency Deviation	8
2.4 Misalignment between transmitter and receiver pads (a) Primary/Secondary Self Inductance (b) Mutual Inductance (c) resonance frequency (d) Frequency Deviation	11
2.5 Resonant RMS current during normal conditions, misalignment and FOD maximum frequency deviation of 8Hz	13
2.6 Resonant RMS current during normal conditions, misalignment and FOD maximum frequency deviation of 74Hz	13
2.7 Schematic diagram of the IPT system.	15
2.8 2D FEA analysis: (a) magnetic flux density without object presence, (b) magnetic flux density with the presence of conductive object.	18
2.9 FOD and Detection (a) Mutual Inductance (b) Primary Self Inductance (c) Secondary Self Inductance (d) Frequency Deviation.	19
2.10 3D electromagnetic model of IPT system.	21
2.11 distribution of flux density on the primary pad.	21
2.12 loss effect of high frequency electromagnetic field on ferrit bars	21
2.13 Primary/secondary self-inductances (L_p)/ (L_s), mutual-inductance (M) as a function of foreign object location with respect to primary pad center.	23
2.14 3D plot of resonance frequency as function of foreign object location respect to primary pad center.	23
2.15 Proposed IPT system with consideration of low lower AC/DC rectifier to provide DC link for FOD purpose in the standby mode.	23
2.16 FEA analysis for aluminum and iron foreign objects(a) Primary self-inductance (L_P) distortion for two different material of FOI(b) Resonance frequency deviation for two different material of FOI.	24
2.17 Misalignment between transmitter and receiver pads (a) Mutual Inductance (b) Primary Self Inductance (c) Secondary Self Inductance (d) Frequency Deviation.	25

2.18	Flowchart for FOI and misalignment identification.	29
2.19	Resonant RMS current during normal conditions, misalignment and FOD maximum frequency deviation of 8Hz.	30
2.20	Resonant RMS current during normal conditions, misalignment and FOD maximum frequency deviation of 672Hz.	30
2.21	Inductive Power Transfer Experimental set-up.	32
2.22	Experimental results achieved by the proposed FOD method(a) 5-cent coin (49% detection area) with 200 ms sampling time (b) Beverage can (with 82% detection area) with 10 ms sampling time.	34
2.23	The plot of the detection area as function of detection speed for two tested foreign objects.	34
2.24	Primary and secondary currents when there is no misalignment/ no FOI.	35
2.25	Discrimination of FOI from misalignment (a) Primary/secondary resonance currents when the new resonant frequency caused by both cases is about 34.77 kHz (b) Primary/secondary resonance currents when the new resonant frequency caused by both cases is about 34.85 kHz (c) Primary/secondary resonance currents when the new resonant frequency caused by both cases is about 35.087 kHz (d) Primary/secondary resonance currents when the new resonant frequency caused by both cases is about 35.2 kHz.	36
2.26	Experimental results for larger size foreign objects(a) Primary/secondary resonance currents when the new resonant frequency caused by FOI is about 36.033 kHz (b) Primary/secondary resonance currents when the new resonant frequency caused by FOI is about 37.306 kHz.	38
2.27	Primary side DC Link current and voltage (standby mode Consumption).	38
2.28	Primary resonance current (i_r) along with switching signal of converter (S_A) with/without foreign conductive objects.	39
3.1	Representation of the VIC concept in an inductive EV charging system.	42
3.2	The flowchart of the virtual inertia based IPT power controller	45
3.3	The proposed VIC for inductive EV charger.	46
3.4	Reference CLK (used as the clock signal for the first D-type flip-flop), and inverted outputs: $\overline{Q_A}, \overline{Q_B}, \overline{Q_C}$ of three cascaded flip-flops (see Fig. 3.3)	48
3.5	Reference signals with 1 to 8 pulses obtained using $A, B,$ and C (for more details refer to Table 3.1)	49
3.6	IPT's primary resonant current path for six operation modes (referring to Table 3.3)	51

3.7	Geometrical parameter of ferrite bars, coil, and shield plate in the circular power pad	52
3.8	2D-FEA Model: Magnetic plot of the IPT system	53
3.9	Simulation Model: synchronous generator with enabled AGC along with inductive charging systems and load	54
3.10	Simulation results: Grid frequency (f), power deviation(ΔP), IPT power level	55
3.11	Virtual inertia response of the proposed IPT to power grid dynamics with various inertia Constants.	56
3.12	Experimental setup: Inductive Power Transfer connected to an Lab-Volt grid emulator which is comprised of synchronous generator, RL loads.	57
3.13	power transfer level (a) level 2(b) level 3 (c) level 4 (d) level 5	58
3.14	power transfer in different level (a) level 6 (b) level 7 (c) level 8 (d) level 9	59
3.15	Power transfer level (a) level 10 (b) level 11(c) level 12(d) level 13	60
3.16	power transfer level (a) L= 14(b) L= 15 (c) L= 16	60
3.17	Frequency deviation VS the IPT power level number ($1\% < SOC < 99\%$)	61
3.18	Battery power change in response to grid frequency fall using the VIC-based inductive charger.	63
3.19	Battery power change in response to grid frequency rise using the VIC-based inductive charger.	63
3.20	Grid-to-Battery efficiency analysis of IPT in different power level (L) is (a)L=10 (b) L=11 (c) L=12 (d) L=13 (e) L=14 (f) L=15	65
3.21	Efficiency plots at different power transfer levels	66
4.1	Schematic: AC-AC matrix converter for IPT system	70
4.2	IPT's primary resonant current path for six operation modes when ac supply voltage is in positive half cycle (V_{ac})	71
4.3	when ac supply voltage is positive ($V_{ac} > 0$)	72
4.4	when ac supply voltage is negative ($V_{ac} < 0$)	72
4.5	a) Converter's conduction phase (α) b) reference power change (P_{ref}) c) IPT's instantaneous Power ($P_{ints.}$) d) Averaged IPT power over 60 Hz time period ($P_{Ave.}$)	74
4.6	a) v_{ac} b) Resonant Current (I_{res}) c) Grid Current (I_{grid})	74

4.7	plots of I_r , V_{out} , and switching signals for few cycles around the $point_1$ as marked in Fig. 4.5	75
4.8	plots of I_r , V_{out} , and switching signals for few cycles around the $point_2$ as marked in Fig. 4.5	75
4.9	plots of I_r , V_{out} , and switching signals for few cycles around the $point_3$ as marked in Fig. 4.5	77
4.10	Experimental result for switching signals (SW1 and SW4), resonant current and converter output voltage when input AC voltage are positive	78
4.11	Experimental result for switching signals(SW2 and SW3), resonant current and converter output voltage when input AC voltage are positive	78
5.1	A typical Series-Series IPT system	82
5.2	Series-compensated inductive charging system: equivalent circuit and corresponding variables.	83
5.3	A conceptual plot of the resonant current, capacitor voltage and corresponding analytical formulations.	84
5.4	The flowchart of the developed parameter estimation method based analytical formulations.	85
5.5	The simulation results of the developed parameter estimation method	86
5.6	The experimental setup of the inductive charging system prototype with online parameter estimation functionality.	87
5.7	The estimated coupling factor and battery charging current while the airgap is reduced for 10.5 seconds.	88
6.1	The conceptual schematic of IPT roadway-powered track for dynamic EV charging system	92
6.2	IPT systems consists of two primary couplers (TX1, and TX2) and two secondary couplers (RX1, and RX2)	93
6.3	Simplified IPT circuit for double couplers configuration using FHA method	94
6.4	3D-FEA model of 2 (a) DD (b) BPP Coupler	96
6.5	Magnetic flux density in 0.4m distance (a) BPP (b) DD Couplers	96
6.6	Magnetic flux density distribution along Line2 (a) DD (b) BPP Coupler	97
6.7	Parametric analysis for DD and BPP couplers when the misalignment of transmitter and receiver pads are varied from -200mm to 200mm (a) Coupling Factor(%) (b) Mutual Inductance(μ H)	97

6.8	Parametric analysis for DD and BPP couplers when the misalignment of transmitter and receiver pads are varied from -200mm to 200mm (a) Open Circuit Voltage of RX1 and RX2 (b) Short Circuit Current(I_{sc}) (c) Uncompensated Power (P_{su}) (KW)	98
7.1	The conceptual schematic of IPT roadway-powered track for dynamic EV charging system	101
7.2	IPT systems consists of two primary couplers (TX1, and TX2) and two secondary couplers (RX1, and RX2)	102
7.3	Simplified IPT circuit using FHA method	102
7.4	BPP 3-D FEA model with all the defined parameters	104
7.5	The proposed multi-objective time-harmonic algorithm using co-simulation of FEMM software and MATLAB	108
7.6	3D-plot of objective function values of all the solutions along with Pareto optimal solutions	110
7.7	Validation study: receiver(RX) and IPT track(TX_i is set with PSF-6 design	111
7.8	Validation study: receiver(RX) and IPT track(TX_i is set with PFS-1 design	111
7.9	Receiver Power and coupling factor with PSF-6 design	112
7.10	Receiver mutual inductance with PSF-6 design	112
7.11	Receiver Power when IPT track is set with PSF-1	112
7.12	Mutual inductance and coupling factor when IPT track is set with PSF-1 design	113
7.13	CNC design of the experimental setup according to "POS-6" design values	114
7.14	The experimental setup for dynamic IPT system which is built based on "POS-6" design values	115
7.15	FEA study for dynamic wireless power transfer	119
7.16	The depicted 16-discretized reference levels of the primary resonant current for IPT-roadway having three transmitters ($TX_i, i = 1 : 3$)	120
7.17	Proposed control of DWPT for matrix converter for primary current regulation according to pickup side position	121
7.18	ANSYS combined with MATLAB simulation results as RX_1 moves all the way from TX_1 to TX_3	123
8.1	Conceptual Picture: AC-AC Matrix Converter and IPT system	128

8.2	The simulation results for the signals $count2(i)$, $count22$, $count3$ and $count33$	129
8.3	Count4(t) ($\forall t \in [0 \dots 15]$) which contains $t + 1$ pulses in negative half cycles	129
8.4	Count5(k) ($k = 0$ to 15) which contains the ($k+1$) pulses in positive half cycles	130
8.5	Equivalent circuit operations with active and zero states for Grid to Vehicle operational mode	131
8.6	Dynamic IPT setup comprised of 5 bipolar transmitting couplers and a receiver	134
8.7	Resonant high frequency converter with FPGA-based IPT power controller	134
8.8	3-d plot: output power vs energy injection in positive half cycle(L_{pos}) vs energy injection in positive half cycle(L_{neg})	135
8.9	Switching signals when the multi-power level controller is set to operate in total level of 5 ($L_{neg} = 3$ and $L_{pos} = 2$) (a) Dip switches for power level selector for positive are set $P_3P_2P_1P_0 = "0001"$ (b) Dip switches for power level selector for negative are set $N_3N_2N_1N_0 = "0010"$	136
8.10	Power level controller is set to operate in total level of 9 ($L_{neg} = 5$ and $L_{pos} = 4$) (a) Power level selector for positive are set $P_3P_2P_1P_0 = "0101"$ (b) Power level selector for negative are set $N_3N_2N_1N_0 = "0100"$	137
8.11	Power level controller is set to operate in total level of 17 ($L_{neg} = 8$ and $L_{pos} = 9$) (a) Power level selector for positive are set $P_3P_2P_1P_0 = "0111"$ (b) Power level selector for negative are set $N_3N_2N_1N_0 = "1000"$	138
8.12	Power level controller is set at 23 ($L_{neg} = 11$ and $L_{pos} = 12$) (a) Power level selector for positive are set $P_3P_2P_1P_0 = "1010"$ (b) Power level selector for negative are set $N_3N_2N_1N_0 = "1011"$	139
8.13	Power level controller is set at 29 ($L_{neg} = 14$ and $L_{pos} = 15$) (a) Power level selector for positive are set $P_3P_2P_1P_0 = "1101"$ (b) Power level selector for negative are set $N_3N_2N_1N_0 = "1110"$	140
8.14	Power level controller is set 32 ($L_{neg} = 16$ and $L_{pos} = 16$) (a) Power level selector for positive are set $P_3P_2P_1P_0 = "1111"$ (b) Power level selector for negative are set $N_3N_2N_1N_0 = "1111"$	141
8.15	Efficiency plots at different power transfer levels	142

CHAPTER 1

INTRODUCTION

1.1 Motivation

Wireless power transfer by the way of magnetic induction...

1.2 General Statement of Problem Area

General Statement of Problem Area

The global use of electric vehicles (EV) is on the rise[1]. Several technologies for charging the EVs have been developed over the years namely: plug-in electric vehicles, static wireless charging systems, [2]. The problem with stationary wireless charging systems (SWSC) are high battery size, bulky structure, high electromagnetic emission; that all speed up the transition from static to dynamic wireless charging that brings up in-motion charging benefit[3] that can help promote the adoption of EV. Moreover, dynamic wireless EV charging technology can eliminate the need for large size battery which is inevitable in the SWSC. To realize wireless power transfer, there are three major methods: inductive power transfer (IPT) [1], the capacitive power transfer (CPT), and combination of IPT with CPT systems [4]. Generally, there are three major categories for primary coupler configuration, long-track-loop transmitters[5], and short-individual transmitters[6]. A long-track-loop transmitter structure has two problems: first, high self-inductance caused by long-track-loop transmitter can limit the IPT's resonant frequency, second, low coupling coefficient of this coil system decreases the IPT systems' efficiency and makes it impractical for dynamic IPT systems[7]. On the other hand, segmental array of couplers as an alternative configuration was introduced which could be connected in either parallel or series to the same primary converter[8]. This kind of coupler system can solve the high self-inductance problem of the long-

loop coupler, however it causes power pulsation problem as pickup move away transmitter by transmitter[9]. To address this issue, several rectangular transmitter are composed side by side with zero space to form a tracking lane that can realize a continuous dynamic power transfer [8]. However the negative coupling between the active coupler and adjacent inactive couplers can lower the efficiency of the track which is studied as a major concern in this dissertation.

In Fig. 1.1, a typical IPT system with multiple transmitters array connected in parallel is shown . This system is composed of power converters, loosely coupled magnetic structures and compensation components. This dynamic charging system is a dynamic contactless EV charging system while they are moving on the roadway powered tracking lane.

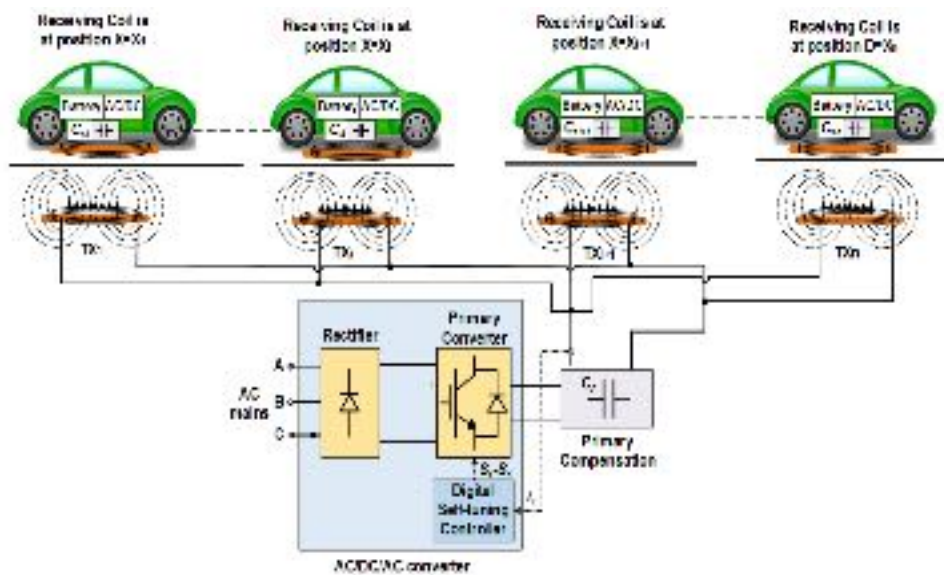


Figure 1.1: The Dynamic wireless power system for EV charging systems.

Research Purpose

Though the concept of DWPT is still an emerging one, a couple of solutions have been proposed to address the challenges faced with DWPT systems. This research is set to increase the efficiency of the dynamic IPT systems to be comparable to the efficiency of stationary IPT systems. Therefore, the aim of this research is to enhance the efficiency, to provide continuous power transfer rate in whole the

track, and to reduce the cost for the development of IPT technology for dynamic EV charging applications.

Research Problem

To increase power transfer and tolerance to lateral offset in track-based systems, optimal design of IPT systems for electric vehicle charging applications is studied. Moreover, the circuit topology, magnetic couplers with wide charging zone, and control methods are considered for design of dynamic IPT systems. Therefore, all the items to be studied in this research are summarized as follows:

1. Design optimization of magnetic structures for IPT based EV charging applications for multiple objectives:
 - Multi-objective design optimization of bipolar power pads topology (DD pads for transmitter pad, and DDQ receiver pad) for dynamic IPT systems; replacing circular pads which has 40% null coupling with the proposed couplers
 - Price along with pads volume, and weight all are together considered as the cost objective function to be minimized.
 - Tolerance to lateral misalignment, coupling factor, loss, power density, and quality factor are considered as a separated objective function in the optimization.
2. New control techniques for the optimized operation of power electronic converters in dynamic IPT systems:
 - New multi-power level power controller to regulate the power transfer rate; enabling highest energy injection level in lowest coupling rate, and vice versa
 - Energy-injection and free-oscillation control methods to control the power injection level; tuning the power transfer rate corresponding to multiple pickups

- Model estimation of whole the IPT-systems: The accurate estimated IPT system model is used for estimating the receiver position which is necessary for position-based multi-power level control of dynamic IPT systems.
3. Addressing some common issues of inductive EV charging systems
- Resonant frequency deviation-based ign object detection control implementation for IPT systems.
 - Virtual inertia-based control multi-power level IPT systems to synchronize the charging level with electric grid dynamic.

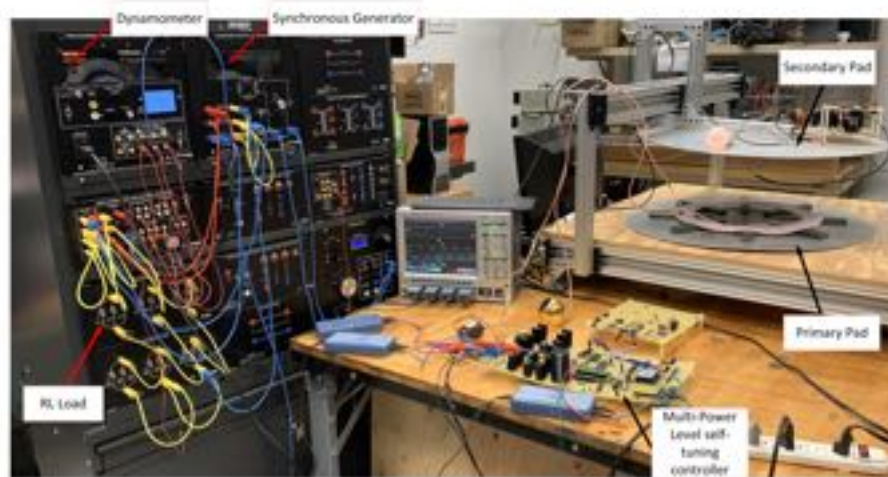


Figure 1.2: Proposed Multi-power level controller for dynamic inductive electric vehicle charging using estimated position

Preliminary Result

Theoretical Perspective

In this research, multi-power level IPT system is studied that can increase the power level under misalignment condition along the track, this can help get rid of both negative coupling between transmitters, and power pulsation. To identify the misalignment case as receiver moves away, an accurate IPT model estimation along the track is developed which can contribute to smart power transfer controller.

A new multi-power level IPT system are developed using free oscillation and energy injection technique. The power injection can happen in both positive and negative half cycles according to the power transfer level value set. Using this technique, the power transfer to secondary side in the injection mode; and zero power transfer happens to the secondary coil in the free oscillation mode. The proposed multi-power level controller was applied on a stationary IPT systems as shown in fig.1.2, and in the future research is applied on dynamic inductive power transfer for vehicle charging application. The power transfer level reference of the proposed controller is online updated via estimating the pickup coil position on the track.

FOREIGN OBJECT DETECTION IN INDUCTIVE CHARGING SYSTEMS BASED ON PRIMARY SIDE MEASUREMENTS

2.1 Introduction

The use of electric vehicles (EVs) has been on the rise in recent years with global stock in excess of 3 million EVs [10]. There are also projections for massive increase in the use of EVs in the future. Presently, most electric vehicles battery charging systems requires a physical connection between the EVs and the charging station. This obviously comes with some challenges which include the lack of flexibility of the charging system, less convenience, safety concerns with the use of charging cables amongst others. Contact-less forms of charging tends to address these issues with the contact-based charging systems. The use of IPT systems for wireless power transfer is one of the most promising methods of contact-less power transfer[11–15]. There are many advantages for the necessity of wireless power transfer technology; first, to ease electric vehicle charging second, to control microgrid system frequency [16–20] using G2V/V2G modes. The transmitter pad is used to create a high frequency magnetic field which causes an emf to be induced in the secondary receiver pad. The secondary induced emf can then be used for charging the battery after rectification. For loosely coupled (usually with large air gap between the transmitter and the receiver pads) IPT systems, resonant inductive coupling can be employed. This allows for a highly efficient IPT system by generating high amount of resonant currents that enable bulk power to be easily transferred from the primary pad to the secondary[21, 22].

For IPT systems with wide air-gap, there is an increased possibility of foreign object intrusion in to the system air-gap. Several methods have been proposed to detect this intrusion of foreign objects in IPT systems, This include the measuring some parameters of the IPT systems such as its capacitance [23] , inductance [21]

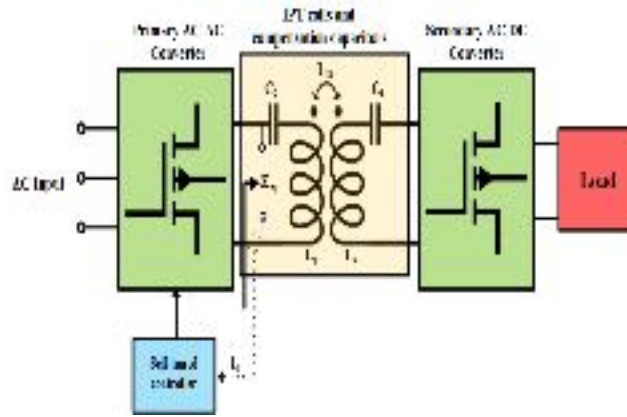


Figure 2.1: Schematic diagram of the simulated IPT system

(and consequently resonant frequency), induced emf [24], loss in power transfer [25, 26], and the time for the energy in the circuit to decay [27]. Other methods of foreign object detection (FOD) which uses some sensors include taking measurements of the light intensity [14], the use of thermal sensors [28] to monitor the heat generated as result of the foreign object, the use of magnetic field sensors to monitor and measures changes in the IPT's magnetic field as a result of the foreign object.

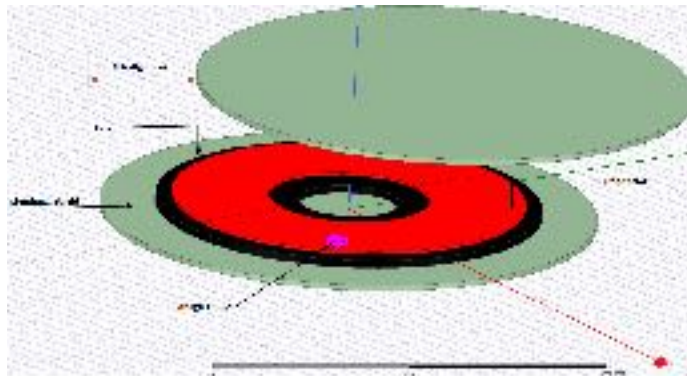
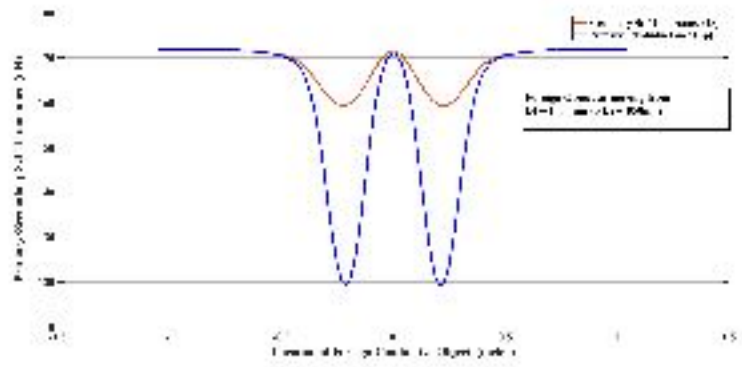


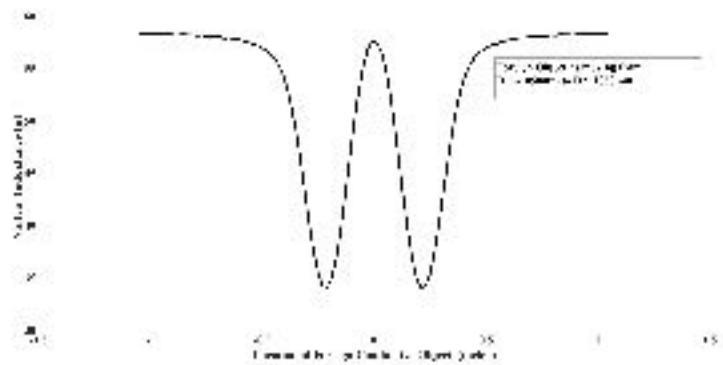
Figure 2.2: 3D Model of the studies IPT system for Misalignment and FOI

2.2 Theoretical Formulation of Proposed Methodology

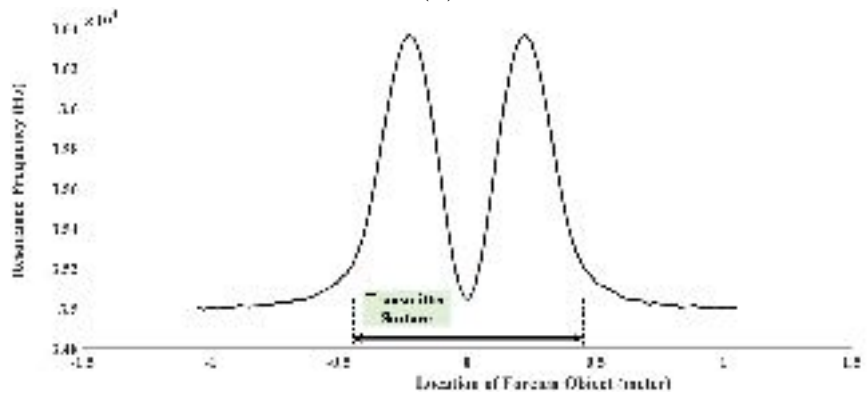
The presence of foreign object within air gap and misalignment of an IPT can be captured by measuring the primary, secondary and the mutual inductance values



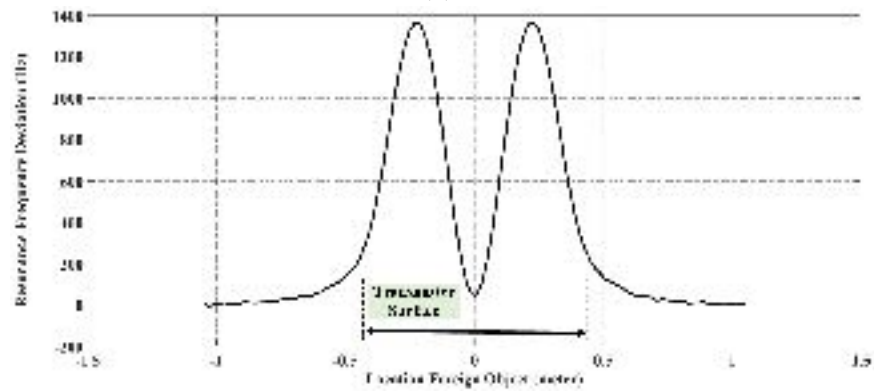
(a)



(b)



(c)



(d)

Figure 2.3: FOI and Detection (a) Primary/Secondary Self Inductance (b) Mutual Inductance (c) resonance frequency (d) Frequency Deviation

(L_p , L_s and L_m), (Fig. 2.1) [15, 29, 30]. These change in inductance values consequently affects the resonant frequency of the IPT systems. According to [21, 23], the Z_{eq} (impedance of IPT system from the primary side) of a resonant IPT system with series-series compensation, and transfer function of IPT system accordingly can be expressed as:

The transfer function of the system can be expressed as:

$$H(s) = \frac{sC_p(1 + s^2C_sL_s + sC_sR_s)}{\left[C_pC_s(L_pL_s - M^2)s^4 + C_pC_s(L_sR_p + L_pR_s)s^3 + (C_pL_p + C_sL_s + C_pC_sR_pR_s)s^2 + (C_pR_p + C_sR_s)s + 1 \right]} \quad (2.1)$$

where L_p , L_s , L_m , are primary, secondary and the mutual inductance, C_p , C_s , R_p , R_s , are primary and secondary compensation capacitance and resistances respectively. The imaginary part of the dominant poles of (2.1) (zeroes of Z_{eq}) which represents the IPT system's resonant frequency is used in this chapter to calculate new resonant frequencies of IPT system with new values of L_p , L_s , L_m . However, in some frequencies which are the same between applied scenarios (FOI and misalignment), the impedance's changes tends to be quite small which makes it inappropriate variable for discrimination. However, the RMS value of their resonant currents shows more significant changes due to high amplitude of the converter voltage even with minute changes in Z_{eq} . Furthermore, FOI significantly change the self-inductances which directly affect the resonance frequency, however, misalignment affects more coupling rate than self-inductance

2.3 Simulation Results and Analysis

A 3D FEA model of the IPT system is simulated to obtain the values of L_p , L_s , L_m , while the values of C_p and C_s are selected in such a way to achieve the desired resonant frequency of 35kHz under normal operating condition. For other cases other than normal condition, resonant frequencies are calculated with respect to

normal one. In the misalignment case, the secondary pad was moved from outside the length of the transmitter pad on the left, towards the center and completely all the way outside of the transmitter pad on the right hand side.

For the case of FOI, with the proper alignment of the pads, the foreign object is moved from outside the length of the pads on the left towards the centre and completely all the way outside the two pads towards the right (as represented in Fig. 2.2). The various values of L_p , L_s , L_m is used to obtain the RMS value of the resonant currents using MATLAB/Simulink.

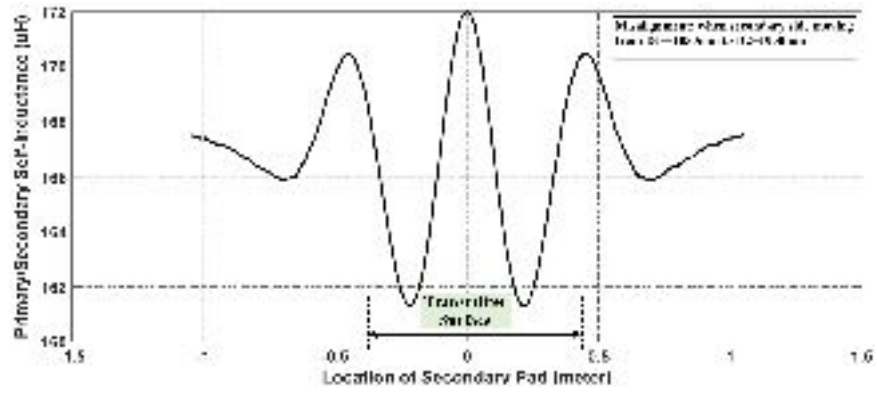
2.3.1 Foreign Object Intrusion and Detection

Fig. 2.9 shows the variation of L_p , L_s , L_m with the corresponding change in resonant frequency as the object moves from outside the region between the two pads on the left hand side to the right hand side of the two pads. It can easily be inferred from Fig. 2.9 that, while the foreign object is completely outside the two pads, the values of L_p , L_s , and L_m as shown in figures . 2.9a and 2.9b are not impacted as a result we have no frequency deviation Fig. 2.9d.

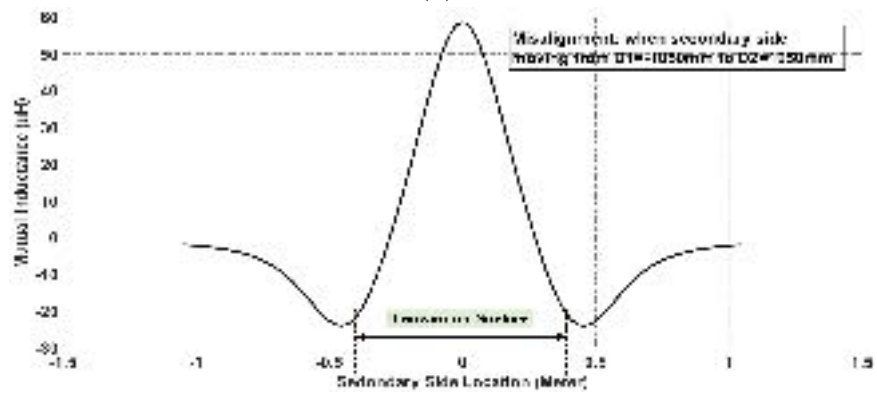
Table 2.1: Specifications of IPT System and inductances of FOI and Misalignment

Parameter	Value	Frequency Deviation	Inductance (μH)	Normal	FOI	Misalignment
Grid voltage (V_{LL})	120V	74Hz	Primary (L_p)	172	161.32	170.2
Grid frequency (f_{ac})	60 Hz		Secondary (L_s)	172	161.29	170.45
(P_{max})	8 kW		Mutual (L_M)	57.78	12.88	55.75
Coupling Factor (k)	0.2	8Hz	Primary (L_p)	172	168.48	170.89
Compensation capacitors (C_p, C_s)	1.3352 μF		Secondary (L_s)	172	171.46	170.88
Battery voltage (V_b)	100 V		Mutual (L_M)	57.78	49.28	57.62

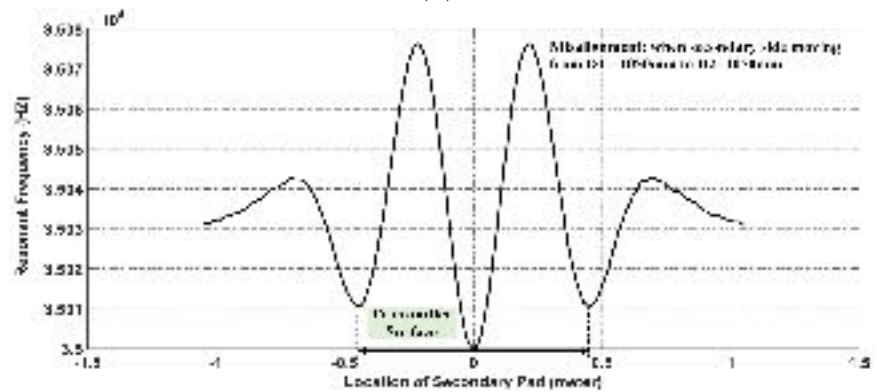
However, as the object moves towards the pad, the values of L_p/L_s , L_m (as seen in figs. 2.3a, 2.3b) reduces and gets to its minimum exactly where the object is located in between the surface of the IPT coils consequently, the frequency deviation reaches to its maximum value Figs. 2.3c and 2.3d. As it moves away from the IPT coil surface toward the center of coil (origin), the inductance values increase and gets back to its value prior to entering the pads, meaning no impact



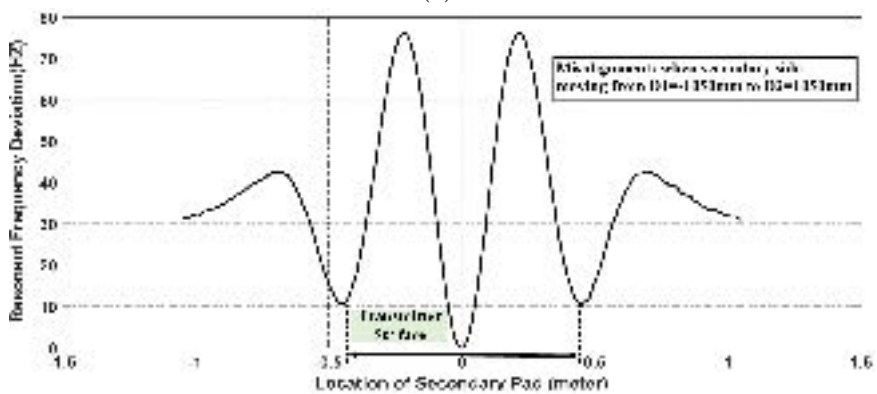
(a)



(b)



(c)



(d)

Figure 2.4: Misalignment between transmitter and receiver pads (a) Primary/Secondary Self Inductance (b) Mutual Inductance (c) resonance frequency (d) Frequency Deviation

on inductance exactly in the center. The inductance values and the frequency deviation follow the same trend as the foreign object moves out from the centre of the pads to the edge.

2.3.2 Misalignment of Transmitter and Receiver Pads

in this case, the receiver pad is moved from the extreme left of the transmitter pad to its extreme right. The impact on the values of L_p/L_s , and L_m and are as shown in figures 2.4a and 2.4b and the corresponding resonance frequency (f_r) and deviation in frequency are shown in figs. 2.4c and 2.4d. The frequency deviation is zero when the receiver pad has zero misalignment, however, it increases when there is a misalignment between the pads as shown in figs. 2.17c and 2.17d.

2.4 discrimination of FOD and misalignment

Resonance frequency-based FOD method is effective for objects that significantly affect resonance frequency. On the other hand, smaller size conductive objects have no remarkable effect on frequency deviation and overlap with frequency deviation range caused by vehicle variation (8Hz to 74Hz). Therefore, discrimination technique needed to distinguish between these two cases. It is desirable to allow the IPT system to self tune itself and continue supplying power to the secondary pad in the case of a misalignment and possibly disconnect the IPT system in-case of FOD which could lead to fire due as a result of the generated heat due to the induced eddy currents. In the overlapping range of the resonant frequency deviation for FOI and misalignment scenarios, the impedance's changes tends to be quite small. However, the RMS value of primary resonant current is more appropriate as a discrimination signal. The reason lies in the fact that the coupling factor is considerably impacted by misalignment, as a result, the power transfer will be decreased which means greater primary resonant current is needed to com-

compensate the lowered efficiency, however, in FOD case, only self-inductances are significantly affected than coupling rate.

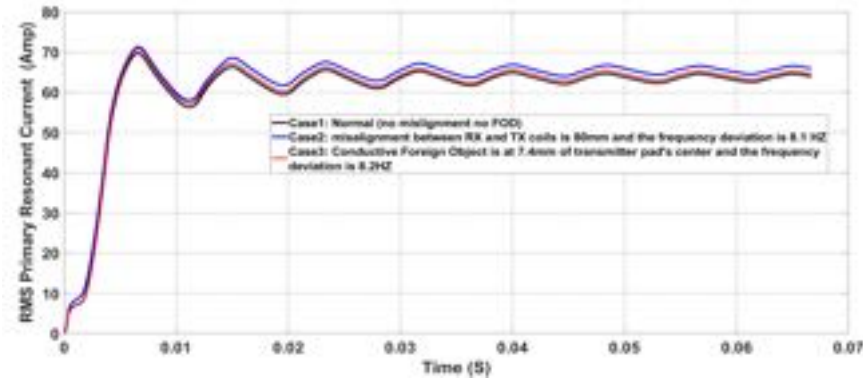


Figure 2.5: Resonant RMS current during normal conditions, misalignment and FOD maximum frequency deviation of 8Hz

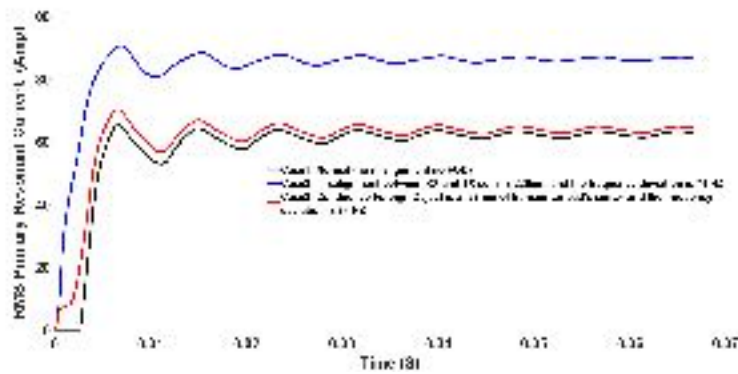


Figure 2.6: Resonant RMS current during normal conditions, misalignment and FOD maximum frequency deviation of 74Hz

Simulation for discrimination of two cases is carried out in MATLAB with magnetic specifications given in table 2.1. Figures 2.5 and 2.6 show the RMS value of the resonant current for three cases including: normal operation of the IPT system, foreign object intrusion and vehicle variations. The simulation is done for the studied IPT system as IPT system is regulated to deliver $P_{out} = 8KW$ to the secondary side. Repetitive simulations have shown that in all overlapping range of frequency deviation, the RMS value of primary resonance current for the misalignment case increases more than the corresponding current for FOI case. As examples, simulation results for the two extreme values of overlapping range of

frequency deviation ($8Hz$ and $74Hz$) are given in figures (2.5 and 2.6). As it can be seen, the RMS value of primary resonant currents for the misalignment case are greater than the corresponding plot for FOI case for both frequency deviation of either $8Hz$ or $74Hz$. Therefore, it can be concluded that when the frequency deviation is in the range of $[8Hz-74Hz]$, the recorded primary resonance current change should be checked, if the primary resonant current significantly changes, the cause of frequency deviation would be the misalignment not FOI.

2.5 Conclusion

A novel technique using resonant current to discriminate foreign object from misalignment is presented. A FEA of an IPT system is used to compute the various changes in L_p , L_s and L_m values for both FOI and misalignment. The results showed that both cases cause a deviation in resonant frequency with the foreign object intrusion and misalignment causing a maximum frequency deviation of $660Hz$ and $74Hz$ respectively with an frequency deviation overlap between $8Hz$ to $74Hz$. To discriminate between these two cases during the frequency overlap, a measurement of the RMS value of the resonant current for FOI and misalignment have shown that the greater amount of resonance current is needed in primary converter to compensate power reduction in case of misalignment occurrence than FOI due to relatively high reduction of coupling rate in misalignment case.

2.6 Introduction

Nowadays, energy delivery to the load without any electrical contact is becoming more popular by using inductive power transfer (IPT) technology. IPT systems are divided in two major categories, this includes loosely-coupled and closely-coupled systems. The former systems have larger gap between receiver and transmitter sides, however the later systems have smaller gap and higher coupling rate. Due

to its flexibility and larger gaps, loosely-coupled IPT are well fit for electric vehicle applications [11, 31–36]. Relatively lower coupling rates of loosely-coupled IPT systems can be compensated by a capacitor tank because they can resonate with the self-inductance of a primary side which can lead to larger primary resonant current and higher power transfer. High resonant frequency IPT systems up to 90kHz, can be designed by selecting the appropriate compensation capacitors that can help reduce the size of coils in both the primary and secondary sides[37]. Hence, high resonant frequency combined with a high-magnitude magnetic field in the gap between primary and secondary coils can keep wireless power transfer rates high. However, this high magnitude magnetic fields can induce intense eddy-current on a conductive foreign object intruded to the power transfer area, which can lead to heat rise and to fire in a worst case [38]. Therefore, it is essential to quickly detect the intrusion of a conductive object to avoid efficiency reduction, and more importantly, to eliminate the risk of a fire in the charging area [39, 40]. Another important control action needed to be done is to differentiate a foreign object intrusion (FOI) case which requires shutting the IPT system down from the misalignment case which is not dangerous but lowers the power transfer rate. The discrimination process is explained with detail in Section IV.

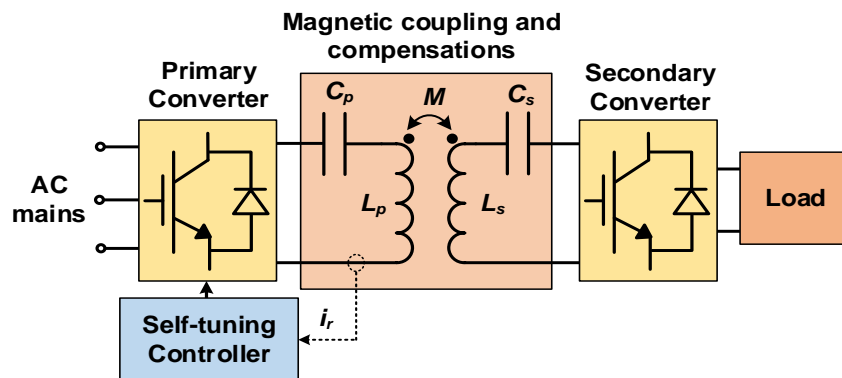


Figure 2.7: Schematic diagram of the IPT system.

In literature, FOD strategies are classified into two: sensor-based and sensor-less detection. Prime examples of sensor-based methods include the use of image processing [41], thermal sensors [42, 43], distance detection [44], magnetic field sen-

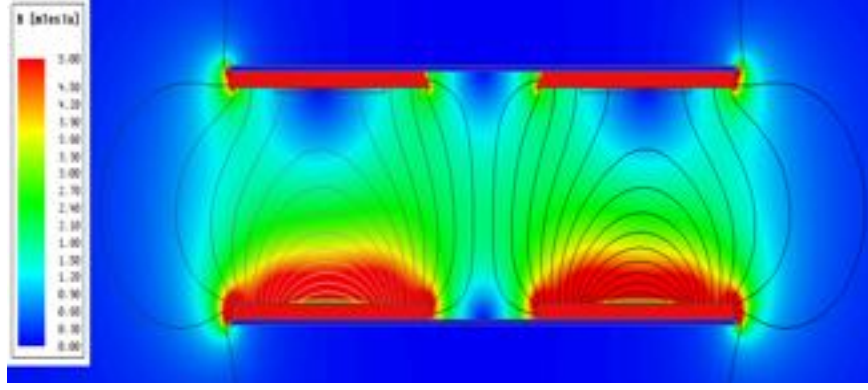
sors [45], and light intensity monitoring [14]. However, sensorless FOD methods utilize real-time monitoring, measurement and estimation of highly affected parameters in IPT systems namely capacitance [46], energy decay time [47], induced voltage [48] and power loss [49, 50] to identify the foreign objects.

Fixed switching PWM converters are controlled by regulating the phase shift of the converter output and duty cycle in IPT system. The major drawback of these converters is the variation in resonant frequency which is typical of IPT systems. This variation affects the IPT's efficiency, whenever the operating switching frequency is different from the resonant frequency [51]. This has led to use self-tuning controllers which synchronizes the converter switching to the circuit resonant frequency [51–55]. These self-tuning controllers has one major benefit; the IPT systems' performance will not be influenced by natural resonance frequency oscillations. Furthermore, FOD implementation on the existing self-controller is easier by using online measurements of resonance frequency deviation. In this chapter, the same self-tuning controller employed for switching generations is also used for FOD implementation. The proposed FOD method based on frequency deviation is very fast because the foreign object intrusion to the power transfer area can markedly impact the electromagnetic characteristic of IPT (self and mutual inductance) which can be detected as the resonance frequency deviation in self-tuning controllers. In this chapter, FEA results show that the cause of the resonance frequency deviation could be either FOI or vehicle positional variations (so called misalignment), therefore, the proposed FOD method uses two major steps to differentiate them from each other. Firstly, detection of the resonant frequency deviation([31]) as a warning of disturbance in IPT system, secondly, the use of primary resonance current to discriminate FOD from misalignment. In the proposed approach, the resonant frequency is constantly monitored and compared to nominal value to detect the intrusion of any foreign object. In this study, the resonance frequency of IPT system is measured using primary resonant current

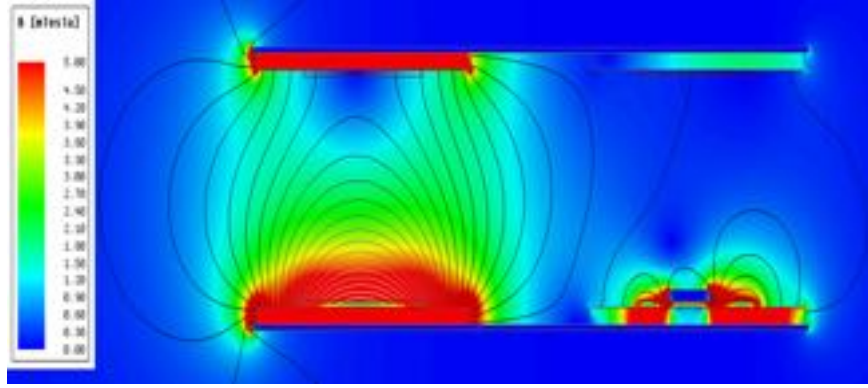
feedback. The measured current is used as a clock to measure resonance frequency which is used in self-tuning converters as a switching frequency. Therefore, for implementation of the FOD method, which is based on frequency deviation, using existing self-tuning converters eliminates any need for additional structures and sensors to be installed on IPT systems. Two detection modes are defined in this study; the online and the standby mode. During the online mode, the FOD is done when the IPT system is running; however, in standby mode, the IPT system is not active and the vehicle is absent. A 2D and 3D finite element analysis (FEA) for FOI is presented as theoretical analysis. Simulation results of the proposed FOD and misalignment discrimination are presented. The experimental results to verify the effectiveness of the proposed FOD method for conductive foreign objects of different sizes and shapes in either of IPT's operating modes are presented. Moreover, the discrimination method is experimentally verified for wide range of resonant frequencies. The test results show that the proposed methods are effective in detection of very small objects such as a small coin within few millisecond, and useful in discrimination of foreign object intrusion from misalignment which is common in both dynamic and static charging systems.

2.7 FEA analysis of conductive foreign Object intrusion in IPT Systems

Foreign objects within charging areas area acts like an electromagnetic shield against high frequency magnetic fields, and this results in electromagnetic disruption of the area where foreign objects are placed. Foreign objects causes a significant change in magnetic coupling, primary and secondary self-inductances (L_p and L_s), and mutual inductance(M). Other than foreign object locations inside the power transfer area, there are other factors which determine the level amount of frequency deviation, including the object dimension, the structure, and



(a)



(b)

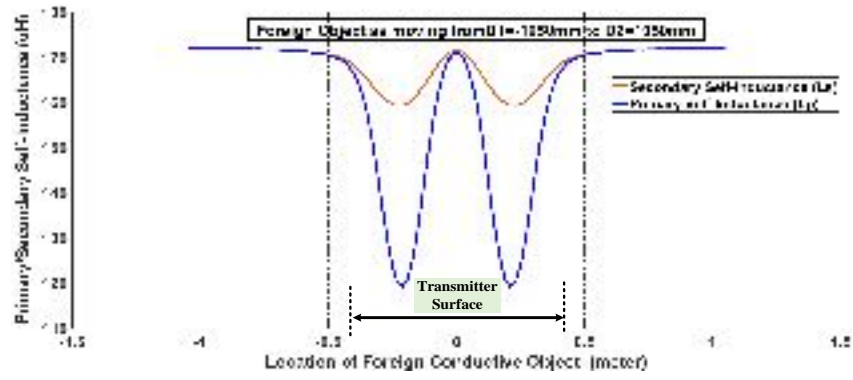
Figure 2.8: 2D FEA analysis: (a) magnetic flux density without object presence, (b) magnetic flux density with the presence of conductive object.

object type. Magnetic flux lines of circular primary/secondary pads with/without the presence of foreign object are shown in Fig. 2.8. Distorted magnetic flux lines with foreign object intrusion into power transfer area is shown in Fig. 2.8(b).

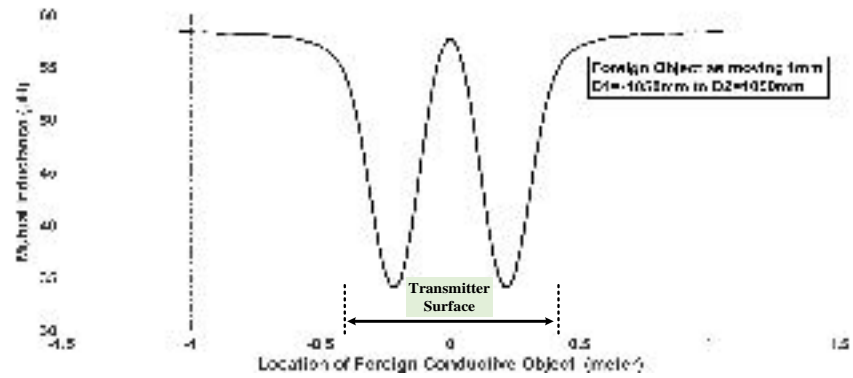
2.8 theoretical analysis for the proposed FOD Method

To clearly show the effects of foreign objects on primary/secondary self-inductances and mutual inductances (L_p , L_s and M), formulation analysis is needed. According to Fig. 2.7, the equivalent total impedance from the primary side can be formed as below:

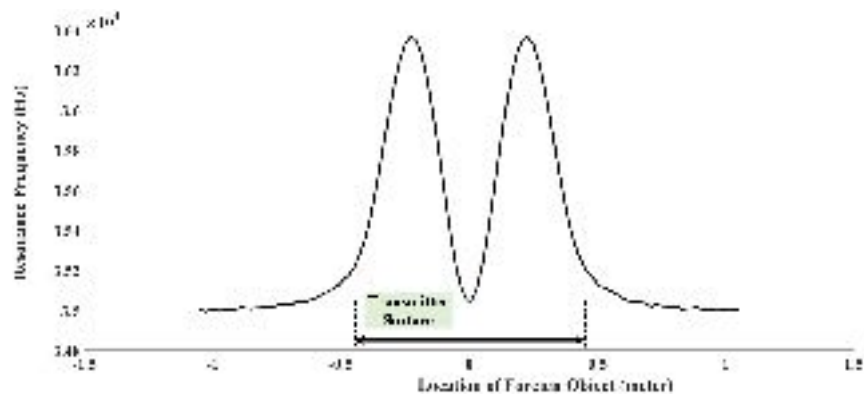
$$Z = R_p + \frac{1}{sC_p} + sL_p + Z_r \quad (2.2)$$



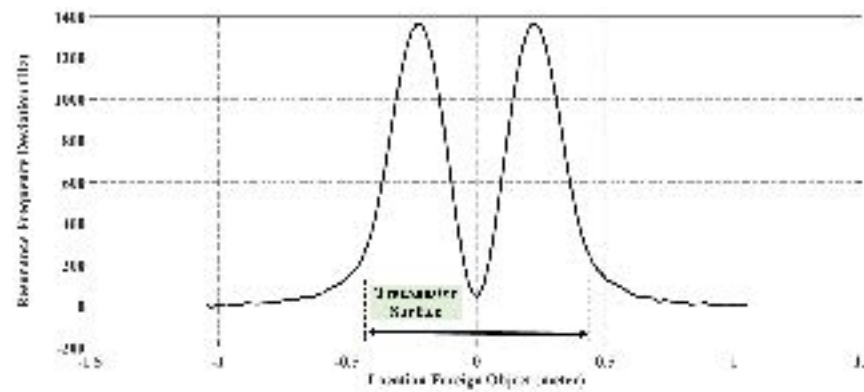
(a)



(b)



(c)



(d)

Figure 2.9: FOD and Detection (a) Mutual Inductance (b) Primary Self Inductance (c) Secondary Self Inductance (d) Frequency Deviation.

where, C_p is the primary compensation capacitor, and R_p is the primary resistance. Z_r is the impedance of a secondary coil seen from the primary side which can be written as:

$$Z_r = -\frac{s^2 M^2}{\frac{1}{sC_s} + sL_s + R_s} \quad (2.3)$$

where, C_s is the secondary compensation capacitor, R_s is the secondary equivalent resistance which includes the load resistance and secondary coil resistance. The transfer function of the IPT system with the primary resonant current as the output, and the primary converter voltage as the input can be calculated as:

$$H(s) = \frac{I_p}{V_p} = \frac{1}{Z} \quad (2.4)$$

the transfer function of the IPT system can be as shown in (2.5), by replacing equations (2.2) and (2.3) in (2.4).

$$H(s) = \frac{sC_p(1 + s^2C_sL_s + sC_sR_s)}{\left[C_pC_s(L_pL_s - M^2)s^4 + C_pC_s(L_sR_p + L_pR_s)s^3 + (C_pL_p + C_sL_s + C_pC_sR_pR_s)s^2 + (C_pR_p + C_sR_s)s + 1 \right]} \quad (2.5)$$

The imaginary part of the dominant poles of the derived transfer function (Eq. (2.4)) is used in this chapter to calculate new resonant frequencies of IPT systems. Equation (2.4) indicates that the variation of L_p , L_s , L_m due to presence of a conductive foreign object in power transfer areas changes the dominant poles of equation (2.5) which are resonant frequencies. Therefore, foreign object existence can be identified by the real-time measurement of resonance frequency. Finite element analysis (2D/3D) is done to analyze the magnetic effect of the foreign object on the IPT system. 2D FEA results are presented in Fig. 2.9 to illustrate the magnetic change on IPT system sides due to FOI. The results show the variation of L_p , L_s , L_m , resonance frequency (f_r), and resonant frequency deviation (df_r) which are represented in Figs. (2.9a, 2.9b, 2.9c and 2.9d), as the foreign object moves from the outside region between the two pads on the left hand side to the right hand side of the two pads. 3D FEA model of the studied IPT system is

also presented in Fig. 2.10, and the electromagnetic analysis is done for foreign object placement all across the charging area. Flux density loss on the ferrites installed in the circular pads, and on the foreign object caused by high frequency electromagnetic field are shown in Figs. 2.11 and 2.12 respectively.

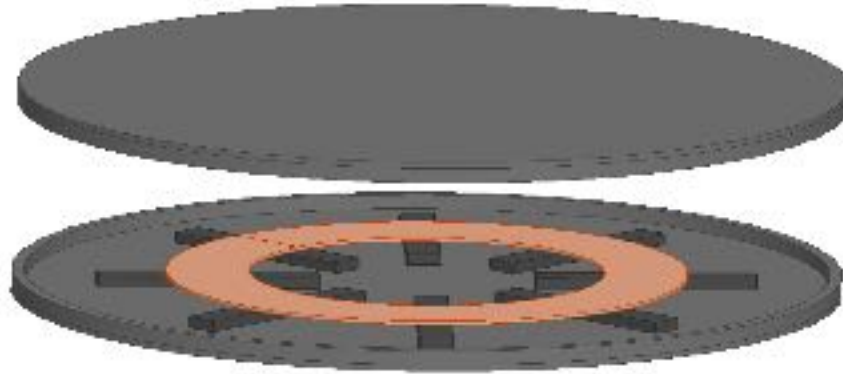


Figure 2.10: 3D electromagnetic model of IPT system.

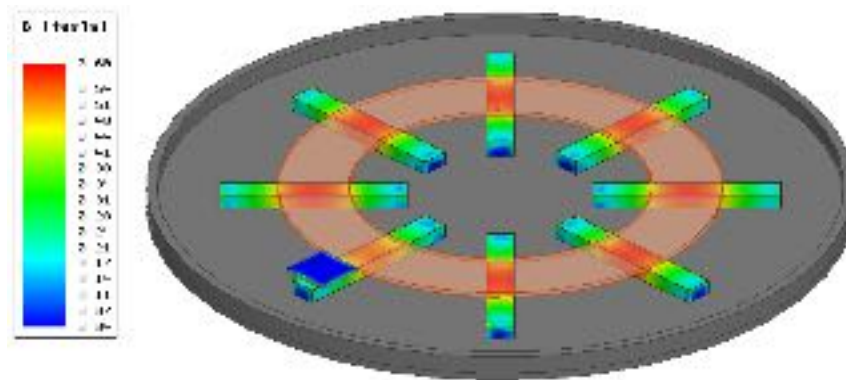


Figure 2.11: distribution of flux density on the primary pad.

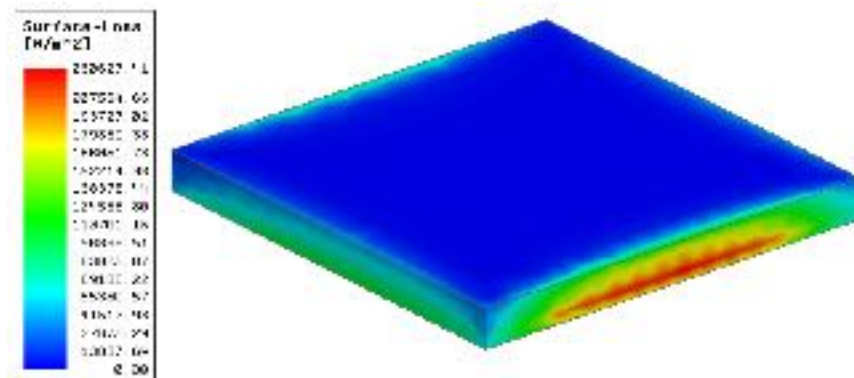


Figure 2.12: loss effect of high frequency electromagnetic field on ferrit bars .

Self-inductances for primary/secondary sides and mutual inductance are all shown in the 3D-plot (Fig. 2.13) for different positions of foreign objects with

respect to the center of the primary pad, which conforms with 2D FEA results presented in Fig. 2.9. The values of L_p , L_s , and L_m represented in Fig. 2.13 are used to calculate the corresponding resonance frequency by finding the poles of the transfer function in (2.5). The resonance frequency as a function of IPT-system's inductances obtained for different positions of foreign objects are represented in Fig. 2.14 which is again in a good agreement with 2D plot shown in the Figs. (2.9c and 2.9d).

According to both 2D FEA and 3D FEA analysis (Figs. 2.9c and 2.14), it can be seen that the resonance frequency reaches its maximum value when the conductive object is located between the surface of the IPT coils, however, it has no impact on inductances and resonance frequency, when the conductive object is located in the area surrounding the center of primary pad. The justification for no impact on inductances and resonance frequency around the center is due to symmetric structures of circular power pads which cancel out all the flux density around the center. Moreover, as it can be seen from Figs. (2.9c and 2.14), the resonance frequency increases for FOI disturbances, however it relatively decreases when a vehicle (receiver pad) enters into the primary pad surface. Also, the resonance frequency drops even further when the wireless charging system operates. According to different causes of frequency deviation mentioned, the formulation for the resonance frequency can be expressed as follows:

$$f_{ref} = f_{r0} - \Delta f_V - \Delta f_L \quad (2.6)$$

$$\Delta f_O = f_r - f_{ref} \quad (2.7)$$

where f_{ref} is the reference frequency, f_{r0} normal resonance frequency when both pads are in a complete alignment, Δf_V is the resonance frequency deviation caused by vehicle misalignment, charging impact on frequency is symbolized as Δf_L , and resonance frequency deviation caused by a foreign object is represented as Δf_O .

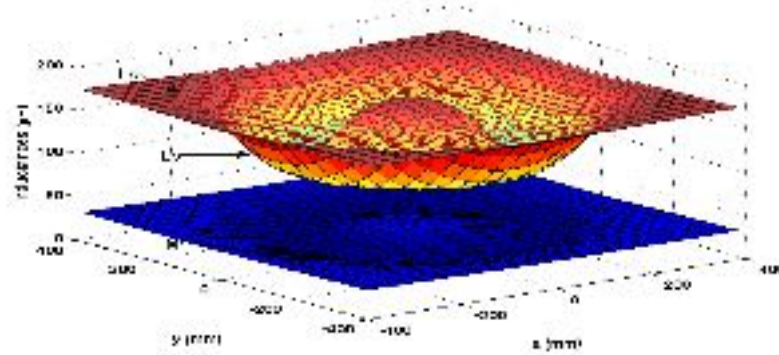


Figure 2.13: Primary/secondary self-inductances (L_p)/ (L_s), mutual-inductance (M) as a function of foreign object location with respect to primary pad center.

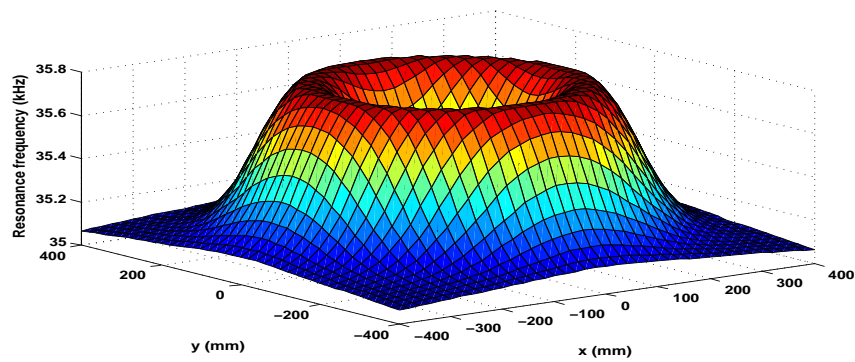


Figure 2.14: 3D plot of resonance frequency as function of foreign object location respect to primary pad center.

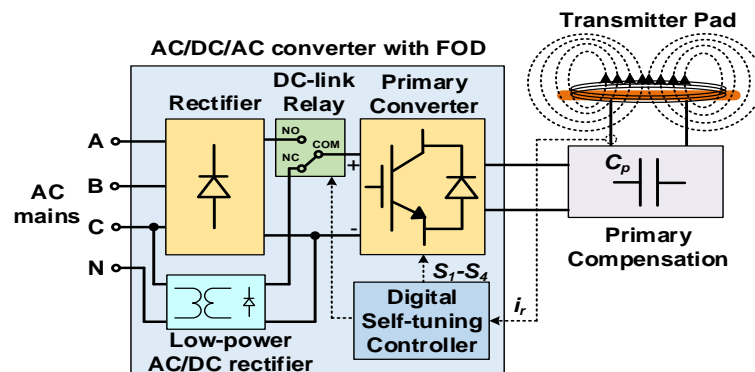
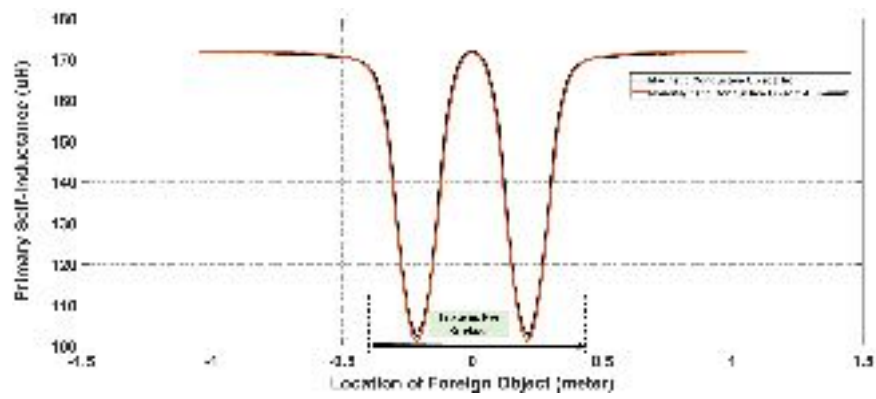
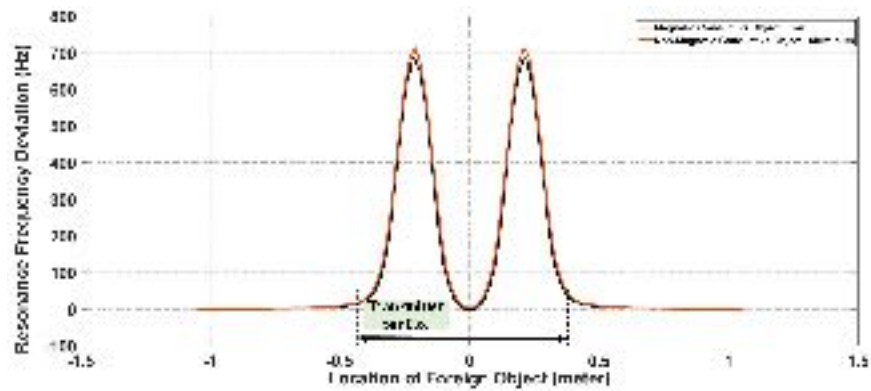


Figure 2.15: Proposed IPT system with consideration of low lower AC/DC rectifier to provide DC link for FOD purpose in the standby mode.

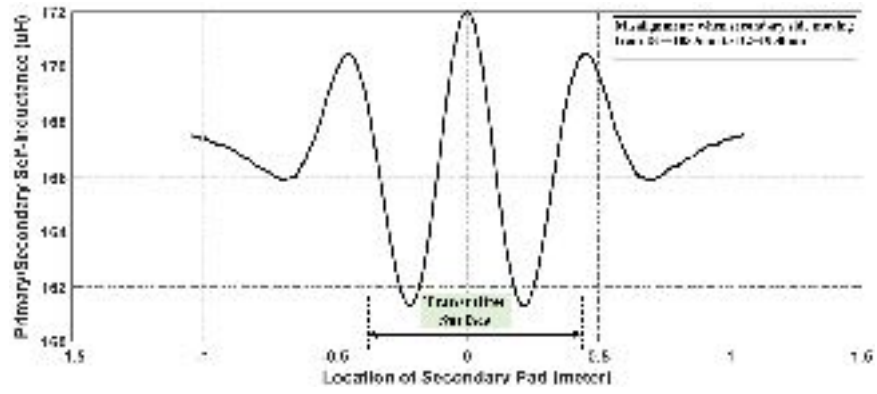


(a)

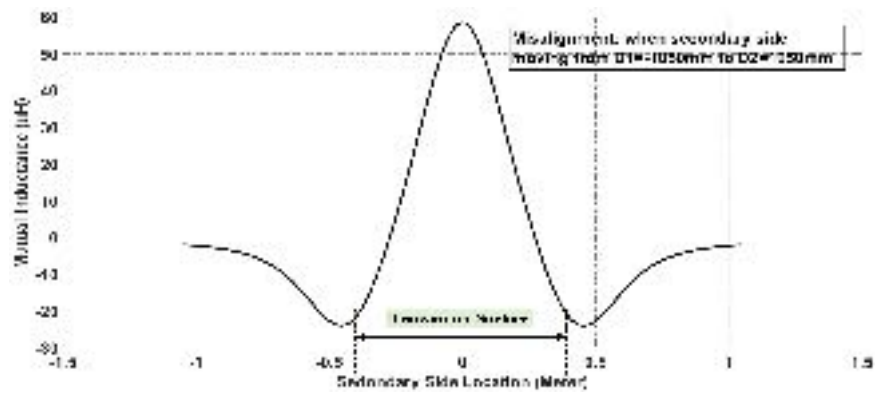


(b)

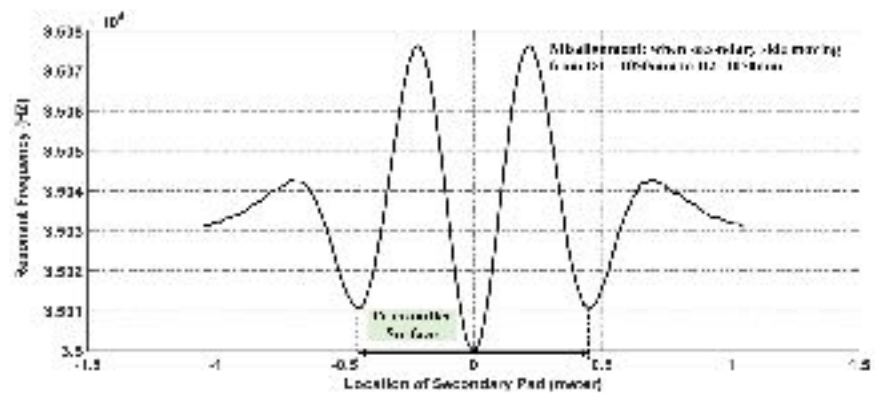
Figure 2.16: FEA analysis for aluminum and iron foreign objects (a) Primary self-inductance (L_P) distortion for two different material of FOI (b) Resonance frequency deviation for two different material of FOI.



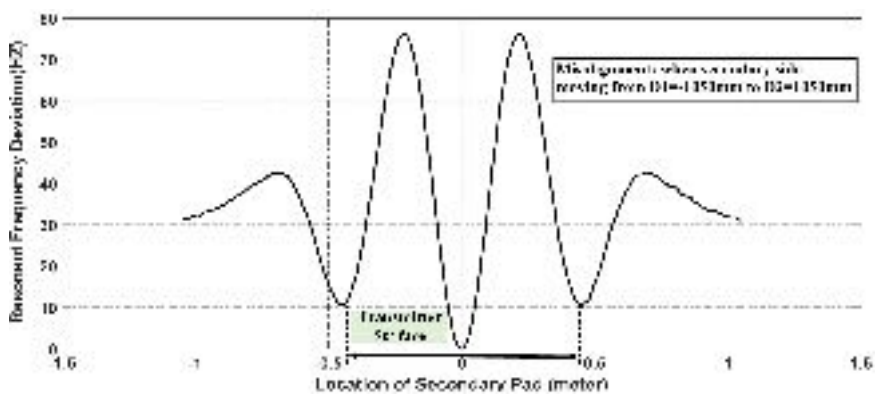
(a)



(b)



(c)



(d)

Figure 2.17: Misalignment between transmitter and receiver pads (a) Mutual Inductance (b) Primary Self Inductance (c) Secondary Self Inductance (d) Frequency Deviation.

2.8.1 FEA Analysis for Magnetic/Non-magnetic Conductive Object

In general, metal can be categorized in two major parts from the field perspective: magnetic conductive metals (with non-trivial permeability), non-magnetic conductive metals (with trivial permeability). Both types of conductive objects impact the electromagnetic characteristics in a similar way when placed in the charging area of IPT systems, because the operating frequency of IPT system is fairly high (35kHz-85kHz). Due to high-frequency magnetic field, the skin depth in both type of conductive objects is very small and therefore, the magnetic field is perpendicular to the surface of the metal objects. In other words, in the electromagnetic model, the conductive object with both material properties can be modeled with Neuman boundary conditions without modelling the inner volume/surface of the it. In order to demonstrate this, two FEA simulations are carried out for the foreign conductive objects with two different permeability (aluminum and iron). Object's size placed in the charging area for the studied analysis is considered ($50mm \times 10mm$). As expected and Fig. 2.16 confirms that aluminum (with relative permeability=1.000021) and iron (with relative permeability=4000) objects have the same effect on the magnetic field, as a result the same resonance frequency deviation is caused by the studied metal foreign objects. Hence, it can be safely concluded that the proposed FOD method can be applicable to all types of metals with different permeability.

2.8.2 Foreign Object Detection At Standby Mode

IPT-systems are exposed to foreign object intrusion in every possible condition, either in high-power conditions (operational mode) when wireless charging system operates, or in very low-power conditions (standby mode) when the IPT-system is off and $\Delta f_V = \Delta f_L = 0$; therefore, the FOD scheme should be enabled in

both modes. In a very-low power condition, DC link should still be provided for a control circuit of a self-tuning controller so that foreign object detection will be guaranteed in the standby mode (Fig. 2.15). Therefore, the DC link in the proposed primary converter switches between low-power mode (single-phase rectifier) when the charging system is off and full-power mode (main three-phase rectifier) when the charging system is on. This mechanism illustrated in (Fig. 2.15) will guarantee a continuous monitoring of power transfer area for FOI irrespective of IPT's operating modes.

2.8.3 IPT-System Losses In Standby Mode

The losses of IPT-systems in standby mode can be expressed as [55]:

$$P = \frac{2\omega V_{dc}^2 \tau^2 (1 + e^{-\pi/\tau\omega})}{\pi L_p (1 + \tau^2 \omega^2) (1 - e^{-\pi/\tau\omega})} \quad (2.8)$$

where r_c is the primary coil resistance, V_{dc} is the DC-link voltage. The damped factor of resonant frequency is $\omega = \sqrt{\omega_0^2 - 1/\tau^2}$, $\tau = 2L_p/r_c$ is the oscillation damping factor, C_p is the primary compensation capacitor, and L_p is the primary self-inductance.

2.8.4 Online Foreign Object Detection In IPT Operational Mode

The FOD method can be used when IPT charging system is enabled, however, vehicle positional variation, which is common in both static or dynamic wireless power charging systems, can impact magnetic characteristics (L_p , L_s , L_m) as shown in Figs. 2.17a, and 2.17b. The corresponding resonance frequency (f_r), and resonant frequency deviation (df_r) are shown in Figs. 2.17c and 2.17d. The frequency deviation at the center of the primary pad (complete alignment) is almost zero because of symmetric pads' shape. As mentioned before, resonance frequency

of IPT system in zero coupling (extreme sides of misalignment) is considered as a reference point, and frequency deviation of other positions are calculated with respect to it. As it can be seen from Fig.2.17d, the maximum resonance frequency deviation caused by vehicle positional variation is 672Hz. In other words, the region of overlap for the resonance frequency deviation caused by FOI and the vehicle positional variation is 8Hz to 672Hz. Though, larger conductive objects can be detected via the proposed FOD method due to large frequency deviation they create, the FOD method cannot be effective in very smaller foreign objects (such as 10d nail and 5-cent coin) that overlap with vehicle variations. Hence, there is a need to distinguish smaller conductive objects effect from vehicle positional variation which is explained in Section IV.

2.9 Discrimination Of FOI From Misalignment

As illustrated in section III, the resonance frequency-based FOD method is effective for objects that significantly affect the resonance frequency. On the other hand, smaller conductive objects have no significant effect on frequency deviation, and it overlaps with frequency deviation range caused by vehicle positional variation. Therefore, discrimination techniques are needed to distinguish between these two cases. It is desirable to allow the IPT system to tune itself and continue supplying power to the secondary in the case of a misalignment. However, in the case of FOI, the IPT system needs to be shut down since FOI could lead to a fire due to the generated heat as a result of the induced eddy currents. In the overlapping range of the resonant frequency deviation for FOI and misalignment scenarios, the primary resonant current is more appropriate as a discrimination signal. The reason lies in the fact that the coupling factor is considerably impacted by misalignment and as a result, the power transfer will be decreased. This means that higher primary resonant current is needed to compensate for the lowered efficiency. However, in case of an FOI, self-inductances are more affected compared

to coupling coefficient. Therefore, it can be concluded that when the frequency deviation is in the range of $[8Hz-672Hz]$, the recorded primary resonance current change should be checked using (2.9). If the primary resonant current significantly changes, the cause of frequency deviation is detected as a misalignment and not an FOI. In Fig. 2.18, a flowchart is presented to show the discrimination method implemented in the setup.

$$\Delta I_{res}^{prim} = I_{res}^{prim}(k+1) - I_{res}^{prim}(k) \quad (2.9)$$

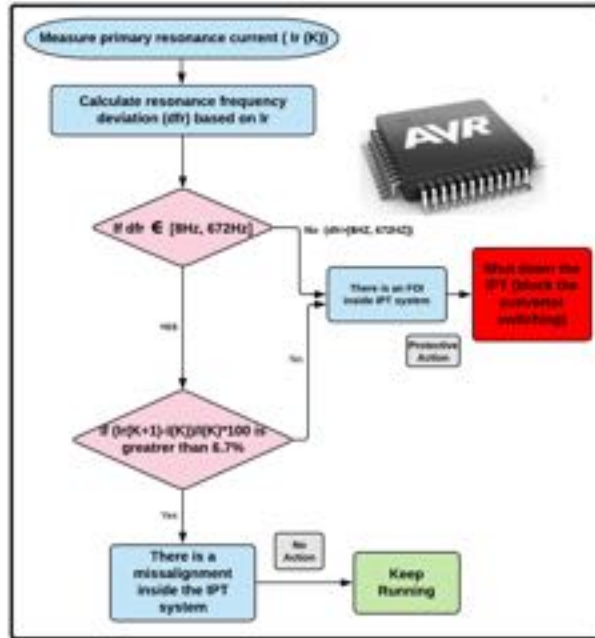


Figure 2.18: Flowchart for FOI and misalignment identification.

The simulation for discrimination of two cases is carried out in MATLAB with the magnetic specifications given in table 2.2. Figures 2.19 and 2.20 show the RMS value of the resonant current for three cases including: normal operation of the IPT system, foreign object intrusion and vehicle positional variations.

The simulation is done for the studied IPT system regulated to deliver $P_{out} = 8kW$ to the secondary side. All simulations are performed for various overlapping

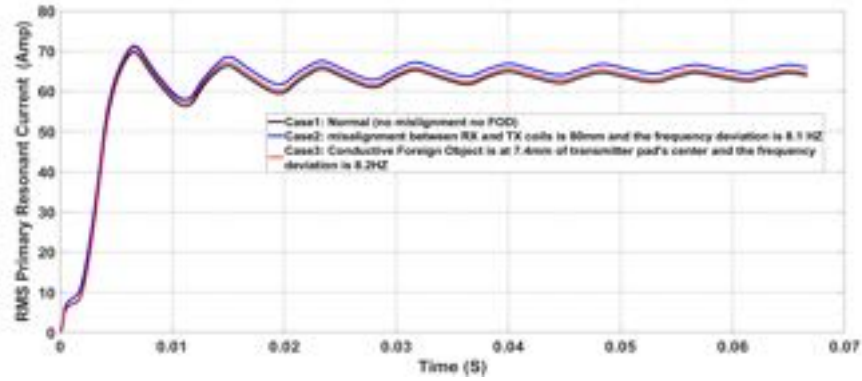


Figure 2.19: Resonant RMS current during normal conditions, misalignment and FOD maximum frequency deviation of 8Hz.

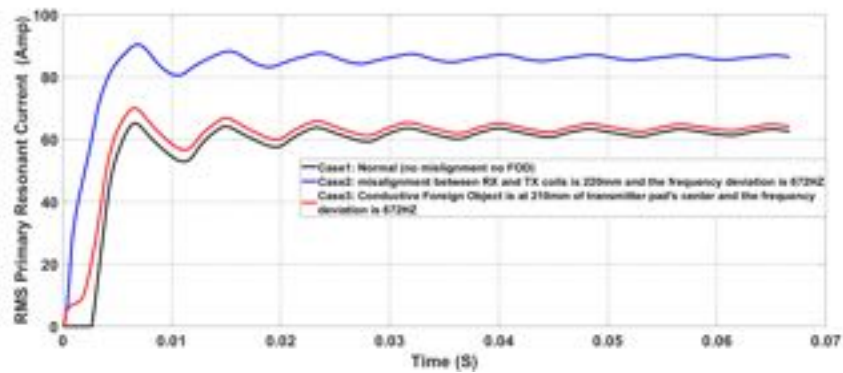


Figure 2.20: Resonant RMS current during normal conditions, misalignment and FOD maximum frequency deviation of 672Hz.

ranges of frequency deviation. The results show that the RMS value of the primary resonance current for the misalignment case increases more than the corresponding current for the FOI case to have a constant power transfer level to the secondary side. Figures (2.19 and 2.20) show the simulation results for the two extreme values of overlapping range of frequency deviation ($8Hz$ and $672Hz$). As it can be seen from the results, the RMS value of the primary resonant current for the misalignment case significantly increases; while in case of the FOI for both frequency deviations ($8Hz$ or $672Hz$), the corresponding current does not change so much.

Table 2.2: Specifications of IPT System and inductances of FOI and Misalignment

Frequency Deviation	Inductance (μH)	Normal	Misalignment	FOD
672Hz	Primary (L_p)	172	161.32	170.2
	Secondary (L_s)	172	161.29	170.45
	Mutual (L_M)	57.78	12.88	55.75
8Hz	Primary (L_p)	172	168.48	170.89
	Secondary (L_s)	172	171.46	170.88
	Mutual (L_M)	57.78	49.28	57.62

2.10 Speed analysis of the proposed FOD method

To measure the primary resonance frequency, the primary resonance current is measured and used by a timer or counter as an external input clock. The time/counter counts the number of external clock cycles within a specific sampling time period.

This can be expressed as follows:

$$N_{cyc} = \frac{T_s}{t_{cyc}} \quad (2.10)$$

where N_{cyc} is the counted number of cycles within a sampling period T_s , sampling frequency is therefore $f_s = 1/T_s$, $t_{cyc} = 1/f_r$ is the time period of the resonant current.

$$N_{cyc} = f_r T_s \quad (2.11)$$

Therefore, considering (2.11), the minimum frequency deviation is dependent on the value of sampling time period as follows:

$$df_{min} = \frac{f_r}{N_{cyc}} = \frac{1}{T_s} = f_s \quad (2.12)$$

According to (2.12), it can be inferred that the greater the sampling time period is, the more accurate the resonant frequency measurement will be, as a result, the lower the FOD speed. For instance, for the sampling time period of 1 ms and 10 ms, frequency deviation will be more than 1kHz and 100Hz respectively. In other words, the resonance frequency measurement has natural errors of 1kHz and 100Hz because of the sampling time period. This means that resonance frequency can be measured with a higher speed but with a greater error or vice versa. Therefore, a compromise between accuracy and speed for FOD method should be met.

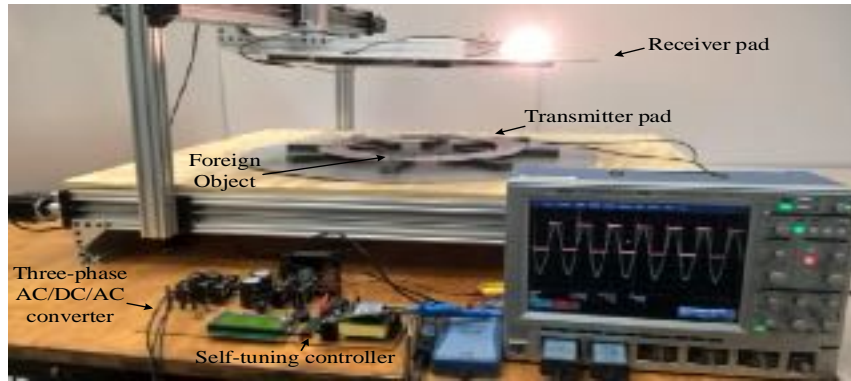


Figure 2.21: Inductive Power Transfer Experimental set-up.

Table 2.3: IPT system specification

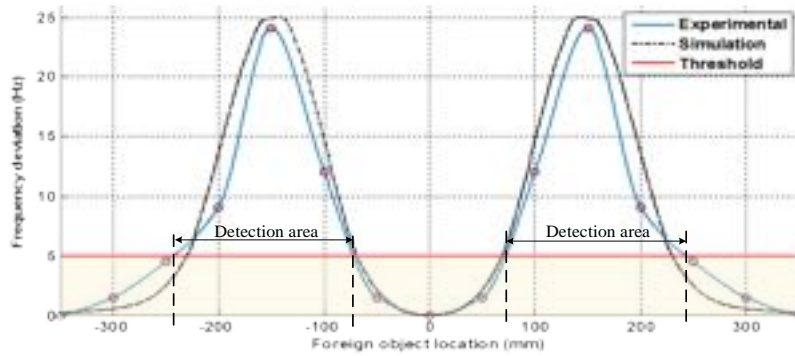
Parameter	Value
Gap distance	200 mm
transmitter pad diameter	700 mm
Primary/Secondary self inductance (L_p, L_s)	172 μ H
Compensation capacitors (C_p, C_s)	120 nF
IPT designed resonance frequency (f_r)	35 kHz
AC Input voltage (V_{ac})	120 V
Input AC frequency (f_{ac})	60 Hz

2.11 Experimental Analysis

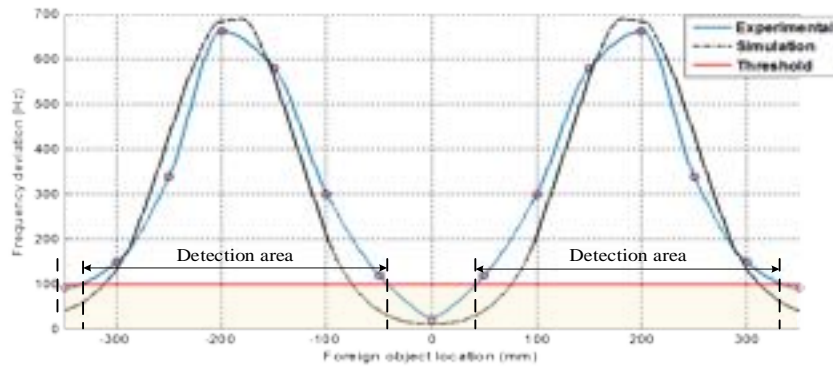
Foreign object detection proposed in this chapter is implemented on an IPT case study system for a 5-cent coin and beverage can. The experimental test bed for the proposed FOD and misalignment methods is shown in Fig. 2.21. It consists of a primary resonant converter, self-tuning resonant controller, Lecroy oscilloscope, transmitter and receiver pads, and compensation tanks. The FOD method is applied on the IPT set up with the specifications given in Table 2.3. As mentioned earlier, the self-tuning controller generates switching frequency in order to synchronize the resonance converter to an IPT-system's operating resonance frequency. The proposed FOD scheme uses the same resonance frequency measured by a self-tuning controller, and compared to the nominal value to detect FOI. Once the frequency deviation exceeds the defined threshold, the controller shuts down the IPT system by blocking the switching signals.

2.11.1 Verification Of The Proposed FOD Method For Two Case Studies: 5-Cent Coin And Beverage Can

The experiments are done for a 5-cent coin and beverage can as two different conductive objects with different sizes. Resonance frequency measurements using a self-tuning controller are carried out for different positions of the 5-cent coin and the beverage can with respect to the center of the primary power pad as given in Figs. 2.22a and 2.22b. As it can be seen from Fig. 2.22, the experimental results agree well with 2D FEA simulation results. Moreover, it shows that the maximum frequency deviation that can be caused by the 5-cent coin in the charging area is 24Hz, however, for the beverage can, the maximum possible frequency deviation is 660Hz. The FOD controller with 200ms detection speed can detect 5-cent coin in almost 49% of possible locations on a primary power pad, and for the beverage can the maximum detection area by controller with 10ms sampling time period



(a)



(b)

Figure 2.22: Experimental results achieved by the proposed FOD method (a) 5-cent coin (49% detection area) with 200 ms sampling time (b) Beverage can (with 82% detection area) with 10 ms sampling time.

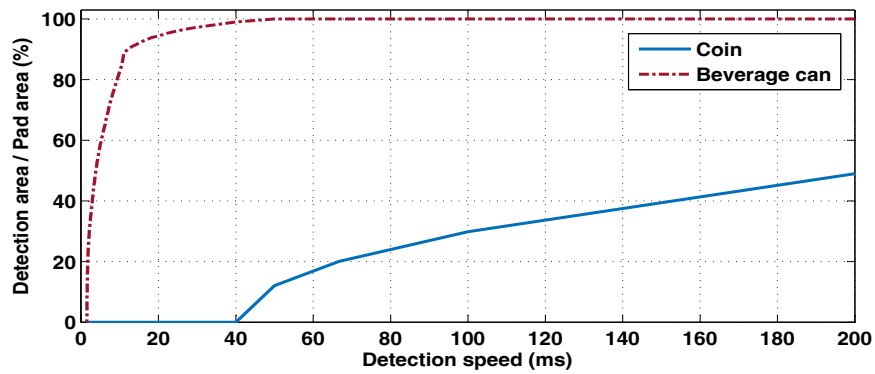


Figure 2.23: The plot of the detection area as function of detection speed for two tested foreign objects.

is 82%. It shows that with the defined detection speed for both tested objects, the detection speed of the beverage can is 20 times that of the 5-cent coin with a higher detection probability (82% in comparison with 49%). Figure 2.23 shows the plot of the detection area for the 5-cent coin and the beverage can as function of detection speed. As seen from Fig. 2.23, with the lower sampling time period, the FOD controller can't detect small size of foreign objects. It can be seen from the figure that, if the detection speed for FOD controller is tuned to 40ms, the beverage can be detected almost at every location on the primary power pad, however, with this detection speed, the 5-cent coin can not be detected at all on the primary pad.

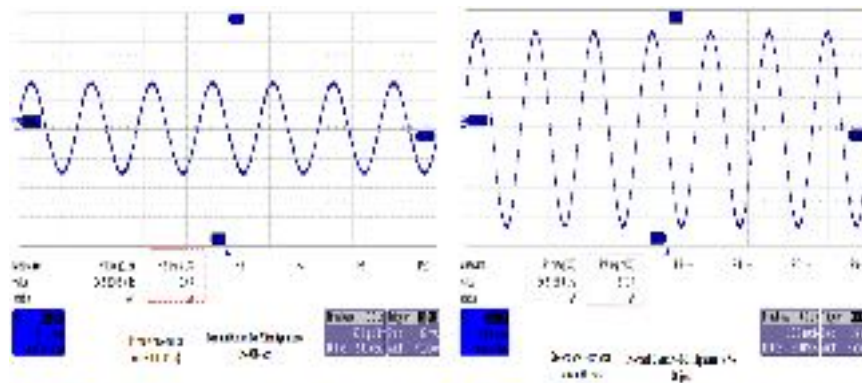
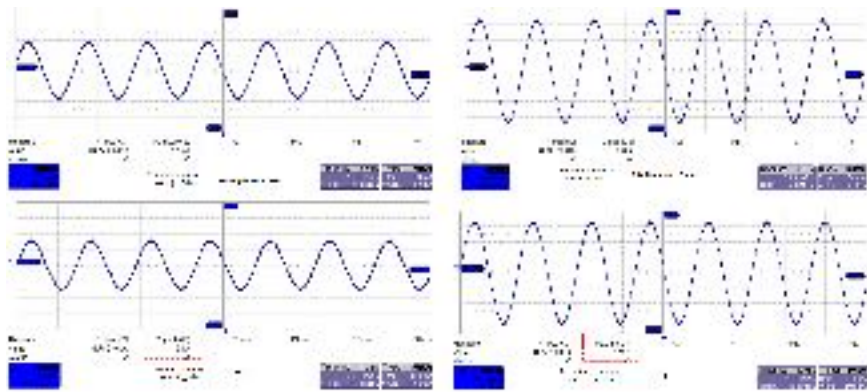


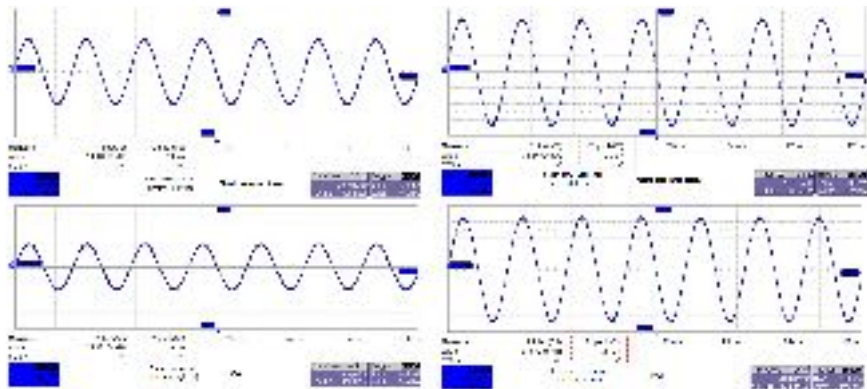
Figure 2.24: Primary and secondary currents when there is no misalignment/ no FOI.

2.11.2 Experimental Verification For Discrimination of FOI From Misalignment

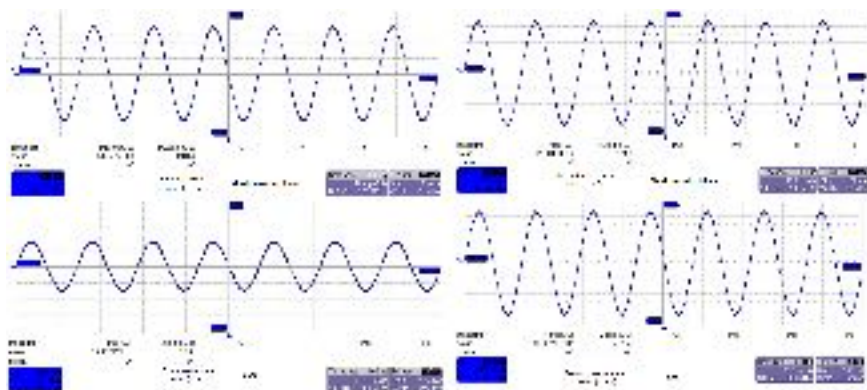
In this study, the illustrated flow chart in Fig. 2.18 is implemented using AVR programming in Atmega32a microcontroller. Current sensor installed on the primary side sends resonance current measurement to the microcontroller; accordingly, the resonance frequency and primary current magnitude are calculated online. The explained logic for discrimination is used to differentiate FOI from misalignment. Moreover, as a protective scheme, the pin(PORTA4) is defined as a shutdown



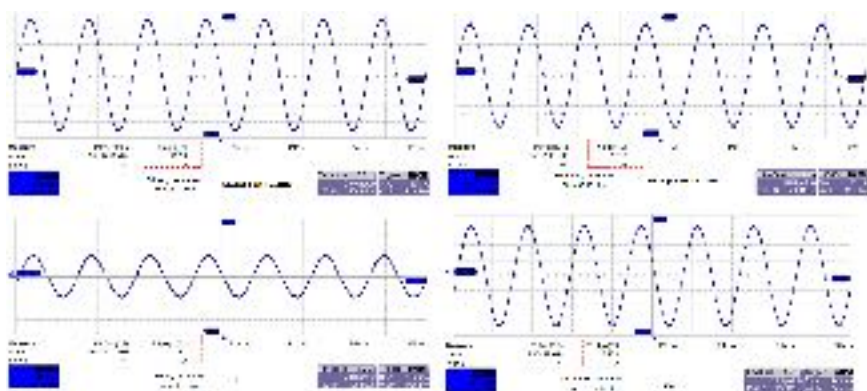
(a)



(b)



(c)



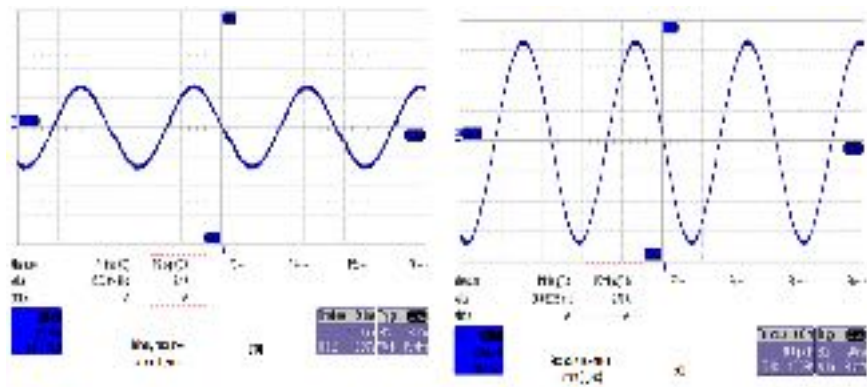
(d)

Figure 2.25: Discrimination of FOI from misalignment (a) Primary/secondary resonance currents when the new resonant frequency caused by both cases is about 34.77 kHz (b) Primary/secondary resonance currents when the new resonant frequency caused by both cases is about 34.85 kHz (c) Primary/secondary resonance currents when the new resonant frequency caused by both cases is about 35.087 kHz (d) Primary/secondary resonance currents when the new resonant frequency

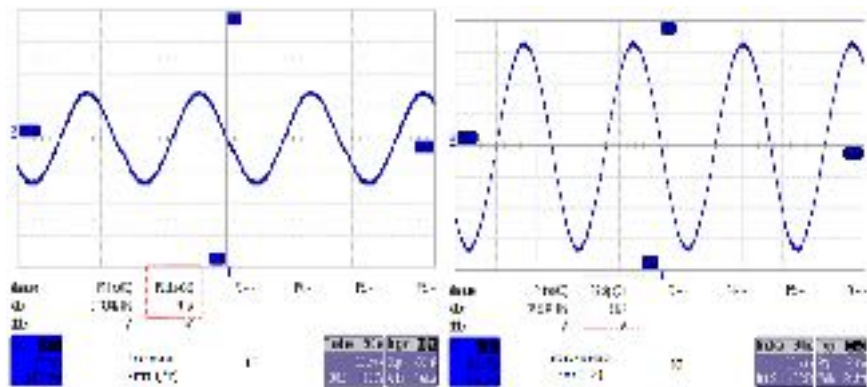
command to block resonance high frequency converter once FOI detected. Figure 2.24 shows primary and secondary resonance currents when there is no disturbance which contains information like: peak-to-peak magnitude, and resonance frequency. In all experimental results, secondary side is fixed on ($I_{Sec} = 2.7A$). In the Fig. 2.25, it is shown that in the all four cases that cause the same resonance frequency for the misalignment and FOI, the primary resonance current is significantly impacted by the misalignment than the FOI. For example, if the resonance frequency is almost $35.2kHz$ (depicted in Fig. 2.25d) for both scenarios, the primary resonance current (for the misalignment case) changes from $I_{rPrim} = 10.4A$ (Fig. 2.24) to $I_{rPrim} = 23.5A$. However, for that frequency deviation caused by FOI, the primary resonance current changes from $I_{rPrim} = 10.4A$ to $I_{rPrim} = 9.7A$ which is quite insignificant. Some other experimental results are presented in Fig. 2.26 for frequency deviations greater than the overlapping range of frequency deviation ($f_r > [8Hz, 672Hz]$). Plot shown in Fig. 2.26 confirms the consistency of the concept that FOI even with larger size does not significantly affect the primary resonance currents. Therefore, combination of resonance frequency deviation and primary side current could be an effective method to detect foreign objects and differentiate them from pads misalignment.

2.11.3 Experimental Verification of the Proposed FOD Method For Standby Mode

In the standby mode, as shown in Fig.2.15, an auxiliary single phase rectifier is proposed which can provide power as much as standby power consumption which can create resonance current in the primary side, therefore the FOD microcontroller can measure the resonance frequency even in low power mode. Figure 2.27 shows the least possible voltage and current of low-power AC/DC rectifier that can create resonance current in the primary circuit ($I_{dclink} = 776mA$, $V_{dclink} = 1.88V$



(a)



(b)

Figure 2.26: Experimental results for larger size foreign objects(a) Primary/secondary resonance currents when the new resonant frequency caused by FOI is about 36.033 kHz (b) Primary/secondary resonance currents when the new resonant frequency caused by FOI is about 37.306 kHz.

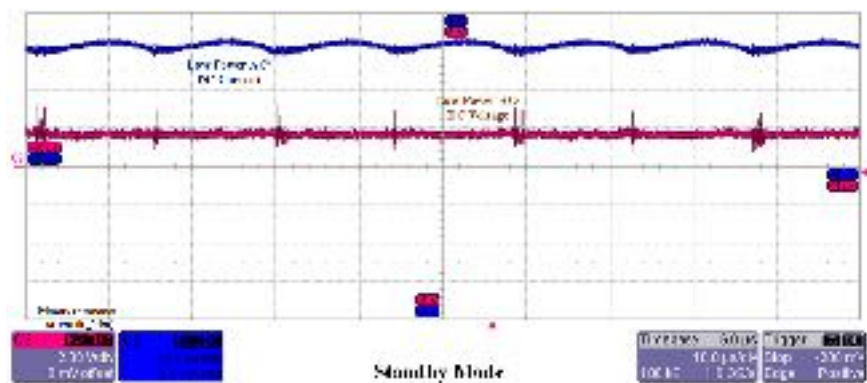


Figure 2.27: Primary side DC Link current and voltage (standby mode Consumption).

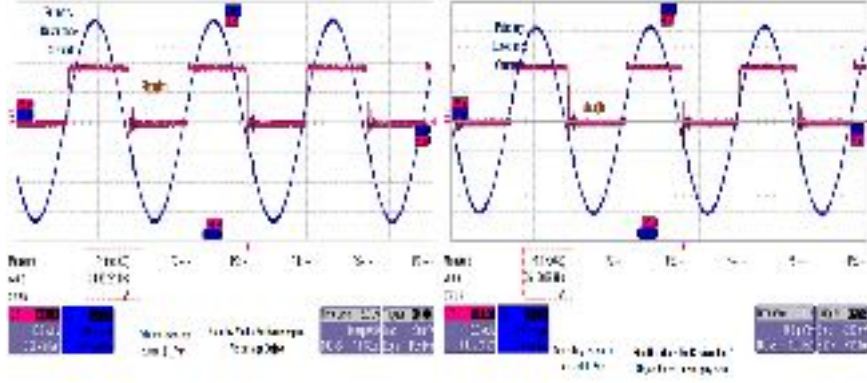


Figure 2.28: Primary resonance current (i_r) along with switching signal of converter (S_A) with/without foreign conductive objects.

which means that $P_{Standby} = 1.458W$ is the needed no-load power of the IPT system to have resonance current). Two cases with/ without foreign object are experimentally investigated for standby mode, and the results are shown in Fig. 2.28. As seen from the result, resonance frequency changes from $f_r = 34.95kHz$ to $f_r = 36.42kHz$ which confirms that proposed FOD method using online measurement of resonance frequency is independent of IPT system's operating modes.

2.12 Summary

A sensoreless technique based on resonance frequency deviation is introduced to detect conductive foreign objects in charging areas. The proposed method can be implemented on self-tuning controllers that use the IPT-system resonance frequency for switching frequency generation, therefore, this eliminates any need for extra sensors or structures. The FOD method can be applied either in low-power mode (standby) or in operational mode. Furthermore, the primary resonance current is introduced as the complementary signal to address the proposed FOD method's weakness to distinguish between the smaller conductive objects and vehicle positional variation. It is shown that the primary resonance current increases more for a misalignment case than FOI. The proposed FOD method is applied on the IPT system to detect a 5-cent coin and a beverage can, and the results have

shown that the FOD method is fast in detection of larger conductive objects (as tested on the beverage can) than smaller size conductive objects (as tested on the 5-cent coin). Experimental tests have further shown that the lower the detection speed, the greater the detection area, as a result, the smaller foreign objects detection can be realized. Also, a couple of experimental verification is done for discrimination of FOI from misalignment for a wide range of overlapping resonant frequencies, and the results have shown that the primary resonant current deviation is an effective way to differentiate these two scenarios.

CHAPTER 3

**VIRTUAL INERTIA-BASED MULTI-POWER LEVEL
CONTROLLER FOR INDUCTIVE ELECTRIC VEHICLE
CHARGING SYSTEMS**

3.1 Introduction

Generally, grid-connected EVs' chargers can be classified into two major groups: convectional plugged-in chargers, and wireless power transfer (WPT) chargers. WPT chargers offer many benefits compared to the conventional chargers namely, comfortably, elimination of drivers' interaction in the charging process, not affected by rain, dust etc, and gaining the public acceptance of EV adoption. Recently, so many researches primarily focused on advancing the design and power controller have been reported on inductive EV charging systems to realize WPT chargers [1]. In [56] for power transferability and the efficiency enhancement, a sequential procedure of IPT design is proposed; simultaneously considering electrical and magnetic parameters, however, it necessitates complex and cumbersome computations. Some researches are focused on addressing load variation issues of IPT systems as it can dramatically affect the efficiency due to off-resonance operation. Reference [57] proposed a dual-stage Z-source resonance converter using Phase Shift Modulation (PSM) for load regulation and power factor correction purposes. However, PSM reduces the efficiency due to hard switching, unpredictable switching states and unbalanced shoot through states over a period. To realize maximum power transfer rate during charging operation, an IPT constant-power battery charger is proposed in [58] by adding a switch-controlled capacitor in the secondary side; providing the impedance match between IPT and load. Its drawbacks are increased number of switches as well as the components, and reduced reliability. The design of an IPT multi-power controller with main focus on simplicity and low cost without compromise on the efficiency is missing in the

literature as proposed in this paper

From inertia perspective, replacement of conventional rotating synchronous gen-

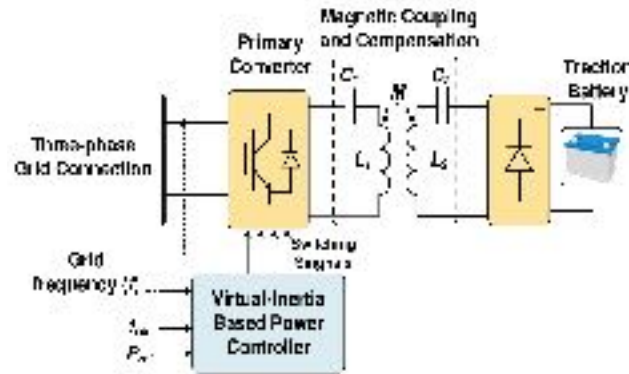


Figure 3.1: Representation of the VIC concept in an inductive EV charging system.

erator with converter interfaced resources has changed the grid inertia response [59]. Traditionally, inertial response to grid dynamic is an inherent characteristic; this allows a conventional automatic generation control (AGC) ([60]) to damp the frequency oscillation. However, with the increased penetration of renewable energy sources (RES), electric grid could suffer from a reduced inertia, deteriorating the frequency stability [59]. To increase virtual inertia of converter interfaced RES in microgrids, several methods have been proposed such as fuzzy-based VIC [61], PID-based VIC [62], virtual inductance controller [63], and generalized droop control-based VIC [64]. Different studies have implemented VIC using different techniques namely: derivative technique [65], the rate of change of rotor speed [66], rate of change of frequency (ROCOF) [67], swing equation based model [68–70], power-frequency response model and synchronous machine model [71].

In addition to the RES integration, the growing number of electric vehicle can also cause the low inertia issue. For conventional plugged-in chargers, several strategies have been proposed such as limiting EVs' charging rate [72], implementing a standard-compliant fast primary frequency control [73], and VIC [74, 75]. In [76], Suul et al developed a virtual synchronous machine-based control for plugged-in chargers enabling their online participation in frequency control and local loads supply. Reference [77] presented a numerical analysis to show how charging sta-

tion equipped with virtual synchronous-based controller can contribute to frequency support in a microgrid. In [78], Latif et al studied the impact of plug-in hybrid EV (PHEV) participation on damping deviation of both frequency and tie-line power in two-area interconnected microgrid using non-integer controllers. In contrast, no research has been carried out for VIC implementation on wireless chargers.

Unlike the conventional PWM and PSM methods which regulate the duty cycle or shift phase of inverter's legs through implementation on expensive digital platforms such as DSP and FPGA[56, 79–81], this paper presents far simple and cost-effective controller. The proposed multi-power level controller is designed through simplified digital circuits which can modulate the power transfer rate by tuning the frequency of energy injection/regeneration to the IPT systems. The proposed controller has effective application in IPT's dynamic environment due to its self-tuning feature, which can set IPT to different power levels according to the grid need, load variation, and misalignment condition. Although the proposed multi-power level control leverages similar advantages such as soft-switching operation, self-tuning capability, low switching stress etc, the proposed IPT power controller's major novelty lies in the simplified and cost-effective design, high speed due to low propagation delay in logic gates, and high efficiency.

Moreover, the VIC implementation on IPT chargers has not been investigated yet. The virtual inertia control integrated into the proposed multi-power level controller is thoroughly studied on the IPT charging power level(Fig. 3.1). This paper, as the extension of [82], presents the experimental validation for the virtual inertia-based control on IPT charging systems in an actual small-scale power grid in detail. It should be noted that "energy injection level" and "power transfer level" are used throughout the paper, and both convey the same meaning.

This paper is organized as follows: first, the VIC is formulated using power-frequency model in the section 3.2. A multi-power level controller is proposed in

the section 3.3. The simulation results for the controller is presented in the section 3.5. The features of the proposed controller including the IPT power transfer level modulation based on grid dynamics, and high efficiency thanks to soft-switch conditions are all verified in the sections 3.6 and 3.7. A testbed for experimental validation is comprised of an IPT case study connected to a LabVolt system as the actual grid emulator.

3.2 Power-Frequency Model Formulation

Equation (3.1) explains the inertia of power system by representing the relation between mechanical power, electrical power, and angular speeds:

$$\Delta P = P_{Mech} - P_e = 2H \frac{d\omega}{dt} + D \omega \quad (3.1)$$

where P_{Mech} is the mechanical power produced, P_e is the electrical load seen by generator, H is the normalized inertia constant of the machine, D is the damping coefficient of the synchronous generator and ω is the angular frequency of the grid. Conventionally, a supply-demand gap in power grid caused by load increase/decrease is compensated by the kinetic energy stored in the rotor. In future electric grid with high penetration of EVs and other converter-based renewable energy resources, the high inertia conventional generators will not be adequate to keep the grid's frequency within permissible ranges, consequently resulting in huge frequency oscillation. In this study, inductive electric vehicle charging systems is designed to follow the power-frequency model equation (3.1), which increases the IPT systems' inertia. The expected benefit of applying VIC on EV systems is adapting EVs' load requirements exactly based on grid dynamics.

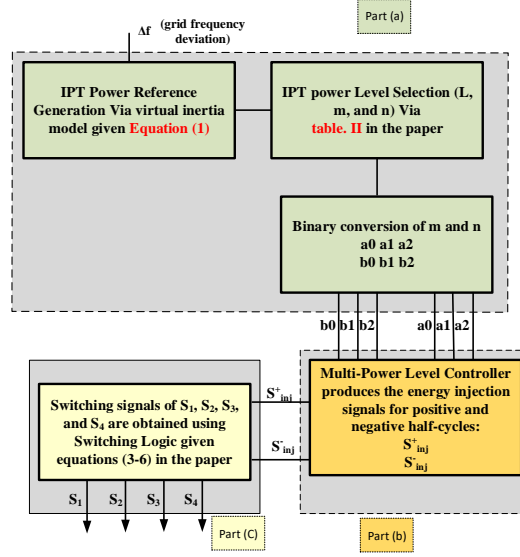


Figure 3.2: The flowchart of the virtual inertia based IPT power controller

3.3 IPT multi-power level resonant controller

Among many compensation configurations, series compensated are commonly used IPT systems, as the primary current can be easily controlled in such a topology. The output power of these IPT systems can be easily regulated by adjusting the number of quantum of energy injection pulses. The flowchart represented in Fig. 3.2 gives an easy and quick diagrammatic view which shows what parts and how they are related to each other in the proposed virtual inertia-base IPT controller. As presented in the flowchart, this proposed controller is composed of three major sections: (a) power reference generation for IPT system through VIC referring to the power-frequency model (3.1), (b) multi-power level controller(subsection 3.3.1) which gets the power reference value from VIC and sets IPT's power transfer level based on new reference and (c) switching logic as shown in subsection 3.3.2. The proposed power transfer controller is explained in details, and the design for that multi-power level controller[82] is presented.

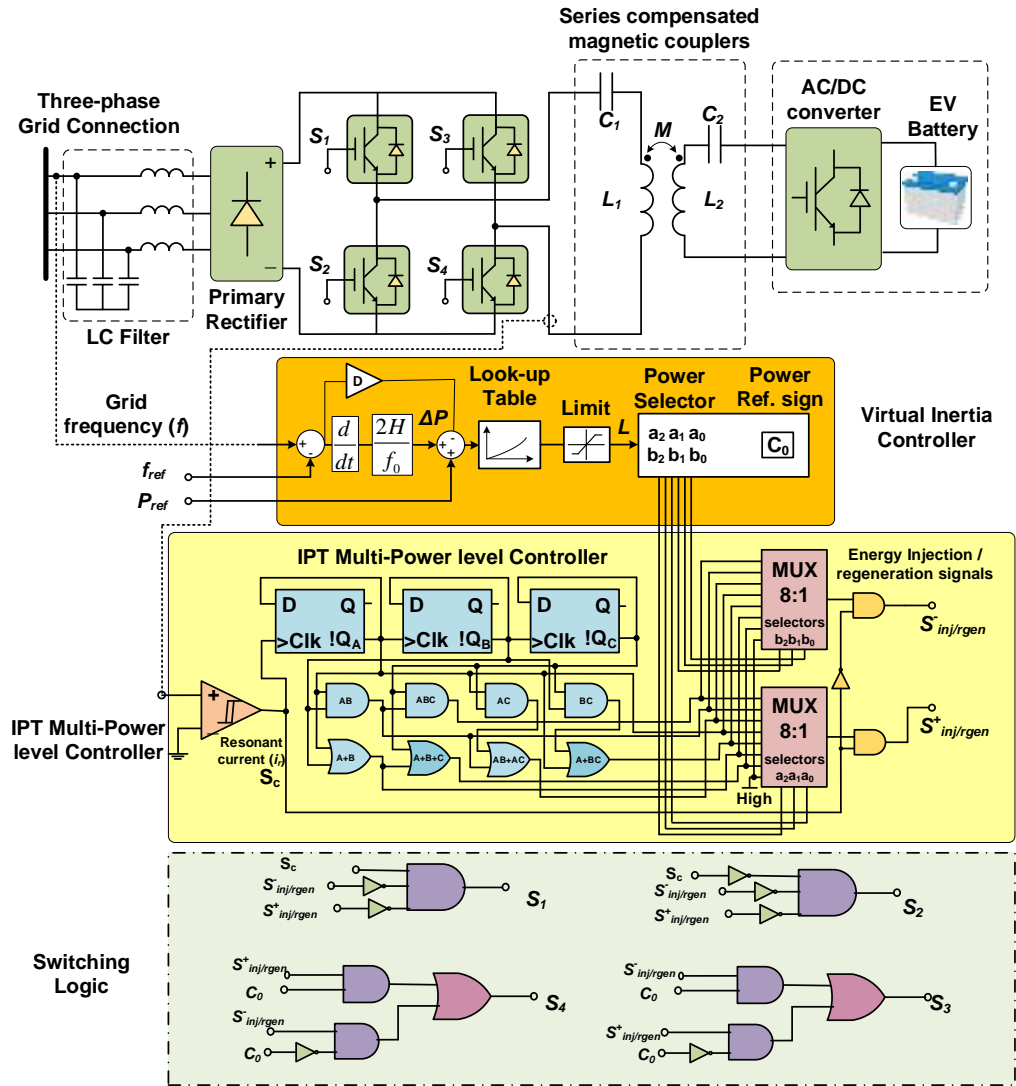


Figure 3.3: The proposed VIC for inductive EV charger.

Table 3.1: Reference signals with corresponding Boolean algebra using A, B, C signals

No. of pulses	Logic	Pulse No. included
1	ABC	1
2	AB	1,5
3	$AB + AC$	1,3,5
4	A	1,3,5,7
5	$A + BC$	1,2,3,5,7
6	$A + B$	1,2,3,5,6,7
7	$A + B + C$	1,2,3,4,5,6,7
8	CLK	1,2,3,4,5,6,7,8

Table 3.2: Power levels with corresponding number of positive and negative pulses, and duty cycle

Power Level #	Number of power transfer pulses			Duty-Cycle (D)
	pos. (m)	neg. (n)	Tot. (L)	
1	1	0	1	0.0625
2	1	1	2	0.1250
3	2	1	3	0.1875
4	2	2	4	0.2500
5	3	2	5	0.3125
6	3	3	6	0.3750
7	4	3	7	0.4375
8	4	4	8	0.5000
9	5	4	9	0.5625
10	5	5	10	0.6250
11	6	5	11	0.6875
12	6	6	12	0.7500
13	7	6	13	0.8125
14	7	7	14	0.8750
15	8	7	15	0.9375
16	8	8	16	1

3.3.1 Control Logic Design

To regulate the power transfer value, the amplitude of primary resonant current needs to be changed. To do so, the power transfer rate should be changed through transferring energy in positive and negative half cycles of primary resonant current. In this design, primary resonant current with sixteen half cycles including 8 positive and 8 negative half cycles is assumed as a control signal. Considering each half-cycle of the control signal as one energy pulse, power transfer can happen in either of positive or negative energy pulses. Referring to Fig. 3.3, the resonant current (i_r) is measured and feedback to the comparator logic gate as an input, then i_r is compared to 0 value in the comparator gate and produces a signal which is defined as $sign(i_r)$, The signal $sign(i_r)$ is 1 in positive half-cycles (where $i_r > 0$) and 0 in negative half-cycles (where $i_r < 0$). This signal ($sign(i_r)$) is then used as the clock Clk for the first D-flip flop, and its output is named $\overline{Q_A}$. Signal $\overline{Q_A}$ is then used as the clock for the another series D-flip flop, and its output is named $\overline{Q_B}$ which is used as the clock for the third series flip flop and its output is defined $\overline{Q_C}$. Technically, the frequency of CLK signal are divided after either of the three-series D-type flip-flops by factors of 1/2, 1/4 and 1/8 as illustrated in

Fig. 3.4. These signals are then ANDed with CLK signal to produce the power transfer reference signals (A , B , and C) which are given as follows:

$$A = CLK \cdot \overline{Q_A} \quad B = CLK \cdot \overline{Q_B} \quad C = CLK \cdot \overline{Q_C} \quad (3.2)$$

Applying the Boolean operators shown in Table 3.1 via logic gates (AND and OR) on A , B , and C signals, eight reference signals for energy injection in positive half-cycles are produced which contains 1 to 8 energy pulses as presented in Fig. 3.5. The complementary signal of CLK is defined \overline{CLK} signal; the CLK and \overline{CLK} signals are used for positive and negative half-cycle of energy injection respectively. Similarly, by using \overline{CLK} as a base along with the Boolean operations given in Table 3.1, the eight reference signals for the negative half-cycles can be achieved in the same manner. In total, sixteen different power levels are achieved by symmetric combination of the derived reference signals(8 reference signals of positive half cycles and 8 reference signals of negative half-cycles) as shown in Table 3.2 to propose the multi-power level controller as presented in Fig. 3.3. As an example, when IPT's power level is 5 (referring to Table 3.2), it means that three pulses of energy injection happens in positive half cycle, and two energy injection pulses occurs at negative half cycle. Therefore, the power transfer rate given as D (in the Table 3.2) is calculated by dividing the number of power level by total number of pulses; for this case is $\frac{5}{16}$. These sixteen signal references are routed to two

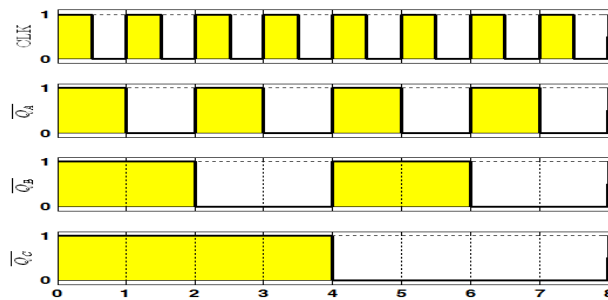


Figure 3.4: Reference CLK (used as the clock signal for the first D-type flip-flop), and inverted outputs: $\overline{Q_A}, \overline{Q_B}, \overline{Q_C}$ of three cascaded flip-flops (see Fig. 3.3)

multiplexers as inputs. The selector bits value (a_0, a_1, a_2 and b_0, b_1 and b_2) of two multiplexers (shown in Fig. 3.3) obtained via the VIC determine the pair of the

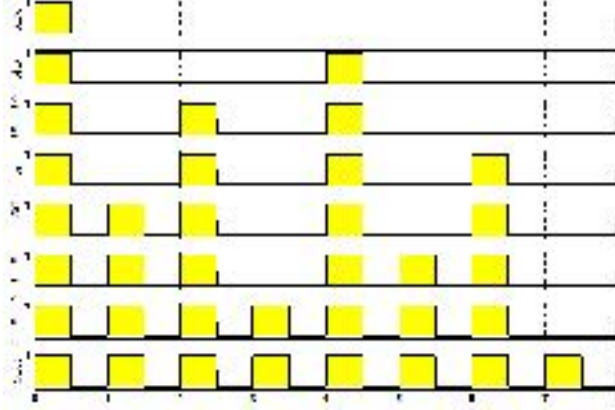


Figure 3.5: Reference signals with 1 to 8 pulses obtained using A , B , and C (for more details refer to Table 3.1)

sixteen reference signals to be selected as energy injection pulses for negative and positive half cycles which are defined $S_{inj/regen}^-$ and $S_{inj/regen}^+$ respectively. The details of switching logic using these energy injection/regeneration pulse is given in the following subsection.

Table 3.3: Switching states in different modes of IPT operation

Mode	Type	$S_{inj/reg}^-$	$S_{inj/reg}^+$	$C_0(\Delta f > 0)$	$S_c(i_{res} > 0)$	S_1	S_2	S_3	S_4
1	Energy Injection (G2V)	0	1	1	1	1	0	0	1
2	Energy Injection (G2V)	1	0	1	0	0	1	1	0
3	Energy regeneration (V2G)	0	1	0	1	0	1	1	0
4	Energy regeneration (V2G)	1	0	0	0	1	0	0	1
5	Free oscillation	0	0	-	1	1	0	0	0
6	Free oscillation	0	0	-	0	0	1	0	0

3.3.2 Switching control Logic

The switching logic of four switches (green colored box in Fig. 3.3) for primary resonant converter is designed based on: energy injection signals generated by multi-power level controller for positive current half-cycles (S_{inj}^+) and negative current half-cycles (S_{inj}^-), and resonant current direction (S_c) as given in Table 3.3. By defining one added variable named C_0 as the power flow direction of IPT system in VIC(referring to the gold colored box in Fig. 3.3), the IPT' primary converter can operate bidirectionally (either in G2V or V2G operation modes).

Whenever, the grid frequency increases ($\Delta f > 0$) then $C_0 = 1$ and IPT operates in G2V mode, inversely, as the $\Delta f < 0$ then $C_0 = 0$ and the IPT charger establishes the V2G connection. Table 3.3 presents the five operation modes of the converter considering the sign of the mentioned variables. For this controller, IPT charger can run in three operation modes including: energy injection (G2V), energy regeneration mode (V2G), and free oscillation mode. Finally, the switching logic are designed based on energy injection/regeneration signals of positive current half-cycles (S_{inj}^+) and negative current half-cycles (S_{inj}^-), resonant current direction (S_c), and power reference sign (C_0) as given in Table 3.3. The switching logic of the switches (S_1 , S_2 , S_3 , and S_4) are presented in equations (3.3), (3.4), (3.5), and (3.6) which are combined in such a way to satisfy the switches states given in the Table 3.3.

$$S_1 = \overline{S_{inj}^+} \overline{S_{inj}^-} S_c \quad (3.3)$$

$$S_2 = \overline{S_{inj}^+} \overline{S_{inj}^-} \overline{S_c} \quad (3.4)$$

$$S_3 = S_{inj}^+ C_0 + S_{inj}^- \overline{C_0} \quad (3.5)$$

$$S_4 = S_{inj}^- C_0 + S_{inj}^+ \overline{C_0} \quad (3.6)$$

Fig. 3.6 is also added which shows corresponding circuit of all the six modes given in the Table 3.3. As it can be seen from Fig. 3.6, in the *Mode1*, IPT operates in energy injection mode as the voltage across LC tank and the resonant current are both in positive half cycles. In *Mode2*, the voltage across LC tank is negative, and the resonant current is in its negative half-cycle which again both current and voltage are in phase and the power transfer is from grid to load. In the *Mode3*, *Mode4*, IPT operates in energy regeneration mode as the voltage across LC tank and the resonant current are out of phase, and energy is released from EV battery to grid. In *Mode5* and *Mode6*, the IPT operates at free oscillation which means the output voltage of the resonant converter is zero, and the energy stored in LC tank is being transferred toward secondary, and the resonant current reduces in this mode until next injection/regeneration pulse is received.

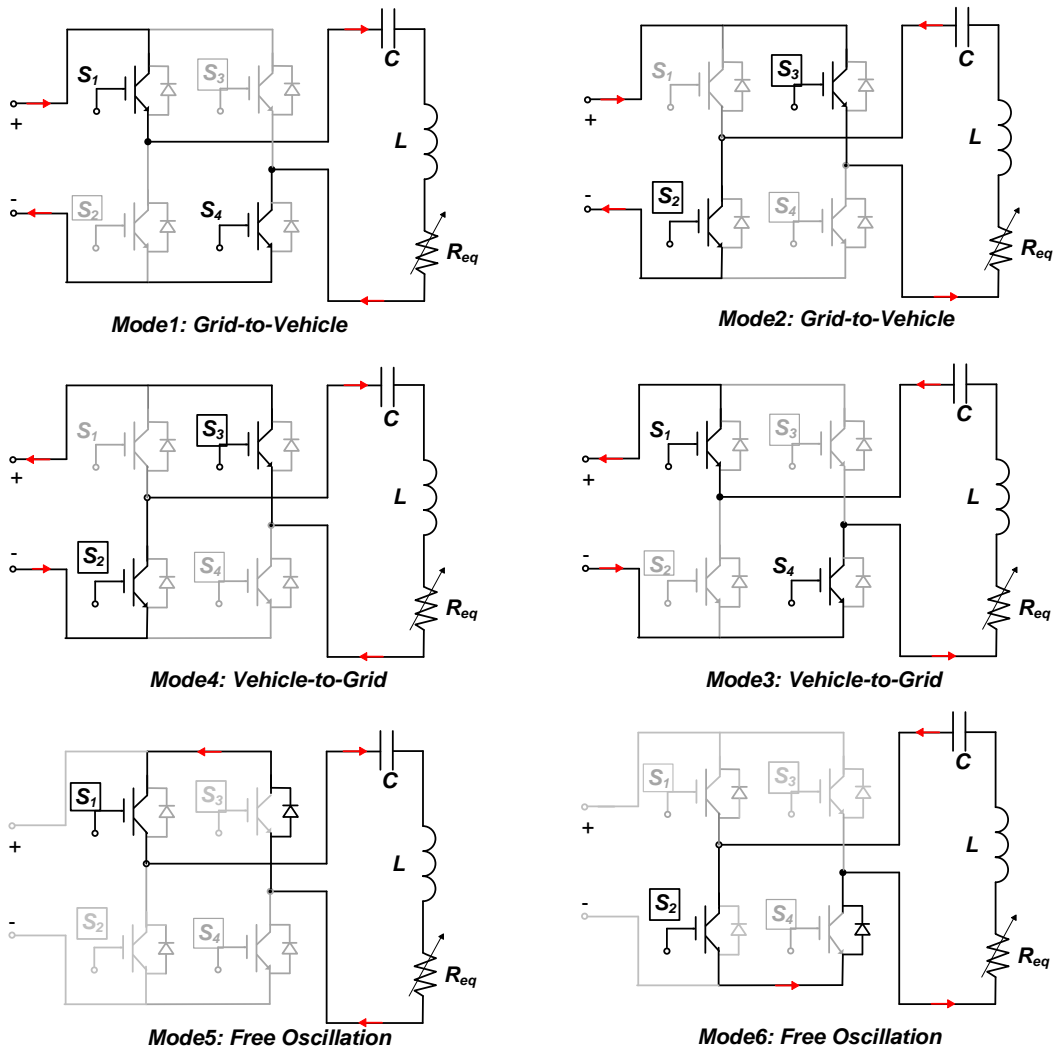


Figure 3.6: IPT's primary resonant current path for six operation modes (referring to Table 3.3)

3.3.3 Fundamental Harmonic Analysis of converter's Voltage

To calculate the power transfer rates in different mentioned levels, Fundamental Harmonic Approximation (FHA) method is used. Applying the FHA method, the fundamental component of converter's voltage is derived at the resonance frequency ω as follows (equation (8.1)):

$$V_1 = \frac{\omega}{8\pi} \int_0^{\frac{16\pi}{\omega}} v_{prim} \sin(\omega t) dt \quad (3.7)$$

where v_{prim} is the output voltage of the primary DC/AC converter, ω is the resonance frequency, and V_1 is the converter's fundamental harmonic component. Considering m and n as the positive and negative energy injection in negative and positive half-cycles of resonant current respectively; the output voltage can be rewritten in a discrete way as shown in equation 3.8:

$$v_{prim} = \begin{cases} |V_{dc}| & \frac{2(j-1)\pi}{\omega} < t < \frac{2j\pi}{\omega}, j = 1, \dots, m \\ & \frac{2(i-1)\pi}{\omega} < t < \frac{2i\pi}{\omega}, j = 1, \dots, n \\ 0 & \text{otherwise} \end{cases} \quad (3.8)$$

Where v_{dc} is the DC-Link voltage (primary three-phase rectifier's output volt-

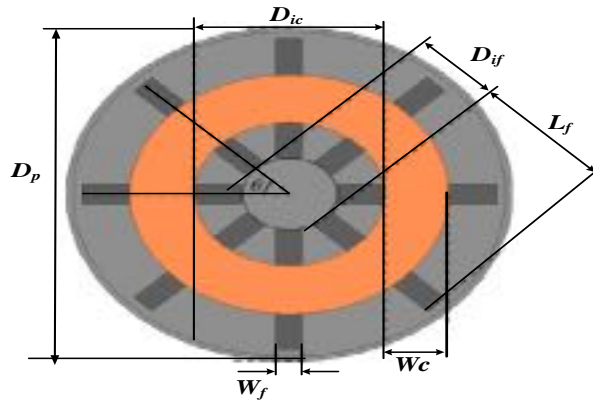


Figure 3.7: Geometrical parameter of ferrite bars, coil, and shield plate in the circular power pad

age). Equation 3.8 shows that in m and n pulse number of positive and negative half cycles, energy injection happens, and the converter's output voltage equals to $|v_{dc}|$ in all these active pulses. Regarding the sign of $|v_{dc}|$, it is positive for positive half-cycles of the primary resonant current and minus for negative half-cycles of resonant current in order to always keep power direction from grid to vehicle(G2V). As the second term of equation (3.8)), for the remaining half cycles, the output voltage of resonant converter is zero which means that IPT operates in free-oscillation mode. By substituting (3.8) in (8.1) and expanding it, equation 8.4 can be achieved:

$$V_1 = \frac{\omega}{8\pi} \left(\sum_{j=1}^m \int_{\frac{2(j-1)\pi}{\omega}}^{\frac{(2j-1)\pi}{\omega}} V_{dc} \sin(\omega t) dt + \sum_{i=1}^n \int_{\frac{(2i-1)\pi}{\omega}}^{\frac{2i\pi}{\omega}} -V_{dc} \sin(\omega t) dt \right) \quad (3.9)$$

Equation (8.4) can be simplified to equation (8.5) as follows:

$$V_1 = \frac{(m+n)V_{dc}}{4\pi} \quad (3.10)$$

As defined earlier, $D = (m+n)/16$ can be substituted in equation (8.5) and simplify it as expressed in equation (8.6).

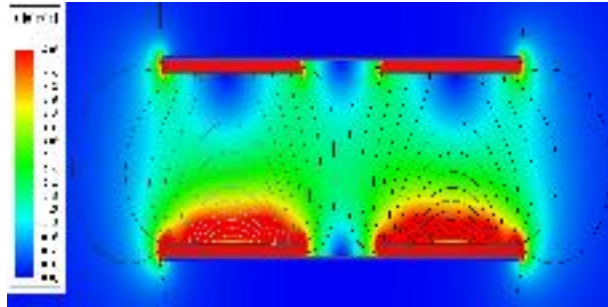


Figure 3.8: 2D-FEA Model: Magnetic plot of the IPT system

$$V_1 = \frac{4}{\pi} DV_{dc} \quad (3.11)$$

To calculate power transfer rate for this system, the fundamental harmonic of primary resonant current is calculated using equation (8.5) and expressed in equation (8.7):

$$I_{pr} = \frac{V_1}{R_{eq}} = \frac{(m+n)V_{dc}}{4\pi R_{eq}} \quad (3.12)$$

where R_{eq} (shown in Fig. 3.6) is the equivalent resistance reflected to the primary, because at resonant frequency, the compensation capacitor and secondary inductance cancels out each other. Then the output power can be presented as,

$$P = \frac{1}{2} R_{eq} I_{pr}^2 = \frac{(m+n)^2 V_{dc}^2}{32\pi^2 R_{eq}} \quad (3.13)$$

As it can be seen from equation (8.8), the m and n have direct relation to power transfer rate.

3.4 Circular IPT Case Study

A circular-pad IPT system is employed as the case study for doing experimental validation of the proposed controller. All the geometrical parameters of the circular pad presented in the Fig. 3.7 namely: spatial phase difference of ferrite bars (θ), inner diameter of ferrite (D_{ic}), width/length of ferrite bar (L_f / W_f), width of coil (W_c), are available in the paper [83]. A 2D finite element analysis (FEA) of

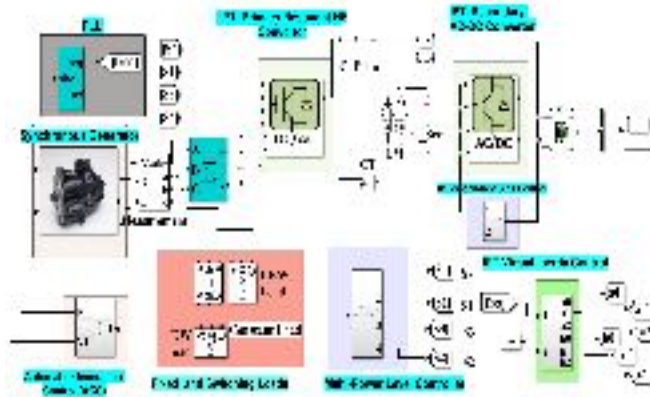


Figure 3.9: Simulation Model: synchronous generator with enabled AGC along with inductive charging systems and load

the circular IPT case study is studied to show the distribution of magnetic flux as shown in the Fig. 3.8. It is worth mentioning that the 2D-FEA results is well match with the 3D-FEA model due to symmetrical geometry of the circular power pad.

3.5 Simulation Analysis

In this section, a simulation model consists of a synchronous generator with enabled AGC, an IPT system and constant/switching loads is studied. In the numerical simulation as shown in Fig. 3.9, an IPT system is equipped with the proposed virtual inertia based multi-power level controller. The switching loads are employed in the simulation model to add and drop frequency dynamics. Table 3.4 shows the specification of the simulated model.

The response of the virtual inertia based IPT system is studied when the load

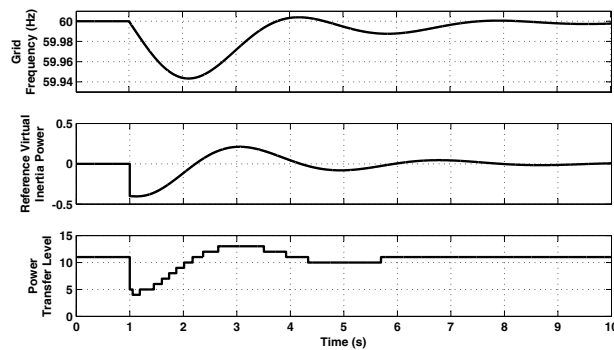


Figure 3.10: Simulation results: Grid frequency (f), power deviation(ΔP), IPT power level

changes at $t = 1s$. As can be seen from Fig. 3.10, the synchronous generator's rotor speed drops, and it takes a few seconds for the generator's AGC to recover the frequency to the rated value due to grid large inertia. The power level regulation of VIC IPT system in response to the disturbance, as well as frequency deviation plot, and the power deviation (ΔP) are also represented. Some other simulations are carried out with different inertia constants (H), the results presented in Fig.

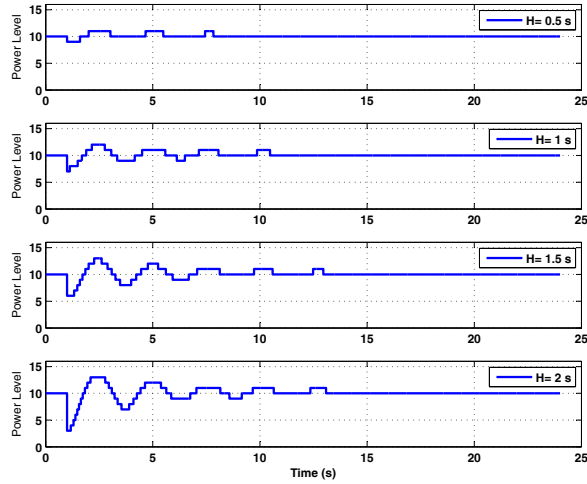


Figure 3.11: Virtual inertia response of the proposed IPT to power grid dynamics with various inertia Constants.

3.11 verifies that with larger grid's inertia constant, wider range of IPT power level owing to the proposed virtual inertia controller can participate in frequency damping.

Table 3.4: Technical specifications for IPT VIC simulation.

Parameter	Value
Generator Inertia Constant (H_{gen})	10s
Generator Damping Coefficient (D_{gen})	0.8
Virtual Inertia Constant of IPT System (H_{vir})	0.5s-2s
Virtual Damping Coefficient (D_{vir})	0.5
Droop gain (R)	0.05 %

Table 3.5: Technical specification of IPT system Set up

Parameter	Value
Gap distance	200 mm
transmitter pad diameter	700 mm
Primary and Secondary Compensation capacitors (C_p, C_s)	120 nF
Primary/Secondary self inductance (L_p, L_s)	172 μ H
AC Input voltage (V_{ac})	120 V
Input AC frequency (f_{ac})	60 Hz
IPT designed resonance frequency (f_r)	35 kHz

Table 3.6: LabVolt dynamometer/generator rating specifications

	Torque	Angular Speed	Active power
Dynamometer	$T = 0 - 3N.m$	$\omega = 0 - 2500rpm$	$P = 350W$
	Apparent Power	power factor	Angular Speed
Generator	200VA	0.8PF	$\omega = 1800rpm$

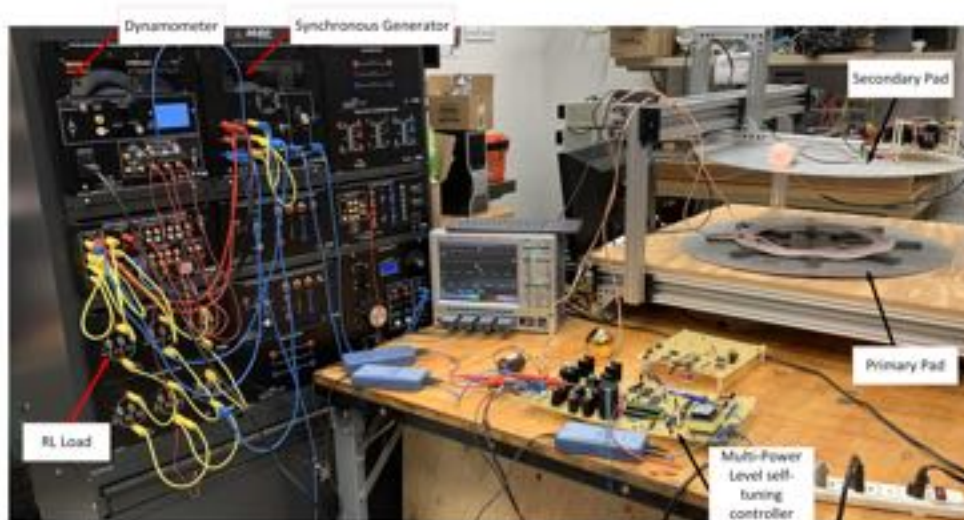


Figure 3.12: Experimental setup: Inductive Power Transfer connected to an Lab-Volt grid emulator which is comprised of synchronous generator, RL loads.

3.6 Experimental Analysis

VIC for inductive EV charging systems proposed in this paper is implemented on an IPT case study system. The experimental test bed of VIC is shown in Fig. 3.12. It consists of a primary resonant converter, multi-power-level resonant controller, transmitter and receiver pads with compensation tanks, LabVolt system which incorporates different modules including synchronous generator, four-quadrant dynamometer, and RL loads, and Lecroy oscilloscope. The microcontroller embedded programming is used to implement VIC (measuring the grid frequency and specifying the power level). The specifications of IPT, and Labvolt components are presented in this section. The Table 3.5 shows the specifications of the IPT setup which is connected to the LabVolt system. In Table 3.6, the rating parameters of dynamometer (prime mover) and generator modules of LabVolt testbed are given. The experiments for validation of the proposed VIC controller is only done for low powers due to the practical limitation of the LabVolt testbed. The power rating of the generator module in the LabVolt system is limited to 200VA which is only suitable for low power level experiments as presented in this paper. The grid frequency fluctuation is measured through the shaft encoder's TTL output accessible

in the dynamometer module of LabVolt system. In this paper, the synchronous generator module of the testbed is set to run in the clock wise prime mover mode. Frequency change is applied to the emulated grid through step by step change in R/L load (in three steps as shown in Table 3.7). The power rating and voltage of the R/L loads in the LabVolt system are 252 wat/var and 120V respectively.

TTL output's frequency of generator shaft($f_{TTL Output}$) is multiplication of

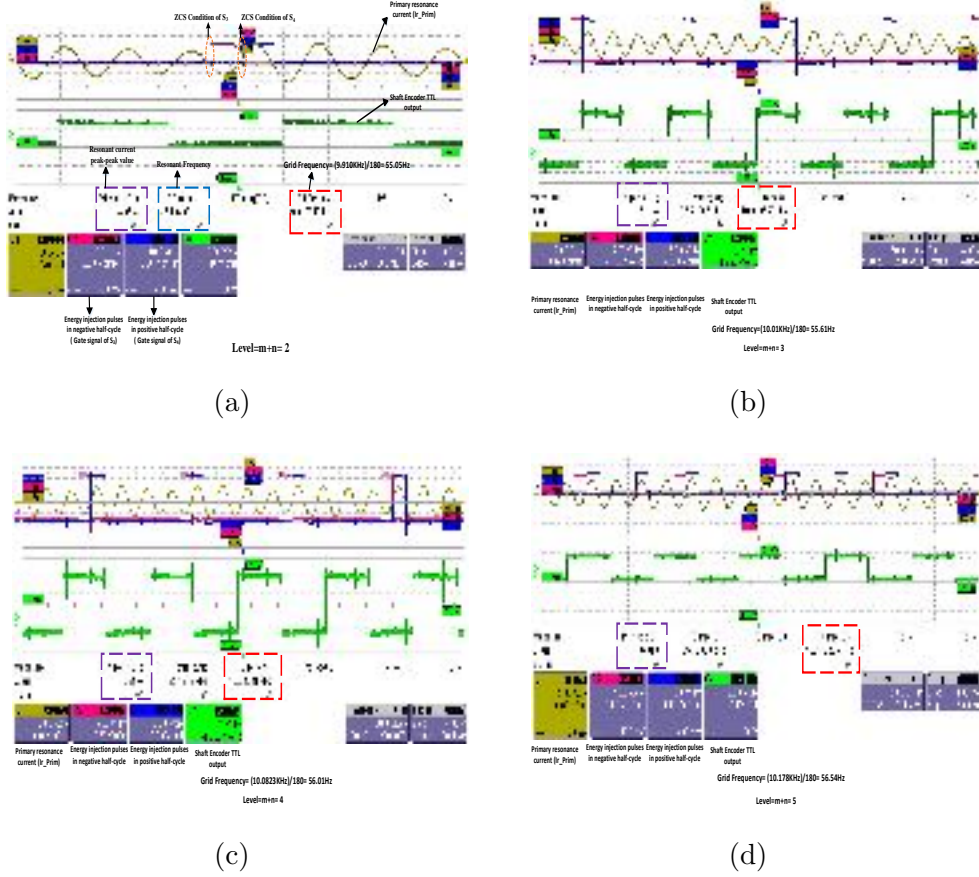


Figure 3.13: power transfer level (a) level 2 (b) level 3 (c) level 4 (d) level 5

the frequency by factor 180, i.e. for nominal frequency(f_s), its frequency is $60 \times 180 = 10800\text{Hz}$. Accordingly, for any other generator speed, the equivalent grid frequency can be calculated through (3.14).

$$f_{Eq-grid} = \frac{f_{TTL Output}}{180} \quad (3.14)$$

Table 3.7: Resistive and Inductive loads of LabVolt

R/L	step1	Step2	Step3
Resistive Load	$R = 300\Omega$	$R = 600\Omega$	$R = 1200\Omega$
	$i_R = 0.4A$	$i_R = 0.2A$	$i_R = 0.1A$
Inductive Load	$X = 300\Omega$	$X = 600\Omega$	$R = 1200\Omega$
	$i_L = 0.4A$	$i_L = 0.2A$	$i_L = 0.1A$

Where $f_{TTL\ Output}$ is the frequency of shaft encoder output accessible in the LabVolt system, $f_{Eq-grid}$ is the equivalent grid frequency of the LabVolt system as the grid emulator.

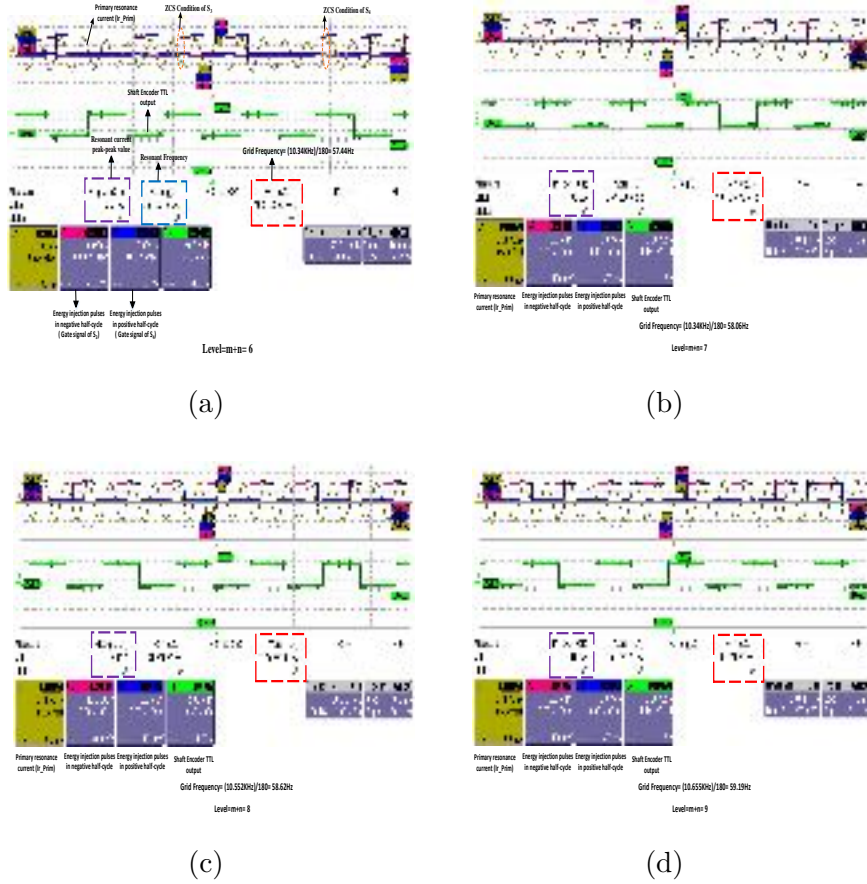


Figure 3.14: power transfer in different level (a) level 6 (b) level 7 (c) level 8 (d) level 9

Parameters P1,P2,P3, and P4 presented in the experimental results, Figs. 3.13a to 3.16c, derived from Lecroy oscilloscope are used to calculate the waveform attributes including rms value, peak-to-peak value, mean value, and frequency of signals. Moreover, F1, F2, F3, and F4 are the math functions to do math oper-

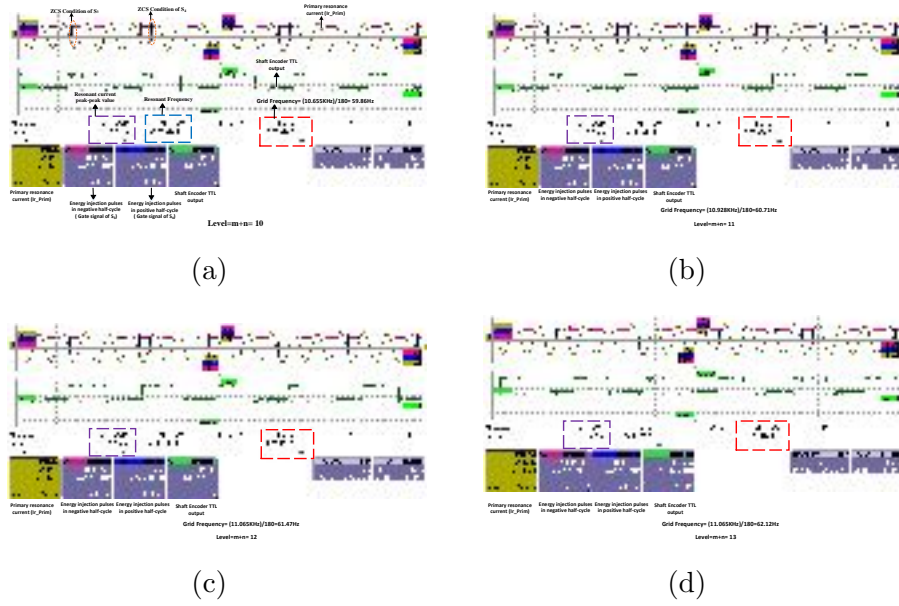


Figure 3.15: Power transfer level (a) level 10 (b) level 11(c) level 12(d) level 13

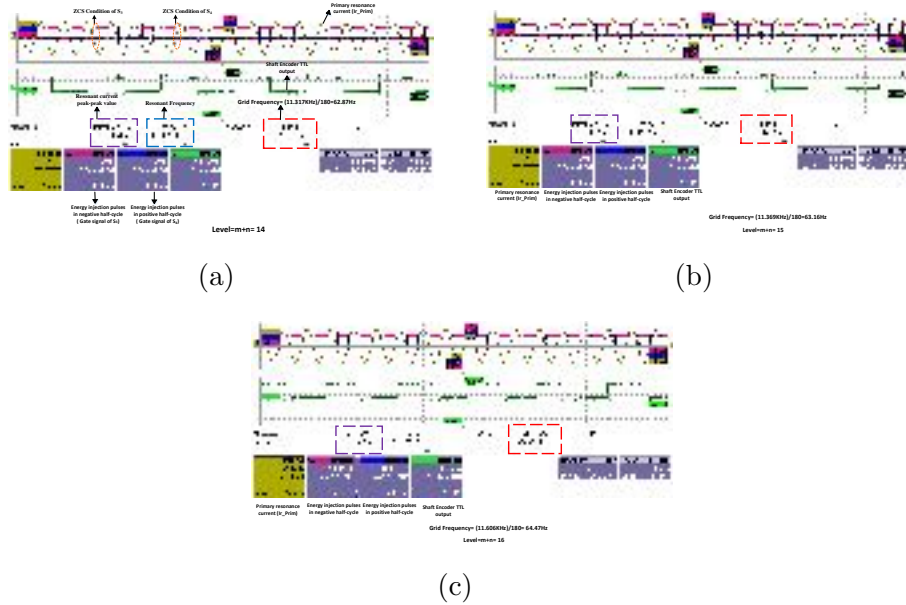


Figure 3.16: power transfer level (a) L= 14(b) L= 15 (c) L= 16

ations on channels such as multiply, fast Fourier transform, square, sum and so on. In this paper, F1 and F2 are used to multiply two channels as used in the Fig. 3.20. Finally, it should be noted that although the design of the proposed VIC power level controller is presented for bidirectional power flow control, the experiments in the paper are carried out for G2V connection.

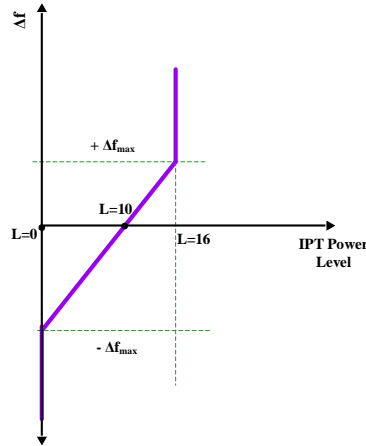


Figure 3.17: Frequency deviation VS the IPT power level number ($1\% < SOC < 99\%$)

3.6.1 VIC Implementation on IPT Multi-power Level charger

Experimental implementation for the proposed IPT multi-power level charging system with VIC which regulates the power transfer level according to the frequency deviation is presented. In Fig. 3.13a, when the shaft encoder frequency as measured by P4 ; $\text{freq}(C4)$ in the plot is 9.91 kHz, which is equivalent to grid frequency (f_{Grid}) of 55.05Hz referring to (3.14), and the IPT system is set on power level 2. This means that the energy transfer only happens in one pulse of both positive and negative half-cycle, and, the duty cycle is $D = \frac{2}{16}$. In other words, the VIC sets the IPT's power level at 2 as a response to low grid frequency, thereby reducing power transfer from the grid to the IPT system. As shown in Fig. 3.13a, the peak-to-peak value of primary resonant current measured by P1 ; $\text{pkpk}(C1)$ in the plot is 4.35A. The results of IPT power response are repeated

for grid frequencies of 55.61Hz, 56.01Hz, and 56.54Hz in Figs. 3.13b, 3.13c, 3.13d respectively. These results affirm that the energy injection level of IPT system are modified by the proposed virtual inertia-based multi-power-level controller for the set grid frequencies to level 3, level 4, and level 5 respectively. The IPT's primary currents (peak-to-peak) for those mentioned power transfer levels tuned by the VIC are 5.12A, 5.89A and 6.91A respectively. Figs. 3.14a, 3.14b, 3.14c, 3.14d, are the repeated results for grid frequencies of 57.44Hz, 58.06Hz, 58.62Hz, and 59.19Hz. Again, the results show the change of the power transfer level tuned by the virtual inertia-based multi-power-level controller. In Figs. 3.14a, 3.14b, 3.14c, 3.14d, power transfer levels of 6, 7, 8 and 9 are achieved for the set grid frequencies respectively. Their corresponding peak-to-peak value of primary resonant currents are 7.74A, 8.26A, 8.64A, and 9.66A respectively. Figs. 3.15a, 3.15b, 3.15c, and 3.15d, are the results for grid frequencies of 59.86Hz, 60.71Hz, 61.47Hz, and 62.12Hz. Again, the results show that the power transfer level is well regulated by the virtual inertia-based IPT controller, which are levels 10, 11, 12 and 13 for the set frequencies. The primary current (peak-to-peak) for these power transfer levels are 10.24A, 10.69A, 10.88A, and 11.07A respectively. As the grid frequency increases, the power transfer level as well as the primary resonant current increases which is in line with the virtual inertia strategy to synchronize the IPT system's power level with the electric grid frequency. Figs. 3.16a, 3.16b, and 3.16c show the IPT's power transfer levels which are 14, 15, and 16 when the grid frequency becomes 62.87Hz, 63.16Hz, and 64.47Hz respectively. Taking Fig. 3.16c as an example, energy injection pulses in all positive and negative half cycles are high. This again shows that the VIC increases the IPT's power level with increase in frequency. The peak-to-peak value of primary current 11.2A, 11.39A, and 11.65A, for these high power levels (14, 15, and 16) show high power demand in response to the increased grid frequency. The experimental results have shown that the proposed IPT power controller is designed to regulate the power transfer level in

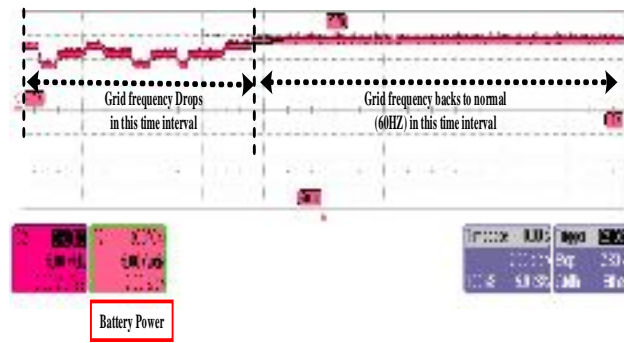


Figure 3.18: Battery power change in response to grid frequency fall using the VIC-based inductive charger.

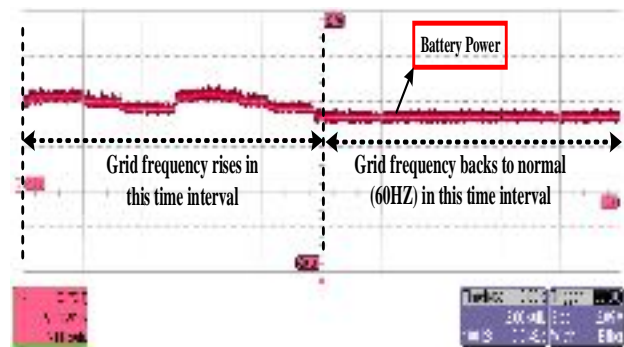


Figure 3.19: Battery power change in response to grid frequency rise using the VIC-based inductive charger.

response to grid frequency change at Grid-to-Vehicle operational mode as shown in Fig. 3.17, as long as the EV battery's SOC lies between 1% or and 100%.

3.6.2 Case1: The grid frequency decreases From $f = 60z$ (Normal) to $f = 58.38z$

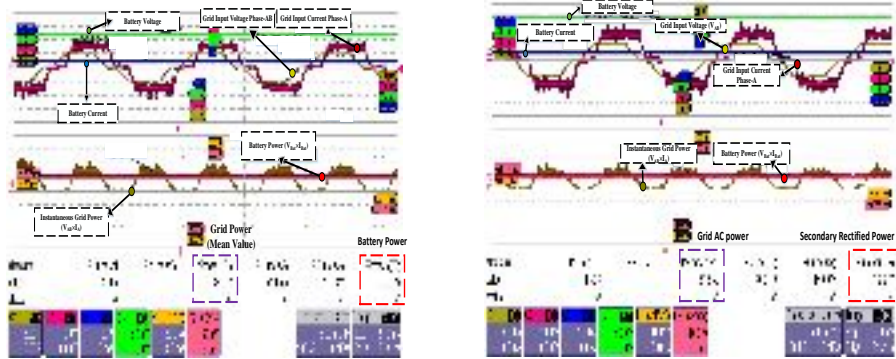
In this scenario, the grid frequency drop is applied to better show the ability of the virtual inertia-based multi-power level controller to regulate the number of power transfer pulses in response to grid frequency fluctuation. As shown in Fig. 3.15a, when the grid frequency is $f = 60Hz$ (normal), the power transfer level is 10. Based on the figure, it means that the IPT multi-power level controller

injects energy in 5-negative/5-positive pulses out of totally 16 half-cycles. When the load increases, the grid frequency gradually decreases, and the IPT virtual inertia-based multi-power level controller accordingly lowers the power transfer level to 9 (4-negative pulses and 5-positive pulses) referring to Fig.3.14d. When the grid frequency further drops to ($f = 58.38\text{Hz}$), the proposed virtual inertia-based controller lowers power transfer level to 8(4-negative pulses and 4-positive pulses) as shown in Fig.3.14c.

All this scenario of grid frequency's drop which is afterward restored back to the normal frequency (60Hz) happens in scale of second in the actual LabVolt System. Given the demonstrated scenario, the battery power in the receiver side presented in the Fig. 3.18 which is decreased under grid frequency fall and then gets back to the normal power level when the grid frequency returns to 60Hz . This scenario further validates the virtual inertia-based IPT's performance in controlling the EV's battery demand in response to grid frequency decrease.

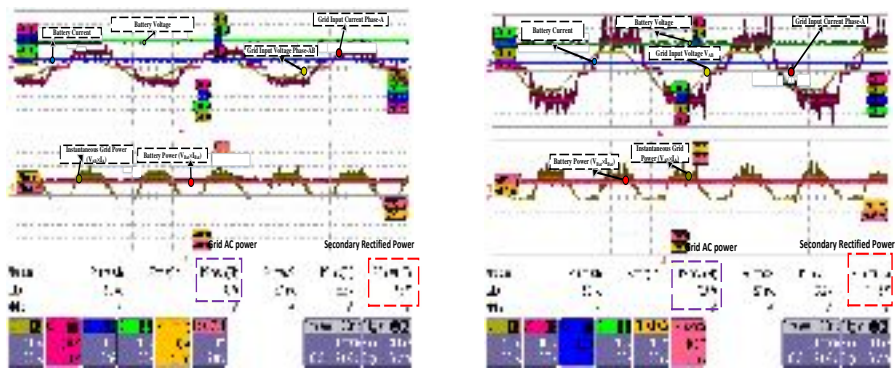
3.6.3 Case2: The grid frequency increases from $f = 60\text{z}(\text{normal})$ to $f = 61.22\text{z}$

In this scenario, the grid frequency rise is applied to show the ability of the proposed virtual inertia-based multi-power level controller in tuning the number of power transfer pulses. As previously shown in Fig. 3.15a, when the grid frequency is $f = 60\text{Hz}$ (normal), the power transfer level is 10. However, when the load decreases, the grid frequency increases, and the proposed virtual inertia-based controller increments the IPT power transfer level to 11. When the grid frequency rises to ($f = 61.22\text{Hz}$) referring to Fig. 3.15b, the proposed virtual inertia-based IPT controller adds one more energy injection pulse, and the power transfer level becomes 12 (see the Fig. 3.15c). All this scenario of grid frequency's rise which is afterward restored back to the normal frequency (60Hz) happens in scale of second in the actual LabVolt System. Given the explained scenario, the battery power in



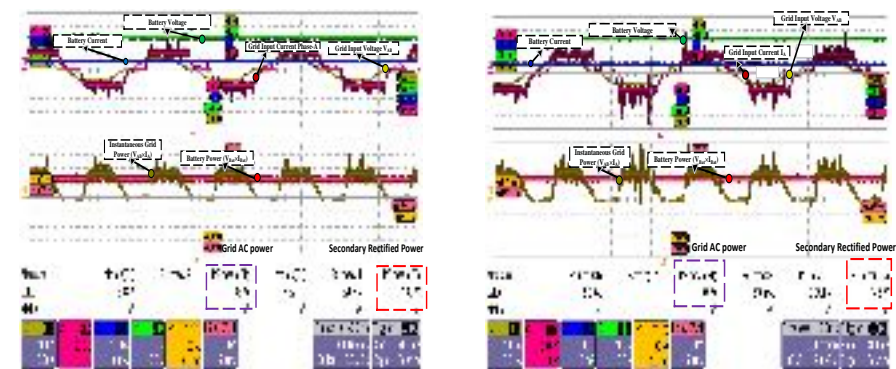
(a)

(b)



(c)

(d)



(e)

(f)

Figure 3.20: Grid-to-Battery efficiency analysis of IPT in different power level (L) is (a)L=10 (b) L=11 (c) L=12 (d) L=13 (e) L=14 (f) L=15

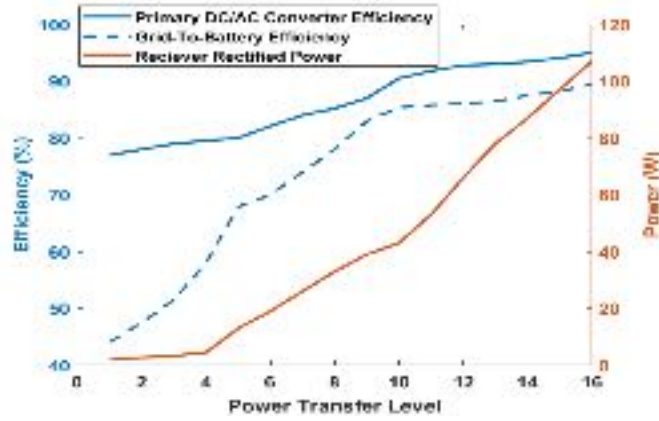


Figure 3.21: Efficiency plots at different power transfer levels

the receiver side presented in the Fig. 3.19 is increased under the grid frequency rise to remove the oscillation. The battery power gets back to the normal level when the grid frequency returns to 60Hz.

3.7 efficiency analysis of the proposed multi-power level

IPT system

As explained, the primary converter is a two-stage AC/DC/AC converter including a full-bridge three-phase AC/DC converter connected to a 60-Hz three-phase supply, and the DC/AC converter controlled with the proposed multi-power level controller. And, in the receiver side, the rectifier converts the induced voltage for battery storage system. In this section, two types of efficiency are measured for the proposed multi-power level IPT system: the Grid-to-Battery efficiency (η_{G2B}) and the primary resonant converter efficiency ($\eta_{Conv.}$). The measurements of battery side and grid-side parameters namely powers, voltages, and currents are presented in Fig. 3.20. In these subplots, the grid's a-b line-line voltage and a-phase current are used for channel1 (C1) and channel2 (C2) in the oscilloscope respectively. And, F1(C1 \times C2) shown in each subplot is a math function which calculates the products of channel1(C1) and channel2 (C2) signals. In other words, F1 calculates $V_{ab} \times I_a$, and, P3(mean(F1)) measures the mean value of F1 as shown

in the purple-dashed box in all the subplots. By multiplying P3 value by $\sqrt{3}$, the three-phase power in the grid side is obtained. Similarly, channel3 (C3) and channel4 (C4) measure the secondary rectified current and voltage respectively. F2 calculates $V_{bat} \times I_{bat}$ and it gives the DC power in the secondary side. Likewise, P6(mean(F2)) measures the mean value of the battery power in the receiver which is shown in the red-dashed box of all plots.

The plot of Grid-to-Battery efficiency (η_{G2B}), the converter efficiency ($\eta_{Conv.}$), and the secondary rectified power (P_{rect}) for all IPT's power levels are shown in Fig. 8.15 based on carried out measurements in different power transfer level. As it can be seen, when the power transfer level increases, the Grid-to-Battery efficiency (η_{G2B}) increases, and reaches up to 89.45% at level=16.

Moreover, it can be concluded that the IPT's total loss increases as the power transfer level decreases due to increase of the number of the IPT's free oscillation states (as depicted in *Mode 5* and *Mode 6* in Figs.3.6). As mentioned, in these modes, the energy injection pulse does not happen, however, the primary resonant current flows through the short-circuited LC which lead to higher conduction loss accordingly.

3.8 Summary

The power-frequency model is used to implement VIC in IPT systems. An IPT multi-power level controller is designed using logic circuit gates which can produce 16-discretized power transfer levels in total. It is shown that VIC implemented via the firmware programming on microcontroller provides the appropriate power transfer level in a real time manner based on the grid frequency fluctuation. The IPT multi-power level controller accordingly regulates the quantum number of energy injection based on the power level set by the VIC. This allows the IPT EV system to appear as a high inertia load to the grid. Experimental results derived in an actual small-scale power grid(LabVolt system) verified that when frequency

either increases or decreases, the proposed VIC sets IPT system either on higher or lower level respectively. The main advantages of the proposed are as follows: 1) Instead of user-defined power reference values, the IPT power reference is selected by VIC; contributing to grid stabilization 2) Simplicity and ease of implementation of multi-power level controller 3) the primary high frequency converter benefits from resonance frequency tracking capability due to the synchronization of switching operations with the resonant current and 4) The proposed VI IPT controller benefits from soft-switching operations (both ZCS and ZVS)

CHAPTER 4

AC-AC MATRIX CONVERTER FOR INDUCTIVE POWER TRANSFER SYSTEMS

Inductive, Electric Vehicle (EV) charging systems have gained much more interest compared to the conventional plugged-in EV chargers due to comfortability, and safety. Regarding high-frequency converters in inductive EV charging system, there are many switching techniques proposed in literature which can be categorized into two major groups including carrier based and non-carrier based methods. Conventional carrier-based Pulse Width Modulation could be employed to modulate magnitude and phase of the converters' output, which result in unnecessary shoot-through states; thereby, increasing the power loss and decreasing the converter's efficiency [84, 85]. On the other hand, non-carrier based PWM methods have become more popular as the switching states are only selected out of limited switching states; resolving the problem of unnecessary switching states. However, there are some issues reported in the literature regarding non-carrier based PWM methods. For instance, the Space Vector Modulation (SVM) requires exact time calculation of each time interval in each sector [86]. Some other researchers have used lookup-based PWM technique using energy injection/regeneration and free-oscillation concept in IPT system [87–89], which can regulate power transfer level in both directions (grid-to-vehicle (G2V) or vehicle-to-grid (V2G)). The major problem with this switching method designed based on energy injection/regeneration and free-oscillation concept is its variable switching frequency. As each power transfer level necessitates different switching frequency (a fraction of IPT operating frequency), therefore, this adversely affects the power transfer capability. In this paper a new lookup-based PWM technique is proposed for AC-AC matrix converter, the conduction period in active state defines the power transfer level in the IPT system. There are many benefits in using the proposed method which include; self-tune capability, low total harmonic dis-

tortion, avoidance of unnecessary switching state, and fixed switching frequency for all possible power transfer level. In one hand, the power transfer rate can be regulated within a fixed switching frequency in a constant operational condition and on the other hand, with dynamic behaviour of IPT system (due to misalignment, or load variation), switching frequency can track resonance frequency as it is synchronized with the resonance current.

4.1 Switching control Logic

In the proposed method, the goal is to regulate the conduction phase (α) within a switching period ($\frac{2\pi}{\omega_r}$) using predetermined switches. As shown in Fig. 4.1, the IPT matrix converter using the proposed switching technique is presented. The power transfer rate in the resonant tank calculated using converter voltage (V_{out}) and the resonant current (I_r) is compared with the IPT set point. The desired conduction phase of the converter (α) is obtained after the power error passed through the PI controller. For the proposed switching technique, conduction phase and resonant frequency (ω_r) are necessary to generate the switching signals. As can be seen from Figs. 4.3 and 4.4, switching logic in G2V mode are explained in two scenarios: when the input ac supply of the converter is in positive half cycle ($V_{ac} > 0$) or in its negative half cycle ($V_{ac} < 0$) respectively.

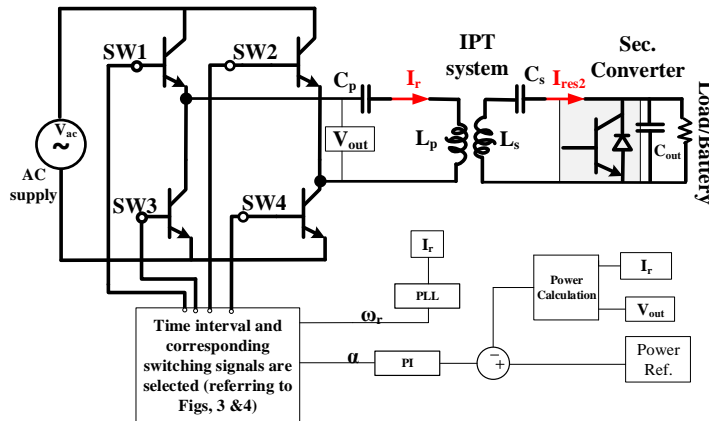


Figure 4.1: Schematic: AC-AC matrix converter for IPT system

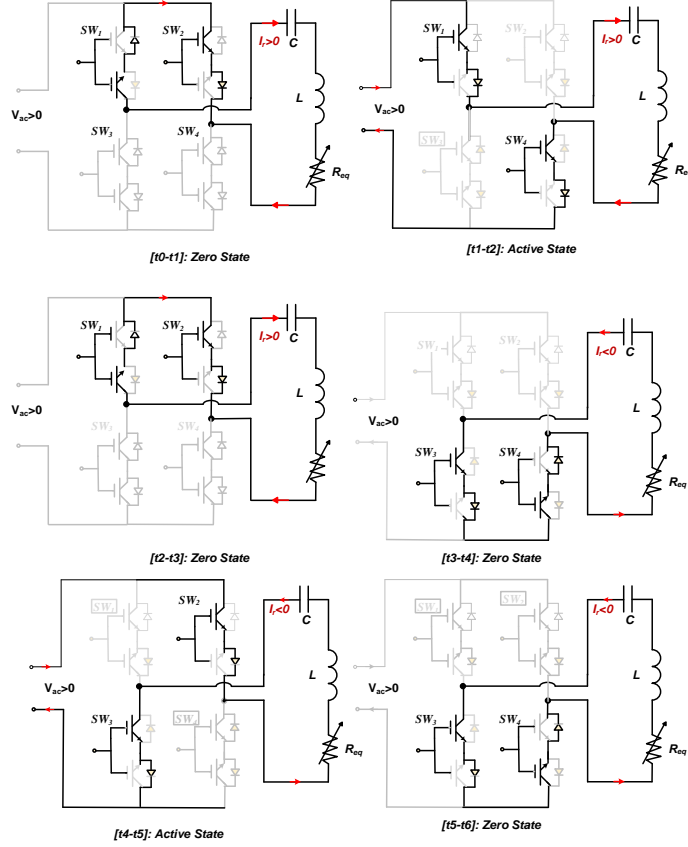


Figure 4.2: IPT's primary resonant current path for six operation modes when ac supply voltage is in positive half cycle (V_{ac})

As can be seen from Fig. 4.3, the first interval $[t_0 - t_1]$ runs as zero state and the output voltage of the converter is zero (referring to subplot g in Fig. 4.3), and SW_1 and SW_2 conduct in this interval, and the corresponding operational power circuit is also presented in Fig. 4.2. In second interval $[t_1 - t_2]$, the converter is in active state; since the resonant current (I_r) is in positive half cycle and the output voltage of the converter should have the same sign $+V_{ac}$ as well (see the subplot g in Fig. 4.3); resulting in forward power transfer (G2V) as the product of voltage and current is positive. That's the reason for selection of SW_1 and SW_4 in this interval; the corresponding operational power circuit of this interval is presented in Fig. 4.2. It should be noted that since the frequency of AC supply is $60Hz$ which is way smaller than the IPT operation frequency $85KHz$, therefore the rate of change in ac supply is relatively low and the ac voltage

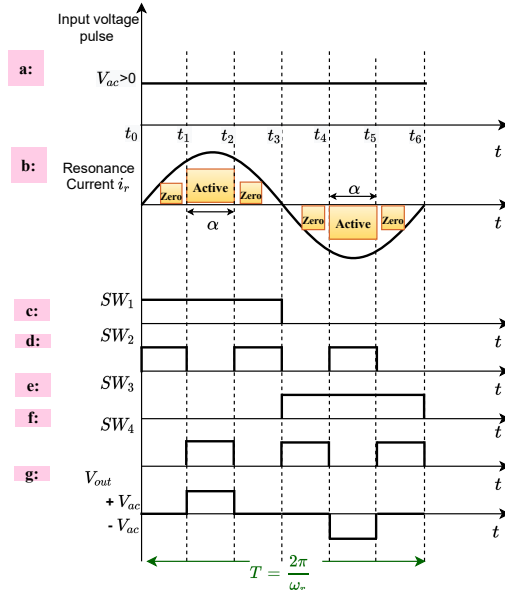


Figure 4.3: when ac supply voltage is positive ($V_{ac} > 0$)

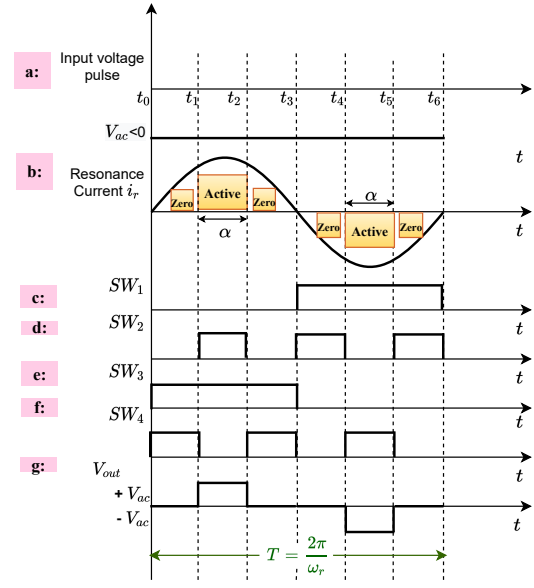


Figure 4.4: when ac supply voltage is negative ($V_{ac} < 0$)

(V_{ac}) can be assumed constant in this interval. In the rest of the time intervals over a resonance frequency, these explanations given for first two intervals can be applied. For the Fig. 4.4, the opposite switching signals repeated, for instance in the second interval, since the input ac voltage is negative ($V_{ac} < 0$), therefore switching signals SW_2 and SW_3 conduct so that positive voltage is produced in the output of the converter; resulting in forward power transfer (G2V).

The reverse power transfer (V2G) can be realized by adding phase shift of 180° to the conduction phase (α); making the resonant current out of phase with respect to converter's voltage. Therefore, the IPT system can have bidirectional capability.

4.1.1 Fundamental Harmonic Analysis of converter's Voltage

Fundamental Harmonic Approximation (FHA) method is used to calculate the converter output voltage. The fundamental component of converter's voltage can be expressed at the resonance frequency (ω_r) as follows:

$$V_1 = \frac{\omega}{2\pi} \int_{t_0}^{t_6} v_{out} \sin(\omega t) dt \quad (4.1)$$

where v_{out} is the output voltage of the primary AC/AC converter, and V_1 is the converter's fundamental harmonic component. t_0 and t_6 are the first and last timing of interval over a resonant frequency. The output voltage of converter in different intervals can be formulated as given below (4.2). By substituting (4.2) in (4.1)

and expanding it, eq.(4.3) can be achieved.

$$v_{out} = \begin{cases} |V_{ac}| & t_1 \leq t < t_2 \\ -|V_{ac}| & t_4 \leq t < t_5 \\ 0 & otherwise \end{cases} \quad (4.2)$$

$$V_1 = \frac{\omega}{2\pi} \left(\int_{t_1}^{t_2} V_{ac} \sin(\omega t) dt + \int_{t_4}^{t_5} -V_{ac} \sin(\omega t) dt \right) \quad (4.3)$$

The timing for either of intervals over a switching frequency is defined in (4.4). Eq.(4.3) can be simplified to eq.(4.5).

$$t_1 = t_0 + \frac{\pi}{2} - \frac{\alpha}{2}; \quad t_2 = t_0 + \frac{\pi}{2} + \frac{\alpha}{2}; \quad t_3 = \pi; \quad t_4 = t_0 + \frac{3\pi}{2} - \frac{\alpha}{2}; \quad t_5 = t_0 + \frac{3\pi}{2} + \frac{\alpha}{2}; \quad t_6 = 2\pi; \quad (4.4)$$

$$V_1 = \frac{2}{\pi} V_{ac} \sin\left(\frac{\alpha}{2}\right) \quad (4.5)$$

Using the relation of voltage in eq.4.5, the primary current can be calculated as shown in eq. 4.6, and power transfer rate of the IPT system can be also calculated as well.

$$I_{pr} = \frac{V_1}{R_{eq}} = \frac{2}{\pi} \frac{V_{ac}}{R_{eq}} \sin\left(\frac{\alpha}{2}\right) \quad (4.6) \quad P = \frac{1}{2} R_{eq} I_{pr}^2 = \frac{V_{ac}^2}{\pi^2 R_{eq}^2} (1 - \cos(\alpha)) \quad (4.7)$$

where R_{eq} (shown in Fig. 4.2) is the equivalent resistance reflected to the primary, because in well-tuned IPT system (at the resonant frequency) the reactive inductance of compensation capacitor and self inductance neutralize each other.

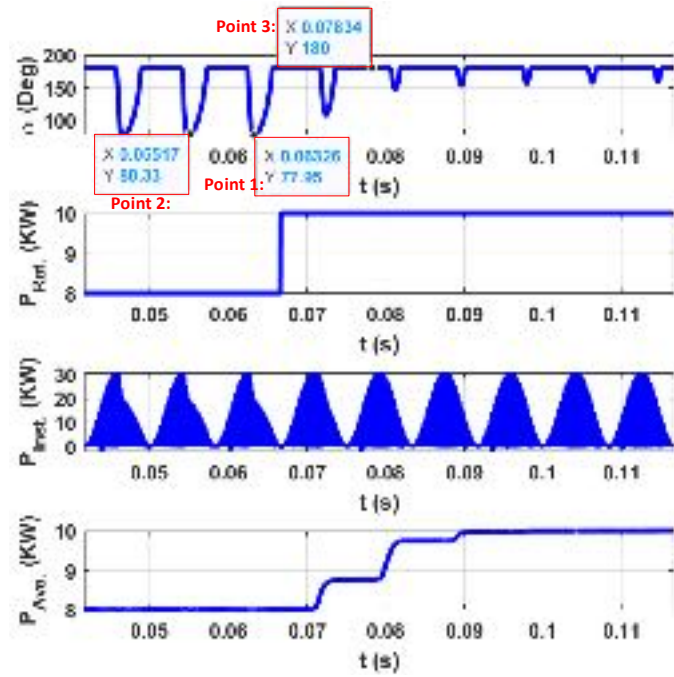


Figure 4.5: a) Converter's conduction phase (α) b) reference power change (P_{ref}) c) IPT's instantaneous Power ($P_{ints.}$) d) Averaged IPT power over 60 Hz time period ($P_{Ave.}$)

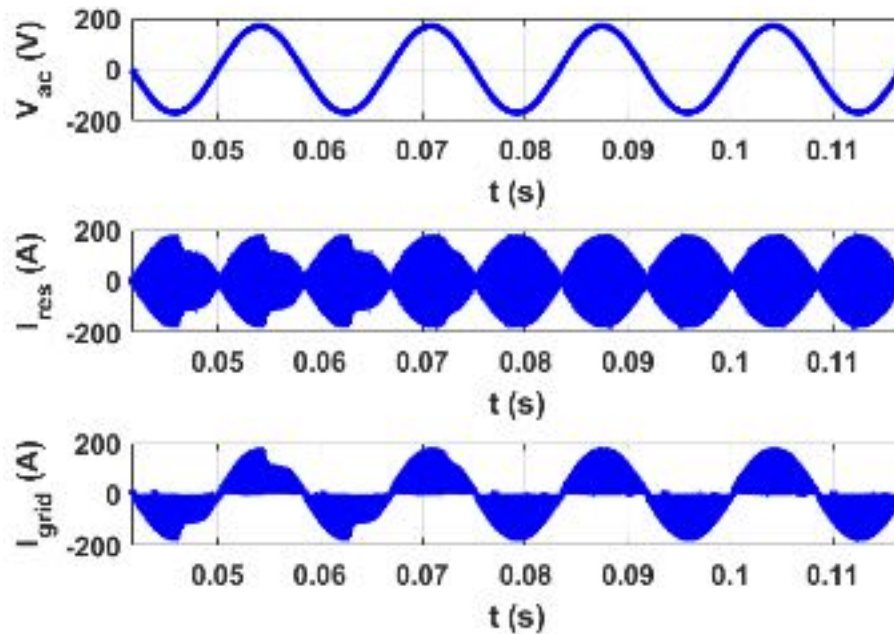


Figure 4.6: a) v_{ac} b) Resonant Current (I_{res}) c) Grid Current (I_{grid})

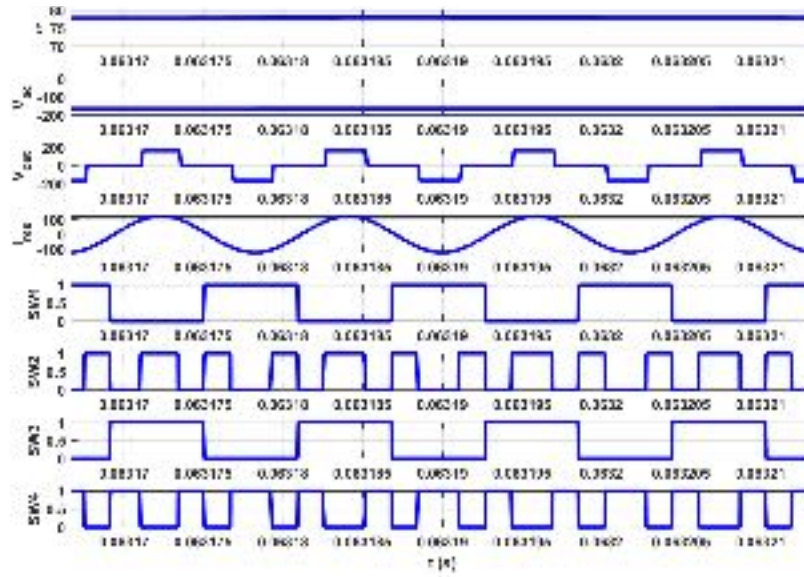


Figure 4.7: plots of I_r , V_{out} , and switching signals for few cycles around the $point_1$ as marked in Fig. 4.5

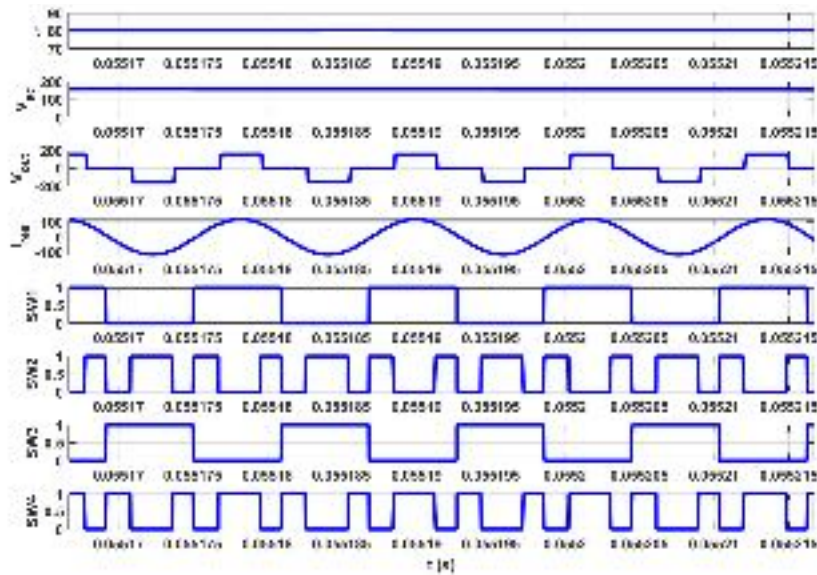


Figure 4.8: plots of I_r , V_{out} , and switching signals for few cycles around the $point_2$ as marked in Fig. 4.5

4.2 Simulation Analysis

In this section, a simulation model of an IPT system and an EV battery connected to the secondary side of IPT is investigated. Table 4.1 shows the specification of the simulated model. The proposed switching method is applied to the primary side of a high-frequency AC-AC matrix converter. The power transfer charging level of the IPT system is increased from $P_{ref} = 8kW$ to $10kW$ at the fourth cycle of main ac supply ($t = 4/60$). As it can be seen from Fig. 4.5, when IPT power transfer rate is $8KW$, the conduction phase(α) changes in opposite manner with respect to main supply voltage ($|V_{ac}|$). On the other hand, at $10KW$ the conduction phase(α) is almost 180° ;not changing too much. The fourth plot in Fig. 4.5 shows that the averaged IPT power tracks the set points. As seen from the figure, as the power set point changes, the averaged IPT power increases, settles and again increases. However, this is due to the fact that the power calculation is done over the $\frac{1}{60Hz}$ period. The instantaneous power shown in the third plot of Fig. 4.5 clearly shows the dynamic change of IPT power in response to the change in the power reference. In Fig. 4.6, the plots of ac voltage, resonant current, along with grid current are shown within seven main frequency cycles ($60Hz$). Since the detailed view of resonant currents and switching signals are difficult in this time scale, these plots around three different points marked as *point1*, *point2*, and *point3* (see Fig. 4.5) are shown in scale of resonant frequency in Figs.4.7 , 4.8, and 4.9 respectively. As it is evident, the switching signals in Figs.4.7 and 4.8 conform with the switching patterns illustrated in Figs.4.3 and 4.4 which are explained earlier for positive/negative grid ac voltage. Moreover, $\alpha = 180^\circ$ in Fig. 4.9 shows complete conduction in either of positive and negative half cycle of resonant current which happens to increase the IPT power rate.

Table 4.1: Technical specification of simulation model

Parameter	Value
Main ac Supply (V_{ac})	120 v
Primary and Secondary Compensation capacitors (C_p, C_s)	38 nF
Mutual Inductance (L_M)	20.52 μ H
Primary/Secondary self inductance (L_p, L_s)	92.31 μ H
Input AC frequency (f)	60 Hz
IPT designed resonance frequency (f_r)	85 kHz

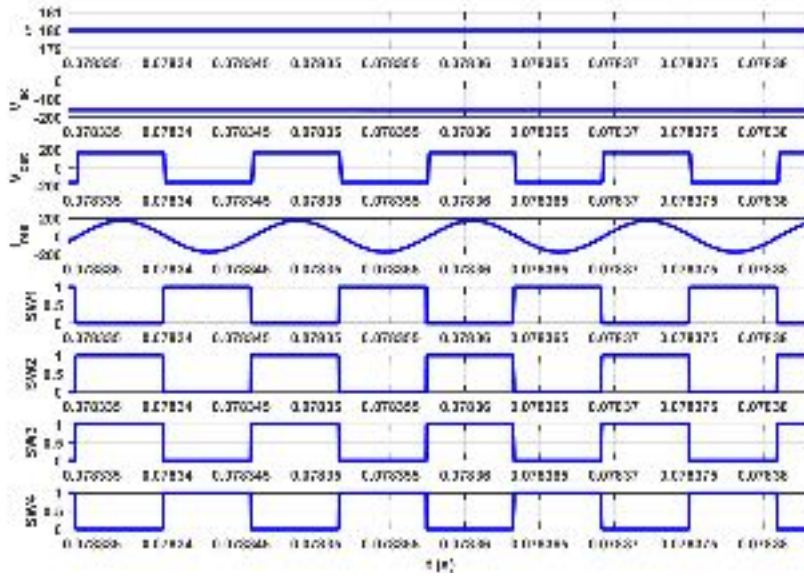


Figure 4.9: plots of I_r , V_{out} , and switching signals for few cycles around the $point_3$ as marked in Fig. 4.5

4.3 Experimental Validation for the multi-power level controller with Zero states

In order to validate the effectiveness of the proposed multi power level control, a Dynamic IPT (D-IPT) setup is implemented. The switching logic is programmed on an Intel® Cyclone V FPGA board. The dynamic IPT setup comprises of 5 bipolar transmitting couplers and a movable receiving coupler. The technical specifications of the D-IPT is as presented in Table.8.2.

The proposed switching logic is programmed in cyclone v 5csema4u23c6n and tested in the same setup described earlier. The experimental result for switching

signals, resonant current and voltage for two different cases when input AC voltage are positive and negative is as shown in Figs.4.10 and 4.11.

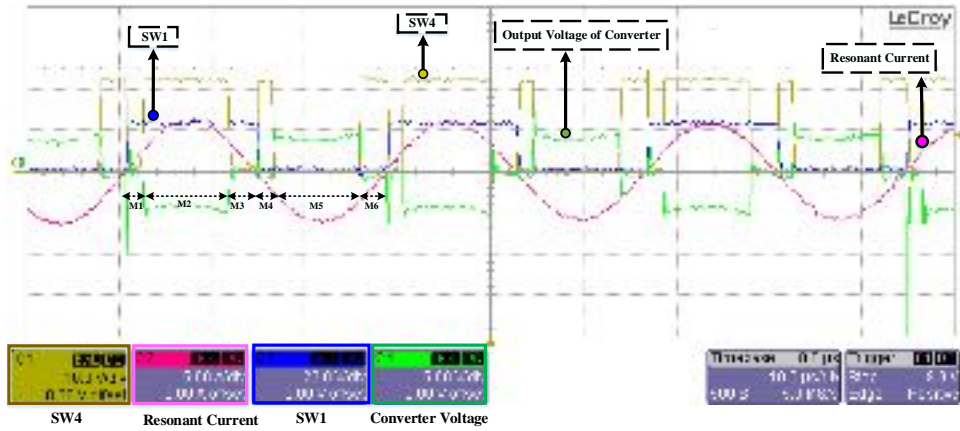


Figure 4.10: Experimental result for switching signals (SW1 and SW4), resonant current and converter output voltage when input AC voltage are positive

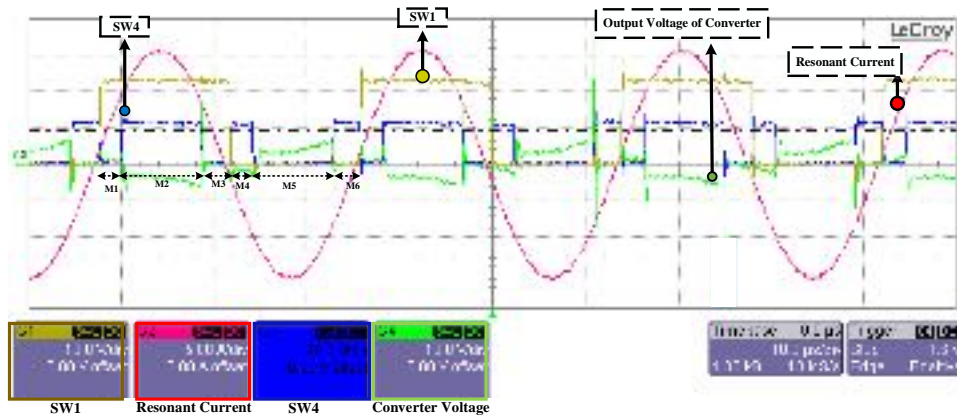


Figure 4.11: Experimental result for switching signals(SW2 and SW3), resonant current and converter output voltage when input AC voltage are positive

Table 4.2: Technical specification of IPT system Set up

Parameter	Value
Gap distance	200 mm
transmitter pad diameter	352 mm
Primary and Secondary Compensation capacitors (C_p, C_s)	82 nF
Primary/Secondary self inductance (L_p, L_s)	38.3 μ H
AC Input voltage (V_{ac})	120 V
Input AC frequency (f_{ac})	60 Hz
IPT designed resonance frequency (f_r)	90 kHz

Due to limited voltage probes of oscilloscope, the experimental results showing the states of SW1 and SW4 during modes $M1 \dots M6$ and SW2 and SW3 during modes $M1 \dots M6$ are as presented in figs. 4.10 and 4.11 respectively. As can be seen from Fig.4.10 and Fig.4.11, in positive half cycle of current and time interval $M1$, switches SW1 and SW3 start conducting. The ON state of SW3 and SW1 generates a zero voltage state. The zero voltage (in mode $M1$) (green plot) as well as a path for flow of resonant current in positive half cycle is shown in both figs. 4.10 and 4.11 .

Next, during $M2$ time interval, switches SW2 and SW3 turn off, while switches SW4 and SW1 turn ON. This produces a positive output voltage. In the next mode $M3$, switches SW2 and SW4 turns off, while SW1 and SW3 are turned ON switches which creates a zero output voltage, additionally forming a path for resonant current in positive half cycle.

During the $M4$ time interval, the resonant current is in negative half cycle. Switches SW2 and SW4 turn on, which create zero voltage state and establishes a path for flow of negative resonant current as seen in figs. 4.10 and 4.11 . In the next time interval $M5$, switches SW1 and SW4 turns off while switches SW2 and SW3 turns on. This produces a negative output voltage which is in phase with the resonant current in order to transfer power toward EV. Finally, in the last mode $M6$, switches SW1 and SW3 turns off while switches SW2 and SW4 turns on. The ON switches SW2 and SW4 causes a zero voltage state as well as circuit path for flow of resonant current. As it can be seen, energy injection operational modes, undesirable negative power transfer did not occur, which verifies the effectiveness of the proposed control and switching technique.

4.4 Summary

A new switching technique for single stage AC-AC matrix converter is proposed. Unlike conventional carrier-based PWM techniques, it employs predetermined

switching vector to eliminate unnecessary switching such as shoot-through, and reduce THD as well as conduction loss. The proposed method improves the performance of IPT system in power regulation by adjusting the conduction angle in active state. This method modulates the power transfer level over a constant switching frequency when there is no load variation or misalignment, furthermore, it can always provide resonance condition in IPT system as the switching frequency is synchronized with resonant current. A simulation study carried out clearly showed the self-tuned performance of the proposed converter in tracking the IPT power reference.

CHAPTER 5
AN ACCURATE ONLINE PARAMETER ESTIMATION
TECHNIQUE FOR INDUCTIVE ELECTRIC VEHICLE
CHARGING SYSTEMS

5.1 Introduction

Inductive Power Transfer (IPT) is a promising technology can be used in wide range of applications. Specifically, IPT enables contactless charging which brings more convenience to the use of electric vehicles (EVs). Unlike conventional wired charging systems, inductive charging systems should be able to adapt to different charging conditions. Although the technical specifications of inductive EV chargers should comply with well established standards [37], EVs may still have different requirements e.g. in terms of ground clearance and traction battery voltage. More importantly, during the charging process, EVs can have changes in their ground clearance due to loading/unloading. Therefore, the major challenge in IPT systems is to maintain the maximum power transfer efficiency in any operating conditions. The maximum power transfer operating point of an inductive charging system is determined by the primary power electronics controller based on several key parameters including primary and secondary self-inductances, air-gap and traction battery voltage, and charging requirements. For improving the energy transfer performance under wide load range and frequent misalignment, a countless of control techniques as well as various topologies have been proposed which result in so many remarkable achievements in IPT development and even commercialization. Multi-powerlevel IPT controller is introduced in [90, 91] which enable self-tune under load change throughout the charge process. In [92], variable frequency phase shift technique is applied in LCC-Series IPT system which significantly reduce loss and guarantee soft switching (ZCS and ZVS). However, these variable frequency techniques differ the IPT system operational frequency from

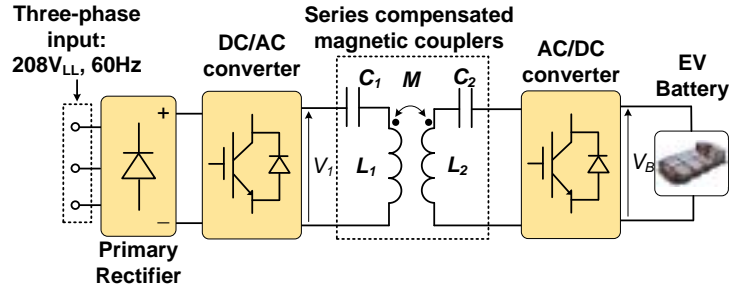


Figure 5.1: A typical Series-Series IPT system

the resonant frequency which makes IPT operates off its desired design frequency. To resolve this issue, impedance adjustment scheme are getting popularity [93–95]. Study [96] has proposed a continuously adjustable capacitor for Multiple-Pickup IPT system which can match impedance network under variable frequency. In [97], variable inductive impedance matching is introduced using multi-loop control technique; this adjustable inductive scheme is applied to adjust both primary and secondary impedance.

Even with so many control techniques for soft switching, impedance networking matching schemes, power electronics typologies ([98]), and coupler configurations([99]) are introduced for efficiency enhancement, still a big issue is the self-tune capability of IPT as it is missing in the literature. It means the adaptive IPT controller should be considered which identify the parameter values of pickup side and regulate the charging level accordingly. To do so, online parameter estimation in IPT systems can be employed to continuously adapt the IPT system to the target system variations and track the maximum power transfer efficiency. Therefore, online parameter estimation is essential and can significantly contribute to the performance enhancement of IPT systems. Also, parameter estimation methods that do not require information from the receiver side are of more interest as the need for communication between the transmitter and receiver is eliminated. Parameter estimation methods for IPT systems have been studied in [100–103]. These methods are primarily based on impedance analysis. In [100], a magnetic coupling coefficient estimation based on impedance measurement is proposed. In

study [104], the coupling coefficient estimation method WPT system is proposed through impedance analysis which only uses primary side information. The estimation method can be operational if only if a decoupled circuit applied to the pickup side, However, simultaneous estimation of magnetic coupling and secondary load is not reported in the literature. In this chapter, an online parameter estimation method that determines both magnetic coupling factor and battery charging current simultaneously in real-time is presented. The proposed method is developed based on the derivation of analytical formulations for magnetic coupling factor secondary battery charging current and voltage as functions of primary current, primary compensation capacitor voltage and electrical specifications of the system. Therefore, the developed method only requires information from the primary side. The proposed method is developed based on the assumption that the IPT system is driven exactly at the resonance frequency. The proposed method is simulated MATLAB/Simulink and is experimentally implemented in a prototype. The results confirm the effectiveness and accuracy of the proposed method.

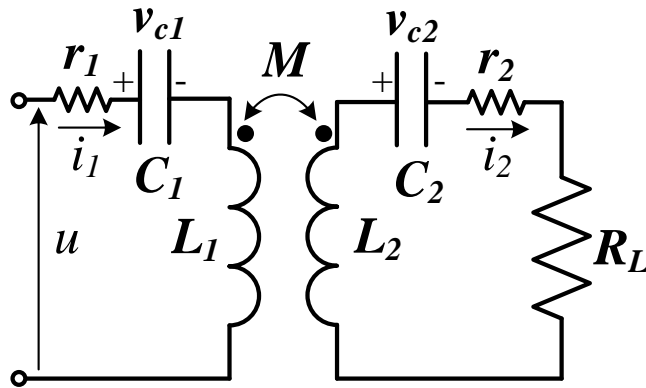


Figure 5.2: Series-compensated inductive charging system: equivalent circuit and corresponding variables.

5.1.1 Magnetic Coupling Coefficient Estimation

The equivalent circuit of a in series compensated inductive battery charging system (Fig. 5.1) is shown in Fig. 5.2 where, u and i_1 are the voltage and current outputs of the primary converter receptively, i_2 is the secondary current, r_1 and r_2 are the equivalent resistances of the primary and secondary sides respectively. r_1 and r_2 incorporate the equivalent series resistances of the compensation capacitors, coils, magnetic core and shielding plates. It can be shown that the secondary RMS current I_2 then can be calculated as,

$$I_2 = \frac{\omega M I_1 - \frac{2\sqrt{2}}{\pi} V_B}{r_2} \quad (5.1)$$

where V_B is the traction battery voltage. In a series compensated IPT system which operates at the resonance frequency ω , the equivalent load resistance reflected to the primary can be expressed as [11],

$$R_{eq} = \frac{\omega^2 M^2}{r_2 + R_B} \quad (5.2)$$

where $R_B = \frac{2\sqrt{2}}{\pi} \frac{V_B}{I_B}$. Therefore, using (5.1), (5.2) can be rewritten as,

$$R_{eq} = \frac{\omega M (\pi \omega M I_1 - 2\sqrt{2} V_B)}{\pi r_2 I_1} \quad (5.3)$$

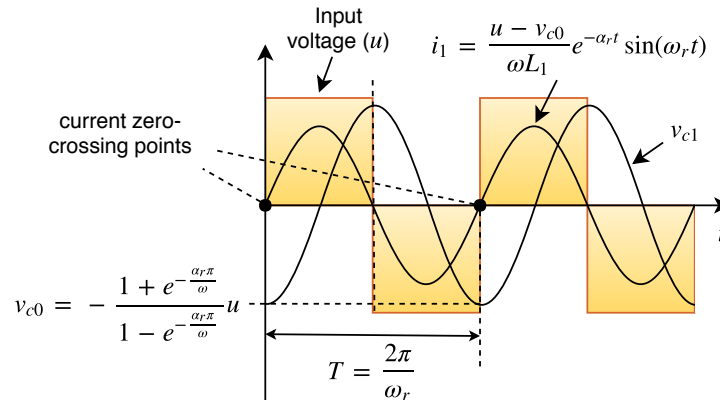


Figure 5.3: A conceptual plot of the resonant current, capacitor voltage and corresponding analytical formulations.

By applying KVL to the primary, fundamental harmonic component of the input voltage applied to the primary can be written as $V_1 = (r_1 + R_{eq})I_1$. Thereby, using (5.3), the primary and secondary currents I_1 can be derived as,

$$I_1 = \frac{\pi r_2 V_1 + 2\sqrt{2}\omega M V_B}{\pi(r_1 r_2 + \omega^2 M^2)} \quad I_2 = \frac{\pi\omega M V_1 - 2\sqrt{2}r_1 V_B}{\pi(r_1 r_2 + \omega^2 M^2)} \quad (5.4)$$

By solving (5.4) for M and using the definition $M = k\sqrt{L_1 L_2}$ the coupling factor k can be derived as,

$$k = \frac{\sqrt{2} V_B + \sqrt{2V_B^2 + \pi^2 r_2 I_1 (V_1 - r_1 I_1)}}{\pi\omega\sqrt{L_1 L_2} I_1} \quad (5.5)$$

Using (5.4), the coupling factor k can be estimated based on primary RMS current measurement (I_1). Assuming r_1 and r_2 are negligible, the coupling factor is approximated as (5.6):

$$k = \frac{2\sqrt{2} V_B}{\pi\omega\sqrt{L_1 L_2} I_1}. \quad (5.6)$$

5.1.2 Battery Charging Current Estimation

The battery charging current (I_B) can be calculated by using (5.4), (5.5) and the fact that in a rectifier the battery charging current $I_B = \frac{2\sqrt{2}}{\pi}I_2$ can be estimated as,

$$I_B = \frac{2\sqrt{2}\pi\omega k\sqrt{L_1 L_2} V_1 - 8r_1 V_B}{\pi^2(r_1 r_2 + \omega^2 k^2 L_1 L_2)} \quad (5.7)$$

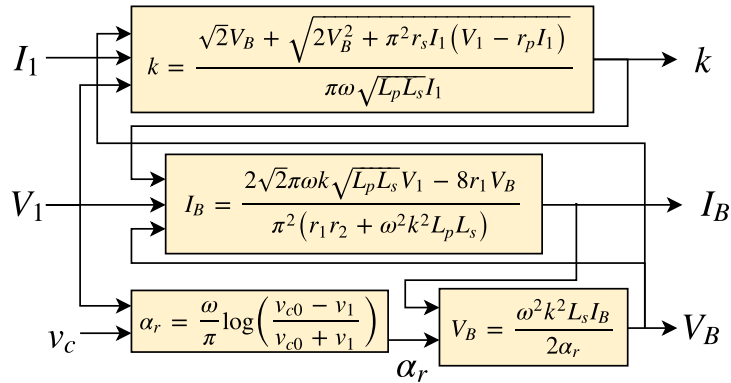
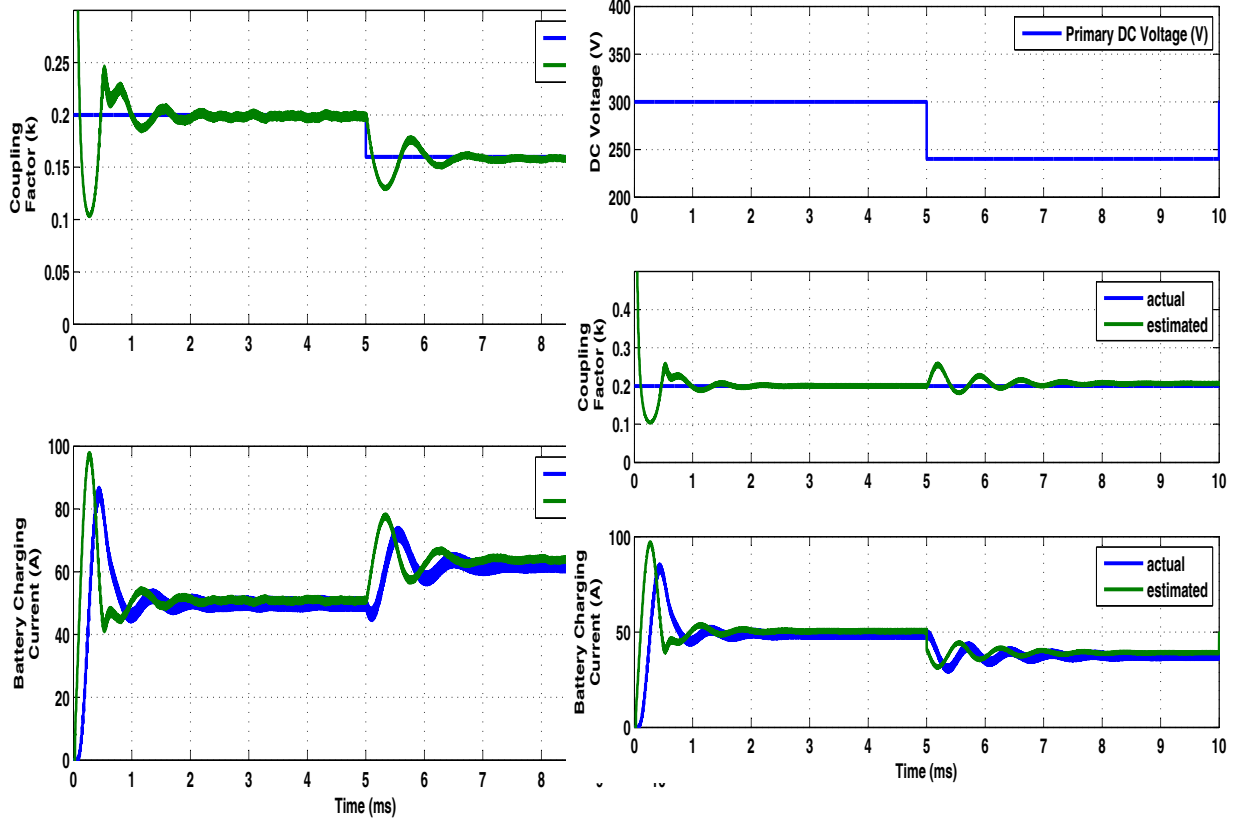


Figure 5.4: The flowchart of the developed parameter estimation method based analytical formulations.



(a) 20% sudden reduction in coupling factor at $t = 5ms$ (b) 17% sudden reduction in primary DC voltage at $t = 5ms$.

Figure 5.5: The simulation results of the developed parameter estimation method

Also, assuming $r_1 = 0$, (5.7) can be further simplified as :

$$I_B = \frac{2\sqrt{2}V_1}{\pi\omega k\sqrt{L_1L_2}} \quad (5.8)$$

5.1.3 Battery Voltage Estimation

In IPT systems, the primary resonant current (i_1) referring to [55] during any half-cycle can be written as (5.9):

$$i_1 = \frac{u - v_{c0}}{\omega L_1} e^{-\alpha_r t} \sin(\omega_r t) \quad (5.9)$$

where v_{c0} is the primary capacitor voltage at the resonant current zero-crossings, α_r is the damping constant and, ω_r is the damped resonance frequency of the IPT

system (see Fig. 5.3). In steady-state, v_{c0} can be calculated according to [55],

$$v_{c0} = -\frac{1 + e^{-\frac{\alpha_r \pi}{\omega}}}{1 - e^{-\frac{\alpha_r \pi}{\omega}}} u \quad (5.10)$$

By solving (5.10) for α_r , the following is derived,

$$\alpha_r = \frac{\omega}{\pi} \log \left(\frac{v_{c0} - u}{v_{c0} + u} \right) \quad (5.11)$$

Also, the following set of equations can be derived for α_r , reflected load resistance to the primary R_{eq} , equivalent AC charging load resistance R_s and equivalent battery resistance R_B :

$$\alpha_r = \frac{R_{eq}}{2L_1} \quad R_{eq} = \frac{\omega^2 M^2}{R_s} \quad R_s = \frac{8}{\pi^2} R_B \quad R_B = \frac{V_B}{I_B} \quad (5.12)$$

Using (5.12), the battery voltage can be estimated as,

$$V_B = \frac{\pi^2 \omega^2 k^2 L_2 I_B}{16 \alpha_r} \quad (5.13)$$

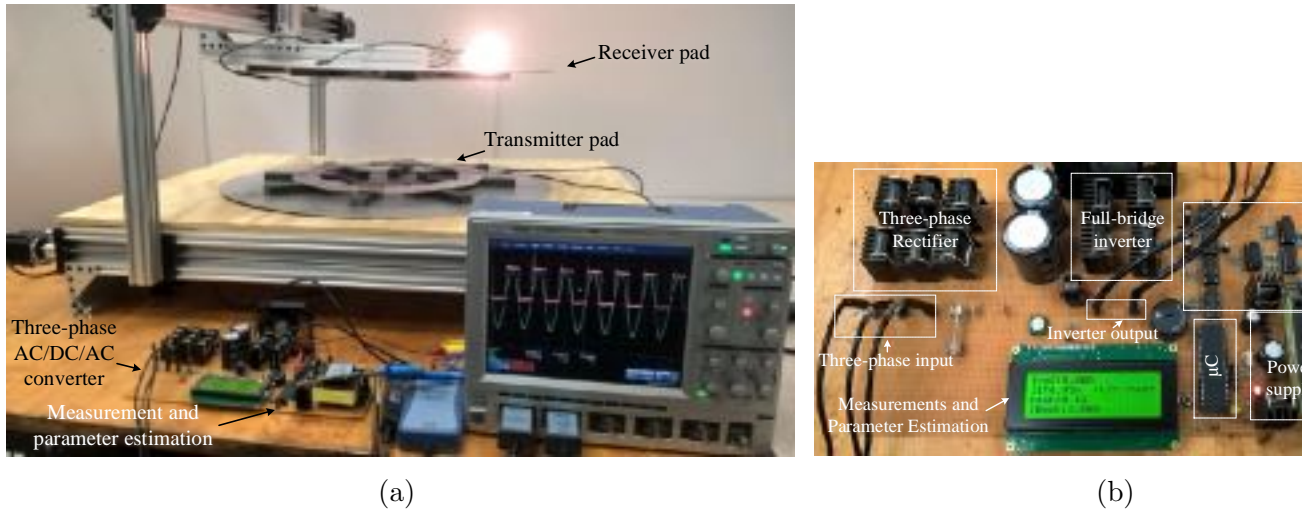


Figure 5.6: The experimental setup of the inductive charging system prototype with online parameter estimation functionality.

In Fig. 5.4, the overall flowchart of the developed parameter estimation method based analytical formulations. As shown, only primary side measurements (I_1 , V_2 , and v_{c0}) are used to estimate the magnetic coupling (k) and the secondary battery charging current and voltage (I_B and V_B). According to Fig. 5.4, there

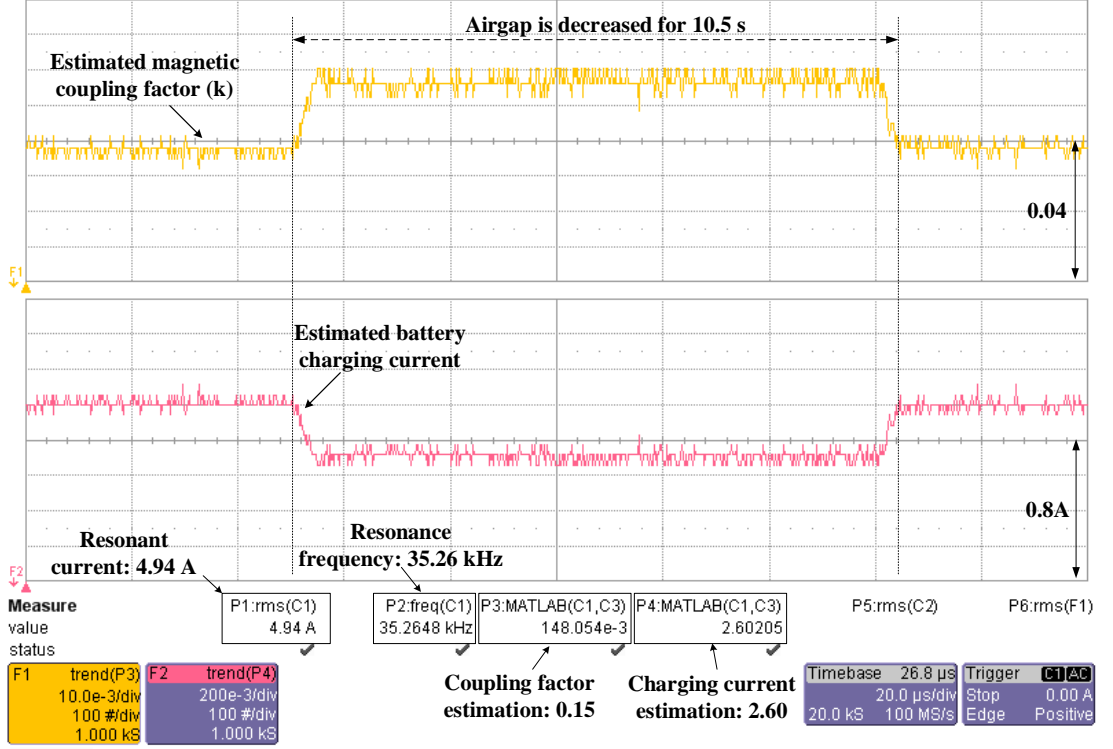


Figure 5.7: The estimated coupling factor and battery charging current while the airgap is reduced for 10.5 seconds.

is an algebraic loop in the flow of the parameter estimation method. This issue is addressed by assigning the setting the initial value of V_B as the nominal traction battery voltage.

5.2 Simulation Analysis

In order to demonstrate the effectiveness and accuracy of the proposed parameter estimation method MATLAB/Simulink simulations are carried out in two scenarios, the results of which are presented in Fig. 5.5. The simulation model is composed of a WPT4 22kW battery charger [105]. In the first scenario, the coupling factor is suddenly reduced from 0.2 to 0.16 at $t = 5ms$ (Fig. 5.5(a)). One assumption in this simulation study is the self-tuned ability of the IPT power controller. As a result of the step change in coupling factor, the battery charging current in the secondary side is increased to compensate the reduced coupling fac-

tor. As can be seen from 5.5(a)), the estimated battery current also tracks closely the actual simulation counterpart.

In the second scenario, the DC voltage level at the primary side is reduced from 300V to 250V at $t = 5ms$ (Fig. 5.5(b)). These results show that the proposed algebraic estimation method can accurately track the actual magnetic coupling factor and the battery charging current with high accuracy in real-time.

5.3 Experimental Analysis

The proposed method is experimentally implemented experimentally. The experimental setup which is shown in Fig. 5.6 is comprised of primary AC/DC/AC converter connected to a variable three-phase AC input, the secondary AC/DC converter connected to a battery, and primary and secondary magnetic structures with an airgap of 250mm. To demonstrate the effectiveness of the proposed method, an experiment is performed by reducing the airgap between the transmitter and receiver for about 10.5 seconds and then going back to the original condition. The proposed parameter estimation is programmed in the LeCroy scope and the result is presented in Fig. 5.7. The estimated parameter including coupling factor, secondary side battery current as presented in the flowchart 5.4 are calculated using MATLAB Mfile based on the primary side measurements. This figure shows that using the developed method, the parameters can be effectively estimated in real-time.

5.4 Conclusions

An online parameter estimation method that can simultaneously determine the magnetic coupling coefficient and the load at the secondary has been introduced. The proposed method is developed based on the analytical formulations for the magnetic coupling, battery charging current and battery voltage that are expressed

in terms of primary side measurements and system specifications. The proposed method is simulated and experimentally validated and the results are presented. The simulation and experimental results verify that the proposed method can accurately estimate the magnetic coupling factor, secondary battery charging current and voltage in inductive charging systems simultaneously in real-time. The developed method can find immediate applications for the development of adaptive controllers for static and dynamic inductive charging systems.

CHAPTER 6

**COMPARISON ANALYSIS OF BIPOLAR AND DOUBLE
D-SHAPE CONFIGURATIONS IN INDUCTIVE POWER
TRANSFER ELECTRIC VEHICLE CHARGERS**

6.1 Introduction

Recently, the conventional plugged-in EV chargers have been rapidly transitioned into wireless chargers using IPT systems as the effort; contributing to adoption of the smart grid infrastructures. Wireless charger can establish both Grid2vehicle and Vehicle2Grid connections [106, 107] which can serve smart grid by alleviating overgeneration of distributed energy resources, and shaving load peak via EV's energy storage availability.

Generally, inductive EV charging systems (refer to the conceptual schematic shown in Fig.6.1) can be realized in two major categories: stationary and dynamic ways. In stationary IPT systems, both vehicle's assembly power pad and ground assembly's power pad are well aligned as well as fixed; however, in the dynamic IPT system [108], EV can get charged while moving. Most of researches in stationary IPT systems are concentrated on power controller improvement, on the other hand, a few researches are focused on the design optimization of power pad geometry and its configuration. The idea of stationary IPT systems with an intermediary coil is implemented in [109–111] to achieve improved system efficiency, better misalignment, zero phase angle, and constant current/constant voltage battery characteristic. Authors of [112] categorized power pad configurations into distributed and lumped models, the former, due to elongated coupler is appropriate in dynamic applications where continuous power delivery is essential, the latter is utilized when pickup such as EV is to be placed in a specific position. Because of the large gap between primary and secondary pad due to EV's big

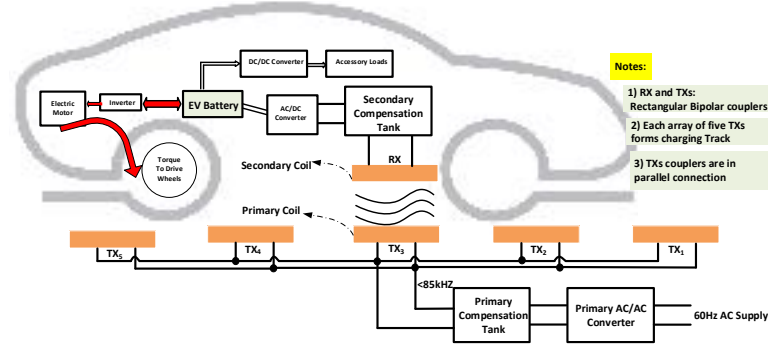


Figure 6.1: The conceptual schematic of IPT roadway-powered track for dynamic EV charging system

ground clearance (the range of $150\text{-}250\text{mm}$), the coupling factor of the lumped couplers is significantly high.

The circular pads are not suitable for dynamic EV charging applications which frequently experience misalignment [113]. This is due to the fact that the circular power pads geometry is proportional to air gap size with ratio of $4 : 1$; for example, with 50mm increase in gap, 200mm increase of diameter is needed to have a fixed power transfer [113, 114]. To address this issue, Double D-shape coils (DD) is proposed which can combine single-sided flux advantage of circular pad with magnetically series benefits of flux pipe design [112]. Pries et al developed a three-phase couplers which improves power density thanks to rotating magnetic field. However, in poly-phase multi layer power pads, unbalanced inductance in different phases leads to difficulty in design of tuning capacitors[115]. Long-track-loop power pads[5, 116] can provide continuous wireless power delivery. However, this type of IPT systems suffer from low efficiency, low magnetic coupling factor, and high self-inductance, making driving the primary coil difficult. Additionally, in long-track IPT systems delivering power to multiple pickups, full charge state of only one of them reflected as the high impedance in the primary track can disrupt the total charging process [117, 118].

In this paper, bipolar power pads (BPP) are proposed as a very efficient coupler for dynamic wireless EV charger with improved power transfer ability, low power loss,

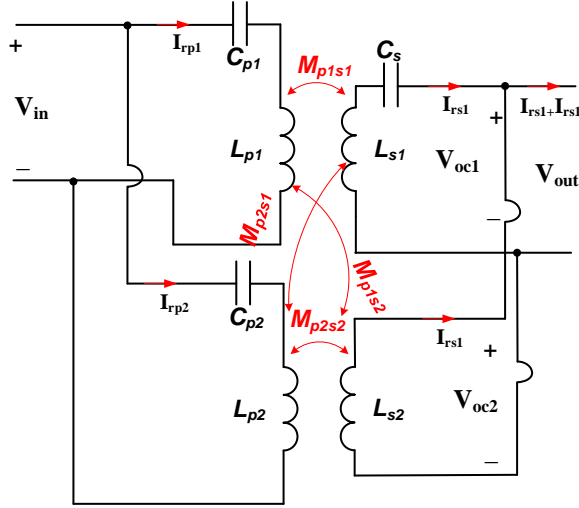


Figure 6.2: IPT systems consists of two primary couplers (TX1, and TX2) and two secondary couplers (RX1, and RX2)

high power density, low electromagnetic emission, and specially with high tolerance to horizontal misalignment. To verify the superiority of BPP, its performance is compared with DD which has been introduced as the one of the well-known couplers in IPT EV chargers. To do so, a 3D-FEA analysis is done in the ANSYS MAXWELL to compare their power transfer capability, tolerance performance and electromagnetic field emission.

6.2 Power transfer calculation

IPT typologies comprised of double couplers such as BPP and DD ([119]) have gained more interest due to their high efficiency for roadway powered applications. The circuit schematic of this type of couplers with Parallel-Parallel compensation topology in both primary and secondary sides is presented as shown in Fig.6.2. To calculate the output power in the secondary side, Fundamental Harmonic Analysis(FHA) (as the widely accepted method) is adopted in analyzing circuit (as shown in Fig.6.3) around the fundamental resonant frequency.

According to [120], the output power of an IPT system can be expressed as

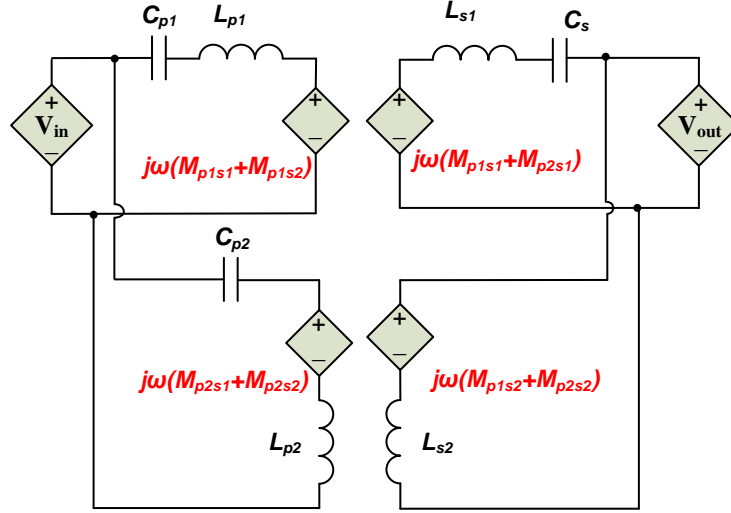


Figure 6.3: Simplified IPT circuit for double couplers configuration using FHA method

follows :

$$P_{out} = \omega_r \frac{M^2}{L_2} I_{rp}^2 Q_2. \quad (6.1)$$

where, M , L_2 , I_{rp} , and Q_2 are mutual inductance, secondary self-inductance, primary resonant current, and secondary loaded quality factor, respectively. Accordingly, the uncompensated power can be derived as expressed in (6.2):

$$P_{su} = V_{OC} I_{SC} = \omega_r \frac{M^2 I_{rp}^2}{L_2}. \quad (6.2)$$

Likewise, the output power of double-type couplers (either DD or BPP configurations) can be calculated by summing the power of RX1 and RX2 using the

following equations.

$$\left\{ \begin{array}{l} V_{OC1} = \omega_r(M_{s1p1} + M_{s1p2})I_{rp1} \\ V_{OC2} = \omega_r(M_{s2p1} + M_{s2p2})I_{rp2} \\ I_{sc1} = \frac{V_{OC1}}{\omega_r L_{s1}} = \frac{(M_{s1p1} + M_{s1p2})I_{rp1}}{L_{s1}} \\ I_{sc2} = \frac{V_{OC2}}{\omega_r L_{s2}} = \frac{(M_{s2p1} + M_{s2p2})I_{rp2}}{L_{s2}} \\ P_{su} = P_{RX1} + P_{RX2} = V_{OC1}I_{SC1} + V_{OC2}I_{SC2} \\ P_{su} = \omega_r \left(\frac{(M_{s1p1} + M_{s1p2})^2 I_{rp1}^2}{L_{s1}} + \frac{(M_{s2p1} + M_{s2p2})^2 I_{rp2}^2}{L_{s2}} \right) \end{array} \right. \quad (6.3)$$

Equation.(6.3) is used as the power calculation of DD and BPP in order to accurately compare these two couplers. Also, the electromagnetic emission compatibility (EMC) and electromagnetic characteristic comparison of these power pads are presented in the next sections.

6.3 Comparison of performance of BPP and DD couplers

In this section, a 3-D Finite Element Analysis (FEA) models of DD and BPP are built using ANSYS MAXWELL as shown in Fig.6.4a and 6.4b respectively. For fair comparison, the geometry of the couplers is considered close.

6.3.1 EMC comparison of DD and BPP couplers

The maximum allowable exposure of EMF for public safety is $.5\mu T$ according to ICNIRP guidelines [121]. As it can be seen from Fig.6.5a, when the pri-

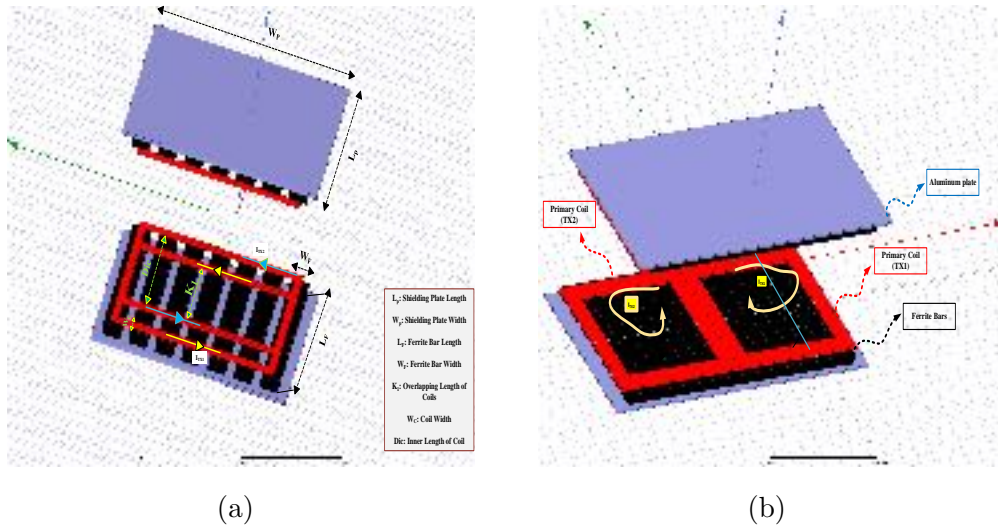


Figure 6.4: 3D-FEA model of 2 (a) DD (b) BPP Coupler

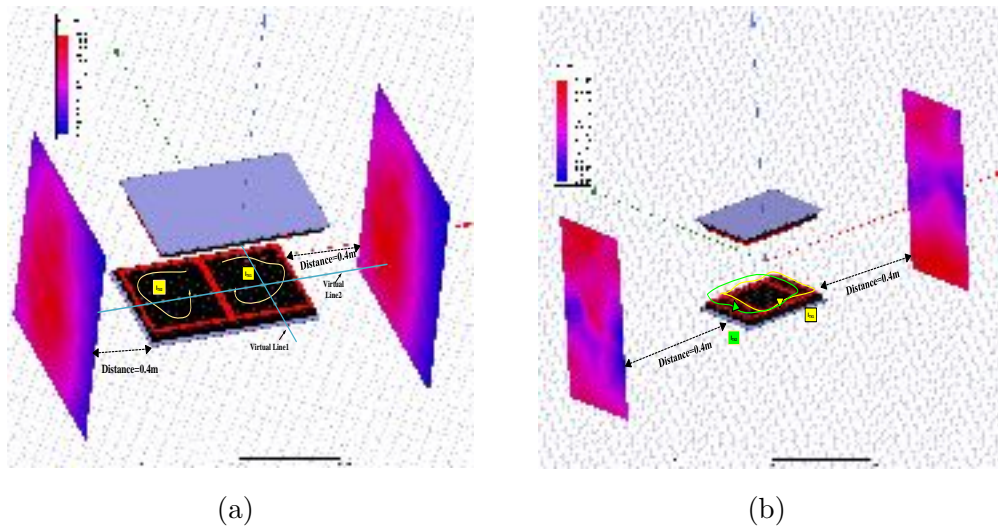


Figure 6.5: Magnetic flux density in 0.4m distance (a) BPP (b) DD Couplers

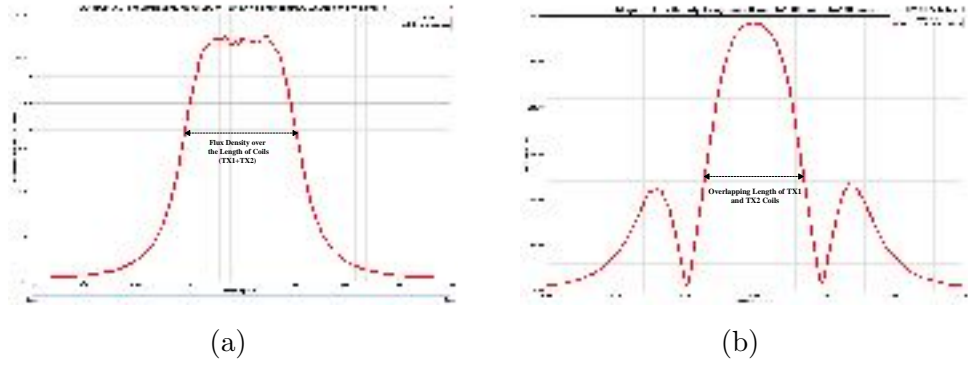


Figure 6.6: Magnetic flux density distribution along Line2 (a) DD (b) BPP Coupler

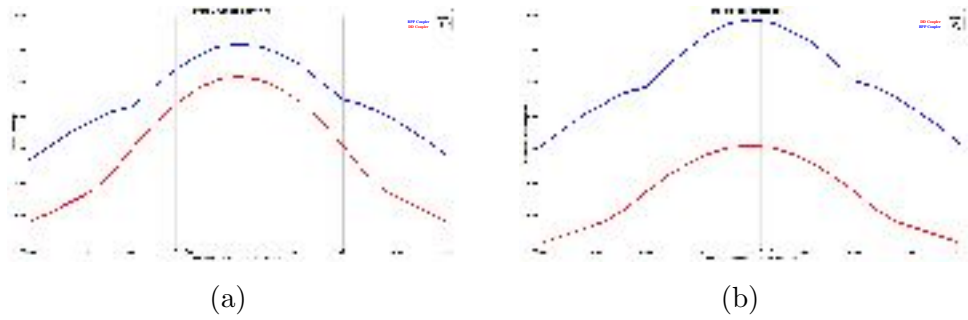


Figure 6.7: Parametric analysis for DD and BPP couplers when the misalignment of transmitter and receiver pads are varied from $-200mm$ to $200mm$ (a) Coupling Factor(%) (b) Mutual Inductance(μ H)

primary/secondary excitation is set at nominal value ($I_{sec} = \frac{\pi}{2\sqrt{2}} \frac{P}{V_B} = 27.65A$, $P = 10kW$), the maximum flux density around the DD coupler exceeds the safe value, however, BPP coupler meets this safety index. The reason being that the two coils (TX1 and TX2) of BPP coupler are magnetically in series in the overlapping zone, while cancelling each other in other zones. To better clarify this concept, the plot of magnetic flux around virtual line 2(as shown in Fig.6.5a) for both DD and BPP models is presented in Figs.6.6a and 6.6b respectively. As it can be seen, the flux density of BPP couplers is high within overlapping length of coils (with maximum value of $285\mu T$), and low in off-overlapping zones. On the other hand, for DD coupler, the flux density experiences narrow high-magnitude zone (with maximum of $112\mu T$) and very low-magnitude in rest of line2.

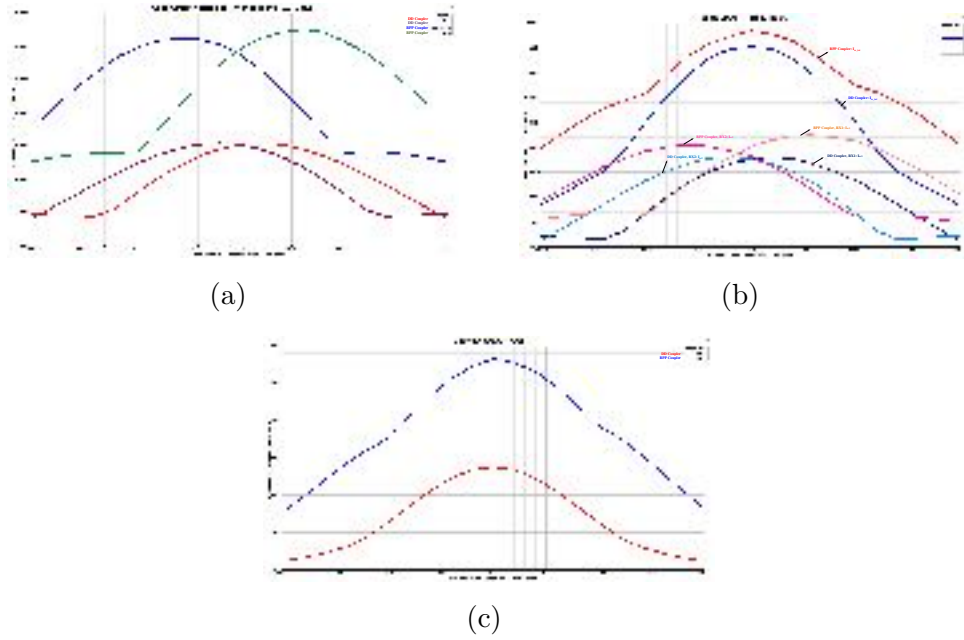


Figure 6.8: Parametric analysis for DD and BPP couplers when the misalignment of transmitter and receiver pads are varied from $-200mm$ to $200mm$ (a) Open Circuit Voltage of RX1 and RX2 (b) Short Circuit Current (I_{sc}) (c) Uncompensated Power (P_{su}) (KW)

6.3.2 Electromagnetic characteristics comparison of DD and BPP

There are some other crucial factors regarding DD and BPP couplers that need to be compared. Their coupling factor, mutual inductance, tolerance to misalignment, induced power in pickup, and so on are also investigated. In this regard, a parametric FEA study is carried out to simulate the dynamic IPT system via defining the secondary position as the variable; leading to misalignment from $-200mm$ to $200mm$ in x-axis. As shown in Fig.6.7a and 6.7b, the magnetic coupling of transmitter and receiver has higher value for BPP compared to DD coupler in all the positions where receiver has moved from $0mm$ to $\pm 200mm$ over transmitter. The reason is due to existence of overlapping zone of BPP coupler in which double coils (TX1 and TX2) is magnetically supporting each other; which can make up the misalignment effect to some extent. However, in DD coupler, the TX1 and

TX2 have almost separated zone of electromagnetic field; not boosting each other; only just supporting in small portion of power pads where their coil width are adjacent. In figs.6.8a, 6.8b, and 6.8c, the effect of misalignment on induced open-circuit voltage of RX1 and RX2 defined as V_{oc1} and V_{oc2} , short circuit current of RX1 and RX2 (defined as I_{sc1} and I_{sc2}), and total uncompensated power (with reference to eq.6.3) are presented for both BPP and DD couplers. As it can be seen, BPP coupler is less impacted with misalignment increase compared to DD, which shows its appropriateness for dynamic EV charging systems.

6.4 Summary

The 3D-FEA model of DD and BPP coupler (being the most effective topologies) for dynamic IPT EV chargers is thoroughly investigated. It was shown that BPP power pads outperform DD power pads in all respects such as electromagnetic compliance, better misalignment tolerance performance, higher coupling factor, and greater power transfer capability.

OPTIMAL DESIGN OF IPT BIPOLAR POWER PAD FOR ROADWAY-POWERED EV CHARGING SYSTEMS

7.1 Introduction

Recently, the conventional plugged-in EV chargers have been transitioned into wireless chargers using Inductive Power Transfer (IPT) systems. Generally, inductive EV charging systems (refer to the conceptual schematic shown in Fig. 7.1) can be realized in two major categories: stationary and dynamic ways. In stationary IPT systems, both vehicle's assembly power pad and ground assembly's power pad are well aligned as well as fixed; however, in the dynamic IPT system, EV can get charged while moving. Some of recent advances in inductive EV charging systems are self-tuned IPT power controller with resonant frequency tracking capability [122] and multi-power level IPT controller [123]. Most of researches in stationary IPT systems are concentrated on power controller improvement, just a few of them are focused on the design optimization of power pad geometry and its configuration. The idea of stationary IPT systems with an intermediary coil is implemented in [109–111] to achieve improved system efficiency, better misalignment, zero phase angle, and constant current/constant voltage characteristic for EV's battery. Authors of [112] categorized power pad configurations into distributed and lumped models, the former, due to elongated configuration is appropriate in dynamic applications where continuous power delivery is essential. Long-track-loop power pads [5, 116] can provide continuous wireless power delivery. However, this type of IPT systems suffer from low efficiency, low magnetic coupling factor, and high self-inductance, making driving the primary coil difficult.

The circular pads are not suitable for dynamic air-gaped EV charging systems which frequently experience misalignment [113], because with the air gap increase, roughly four times increase in circular power pads geometry can compensate the

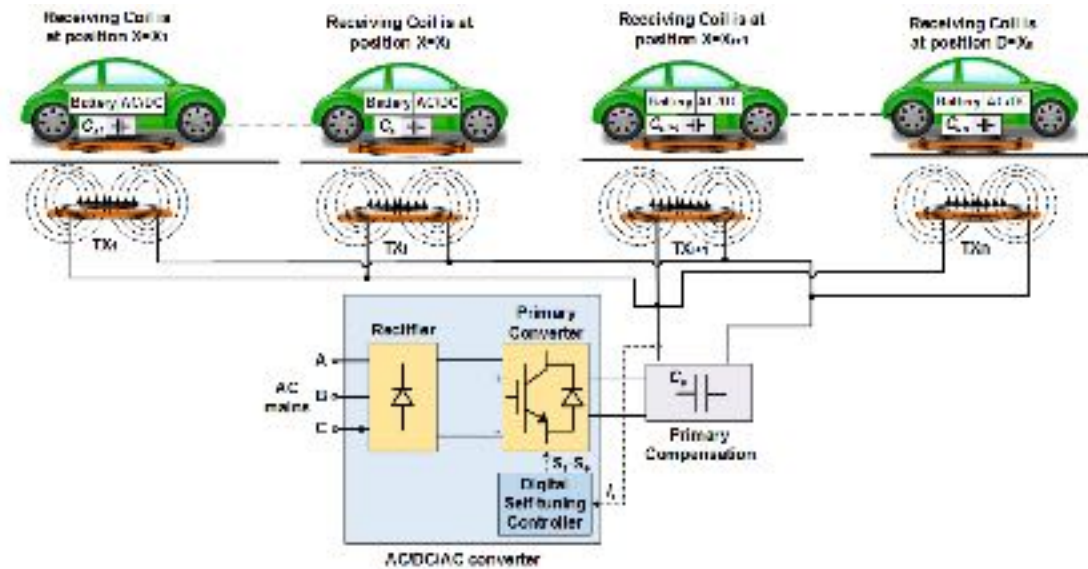


Figure 7.1: The conceptual schematic of IPT roadway-powered track for dynamic EV charging system

power transfer cut [113, 114]. To address this issue and improve misalignment tolerance, Double D-shape coils (DD) is proposed that combines single-sided flux of double coils [112, 124]. Thorough comparative study carries out in [107] to analyze the merits and demerits of DD and Bipolar Power Pad (BPP). Pries et al developed a three-phase couplers which improves power density thanks to rotating magnetic field. The problem with poly-phase multi layer power pads is unbalanced inductance in different phases [115].

In this paper, design of a lumped bipolar power pads (BPP) is presented for dynamic inductive EV charging systems. The main contribution of this paper include the formulation of a multi-objective optimization design algorithm of BPP using accurate FEA-based physics models. The cost of materials, power losses, and tolerance against the horizontal misalignment are defined as the objective functions to ensure practical feasibility of the results. The geometry of the BPP are defined as design variables within the power electronic and electromagnetic constraints. 15 Pareto optimal solutions are obtained NSGA-II based optimization algorithm coupled with FEMM. The results shows the various tradeoffs that can be made based on the objectives highest priority

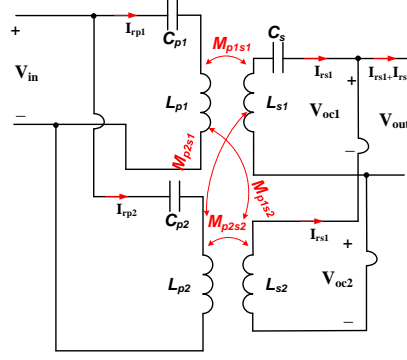


Figure 7.2: IPT systems consists of two primary couplers (TX1, and TX2) and two secondary couplers (RX1, and RX2)

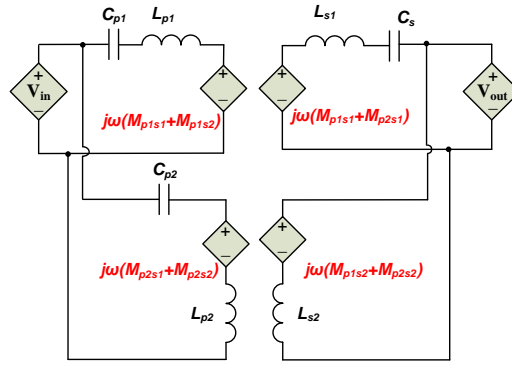


Figure 7.3: Simplified IPT circuit using FHA method

7.2 Power Calculation in double coils IPT systems

IPT typologies comprised of double couplers have gained more interest due to their high efficiency for roadway powered applications ([119, 125]). The circuit schematic of this type of couplers with Parallel-Parallel compensation topology in both primary and secondary sides is presented as shown in Fig. 7.2. To calculate the output power in the secondary side, Fundamental Harmonic Analysis (FHA) is adopted in analyzing circuit (as shown in Fig. 7.3) around the fundamental resonant frequency.

According to [120], the uncompensated power of a typical IPT system with single coil can be expressed as follows :

$$P_{su} = V_{OC} I_{SC} = \omega_r \frac{M^2 I_{rp}^2}{L_2}. \quad (7.1)$$

where, P_{su} , V_{OC} , I_{SC} , M , L_2 , I_{rp} , and Q_2 are the power capacity, open circuit voltage, short circuit current, mutual inductance, secondary self-inductance, primary resonant current, and secondary loaded quality factor, respectively. Likewise, the output power of double-type couplers (either DD or BPP configurations) can be calculated by summing the power of RX1 and RX2 using the following equations.

$$\left\{ \begin{array}{l} V_{OC1} = \omega_r(M_{s1p1} + M_{s1p2})I_{rp1} \\ V_{OC2} = \omega_r(M_{s2p1} + M_{s2p2})I_{rp2} \\ I_{sc1} = \frac{V_{OC1}}{\omega_r L_{s1}} = \frac{(M_{s1p1} + M_{s1p2})I_{rp1}}{L_{s1}} \\ I_{sc2} = \frac{V_{OC2}}{\omega_r L_{s2}} = \frac{(M_{s2p1} + M_{s2p2})I_{rp2}}{L_{s2}} \\ P_{su} = P_{RX1} + P_{RX2} = V_{OC1}I_{SC1} + V_{OC2}I_{SC2} \\ P_{su} = \omega_r \left(\frac{(M_{s1p1} + M_{s1p2})^2 I_{rp1}^2}{L_{s1}} + \frac{(M_{s2p1} + M_{s2p2})^2 I_{rp2}^2}{L_{s2}} \right) \end{array} \right. \quad (7.2)$$

where, ω_r is the radian frequency, M_{sipi} is the mutual inductance between secondary coil i and primary coil i , I_{sci} is the short-circuit current of secondary double coils (RX1 and RX2), V_{OCi} is the open-circuit voltage of secondary coils, P_{RX1} and P_{RX2} are uncompensated power in secondary double coils, while P_{su} is the total uncompensated output.

Equation.(7.2) is used as the power calculation during optimization process for objective function assessment.

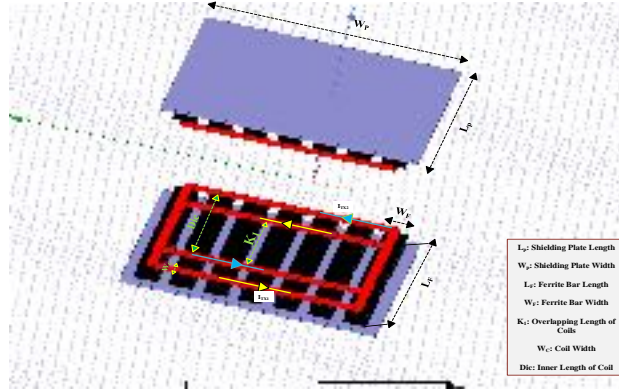


Figure 7.4: BPP 3-D FEA model with all the defined parameters

7.3 Multi-Objective Design of BPP coupler for dynamic IPT systems

Design optimization of BPP coupler using analytical method/equations is almost impossible due to complexity of IPT systems' magnetic structure. Also, the electromagnetic parameters of the magnetic structure cannot be accurately estimated using classical analytical equations. The design parameters to be optimized are shielding plate length, ferrite length, overlapping length of double coils, coil width, inner length of coils, and the number of turn as illustrated in Fig. 7.4. Ferrite core improves the coupling factor by reducing the flux path and the reluctance accordingly. Shielding plates reduce the leakage inductance and stray loss. The design optimization of the BPP is implemented using combined numerical FEA analysis, and MATLAB script. Three important objectives are considered in the proposed optimization algorithm to be minimized. A widely used NSGA-II algorithm, which has many applications in power engineering[126] is used to solve the Multi-Objective Optimization Problem (MOOP).

7.3.1 Objective Functions of MOOP

There objectives are considered for the proposed BPP coupler design optimization algorithm. These objective functions are power loss, cost, and tolerance to

horizontal misalignment (eq.7.3). All the objective functions are explained in following subsections, and parameters of BPP are illustrated in Fig. 7.4.

$$(L_p, W_p, Dic, L_f, W_c, K_1, N) = \min(P_{tot}, C_{tot}, -T_{sd}) \quad (7.3)$$

Coil Loss

Eddy loss in high frequency application are majorly categorized as skin-effect loss and proximity effect loss. Using litz-wire can significantly reduce this loss because the group of bundle woven together makes current flow equal in all strands. The analytical relation of the coil loss P_{Coil} for litz wire is derived by [127] as follows:

$$P_{Coil} = F_r I^2 R_{DC} \quad (7.4)$$

where F_r is the factor relating the DC resistance to AC resistance which includes all the coil's eddy loss. This factor is presented in (7.5) which is associated with frequency (ω), μ_0 as the magnetic constant, N as the number of turns, n as the number of strands, k as the factor of field distribution in multiwinding coil, ρ_c as the resistivity of conductor, and g as the gap between primary and secondary coils.

$$F_r = 1 + \frac{\pi\omega\mu_0 N^2 n^2 d^2 ck}{768\rho_c g^2} \quad (7.5)$$

Ferrite Core Loss

Steinmetz empirical formula for core power loss P_{core} density is given as follows:

$$P_{core} = k_c f^a B_m^b \quad (7.6)$$

where, k_c , a , and b are empirical constants according to the operational frequency of IPT system. The total loss should be multiplied by core volume v .

Shielding Plate loss

By utilizing impedance boundary condition (IBC) as the boundary, the computational size of solving the boundary integral equations can be enormously reduced

[128], as long as the skin depth is significantly lower than the plate size. Using the expression (7.7), the skin depth of aluminium at IPT's operating frequency ($f_r = 85kHz$) is $0.292mm$, which is small and meets the IBC condition.

$$\delta_{ed} = \sqrt{\frac{2}{\omega\mu\sigma_c}} \quad (7.7)$$

where σ_c is the coil's electrical conductivity in (S/m) and μ is the magnetic permeability in H/m . Correspondingly, the finite element model of IPT system can be simplified, and the plate loss can be expressed subsequently as (7.8).

$$P_{plate} = \sqrt{\frac{\mu\omega}{2\sigma_p}} H^2 \quad (7.8)$$

where H is the magnetic field in A/m and σ_p is the plate's electrical conductivity in (S/m) . Therefore, the total power loss in the IPT system, from subsections (7.3.1, 7.3.1, and 7.3.1), can be expressed as (7.9):

$$P_{tot} = P_{plate} + P_{Coil} + P_{Core} \quad (7.9)$$

7.3.2 Cost function

The total cost of the components including shielding plate, ferrite cores, and litz-wire conductor is of great importance in the design process. As given in (7.10), the price of each component is presented for shielding plates, ferrite bars and coils as the function of the their corresponding geometries.

$$C_{tot} = (2W_c + 2Dic - k1)(2W_c + Dic)dp Cp + 8(Dic + Wc)N_c Cc + N_f W_f L_f d_f C_f \quad (7.10)$$

where C_p , C_c , and C_f are the cost coefficients of the Litz wire, ferrite core and aluminum plate respectively. All the geometric parameters of the IPT's power pad are illustrated at Fig. 7.4.

7.3.3 Horizontal Misalignment Tolerance

As another major goal of the BPP design for dynamic IPT application, the high tolerance to misalignment is of great importance. For this aim, in each iteration of FEA-based NSGA-II algorithm for each individual of population, the uncompensated power (named as P_{sud}) under horizontal misalignment of $d=200\text{mm}$ is calculated using eq.7.2, and then is used to assess the tolerance criterion as expressed in (7.11).

$$T_{sd} = \frac{P}{P_{sud}} \quad (7.11)$$

where, P is nominal power in the well-aligned position of IPT system. The lower the sensitivity of the factor (T_{sd}) to horizontal misalignment, the more tolerant the BPP design.

7.3.4 MOOP Constraints

There are three major types of constraint defined for MOOP design of BPP which include geometric constraints, maximum allowable EMF, and power electronic limitations.

looking into geometric constraint, the design decision variable as shown in Fig. 7.4 are Dic , W_c , k_1 , L_f , N .

These variable values should be within their upper/lower bounds. Regarding the maximum allowable EMF constraint, in each iteration of MOOP, the EMF of each design should be always below the maximum electromagnetic field to satisfy the ICNIRP safety guidelines ($EMF \leq EMF_{max}$). In regard to power electronic limitation, primary/secondary converters are stressed by Volt-Ampere of primary/secondary coils ($S = \sqrt{Q_s^2 + 1}$), therefore in each iteration of MOOP the quality factor (Q_s) should be checked to ensure its in permissible ranges ($4 \leq Q_s \leq 10$).

The Proposed multi-objective optimization algorithm flow chat is as shown in Fig.

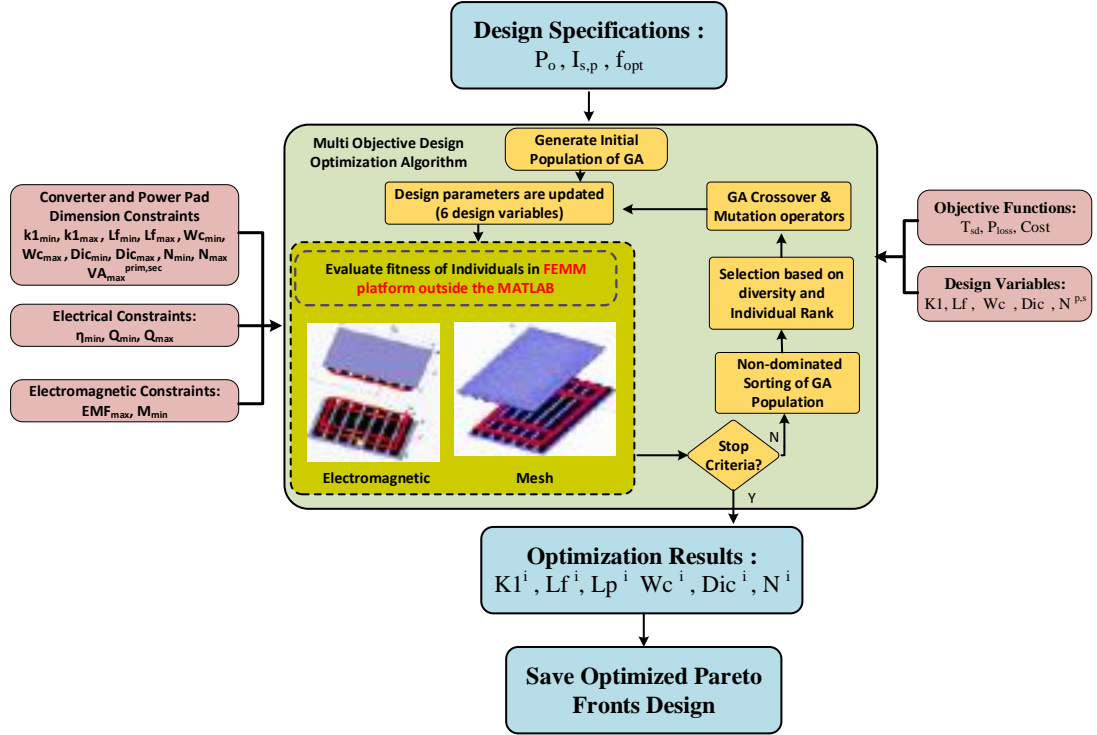


Figure 7.5: The proposed multi-objective time-harmonic algorithm using co-simulation of FEMM software and MATLAB

7.5. The algorithm starts with the definition of the design specifications (P_o , $I_{s,p}$ and f_{opt}), then the initial population of the variables are generated within the variable constraints. The geometry is built and the electromagnetic physics model is applied for evaluation of the objective functions (evaluation of fitness) which should satisfy all the converter, electrical and electromagnetic constraints. New generation of variables are evaluated until the stop criteria is met. The Pareto optimal results are saved as the optimal design for the MOOP.

7.4 MOOP Implementation

The MOOP is implemented using NSGA-II algorithm to find optimal geometries of BPP coupler for 10kW IPT system with the air gap of ($g = 200mm$) as the case study. Copper, aluminium, MnZn N87 materials are used as the materials for coil, plate and ferrite bars, respectively. The cost coefficients of the materials (copper,

aluminium, ferrite bars) are $C_p = \$37600/m^3$ $C_f = \$0.18/cm^2$ $C_c = \$2.04/m$. The operational frequency of IPT system is selected as $85kHz$ as recommended in SAE J2954 [129]. The optimization script is developed in MATLAB (with NSGA-II algorithm as the optimization solver). For each individual generations, a 2D-FEA model geometry is built in FEMM via magnetic preprocessor command set. The 2D FEA model coupled to MATLAB is used to get the electromagnetic parameters value such as mutual/self inductance, flux density, magnetic potential, and so on in order to evaluate the loss and tolerance of each design as shown in the flowchart in Fig. 7.5. The solver stops either when the maximum number of generations is reached to 1000, or when the average change in the spread of the Pareto front over the generations is less than $1e - 3$).

After the implementation of FEA-based multi-objective design optimization al-

Table 7.1: Pareto optimal solutions obtained for a design optimization of BPP couplers for $10kW$ IPT system

Solution	BPP Design Parameters						Electromagnetic Parameters				Objective Functions		
No. #	L_p	Dic	L_f	W_c	k_1	N	M_{s1p1}	M_{s1p2}	K_{tot}	L_p	$\eta(\%)$	Cost(\$)	$D_h(mm)$
PFS-1	311.33	124.5	99.34	21.47	30.64	16	7.6	5.31	28	92.23	87.68	112.39	22.44
PFS-2	357.94	236.5	231.3	10.03	185.15	15	20.6	1.57	23.41	189.5	92.07	226.07	283.78
PFS-3	290.7	166.1	190.7	14.5	120.6	15	13.9	2.82	27.02	124.2	90.6	177.95	148.92
PFS-4	351.6	233.6	231.6	10.36	186.3	15	19.73	0.61	21.80	186.62	91.166	225.198	260.1
PFS-5	242.25	115.8	222.2	23.3	86	16	11.82	10.71	10.71	229.41	94.45	187.43	31.33
PFS-6	352.6	233.2	233.2	10.6	185.1	15	20.52	0.96	23.29	184.62	91.80	226.29	285.91
PFS-7	310.04	180.33	188.1	13.7	128.03	14	12.84	3.24	27.86	115.54	90.01	177.69	137.22
PFS-8	292.7	150.1	161.34	18.44	94.4	16	12.52	4.7	30.16	114.18	90.932	158.53	108.7
PFS-9	274.6	127.2	144.4	20.7	71.2	16	9.73	4.48	30.36	93.67	89.18	140.81	72.49
PFS-10	302.9	162.9	172.1	17.5	108.1	15	12.43	3.98	29.6	111.02	90.29	166.53	117.8
PFS-11	258.45	88.1	112	28.05	23.9	18	7.16	4.87	32.04	75.17	87.4	113.94	37.73
PFS-12	269.2	104.9	126	26	42.6	17	8.44	5.03	33.16	81.24	88.78	126	53.6
PFS-13	359.3	211.4	206.4	19.5	152.5	15	16.25	2.65	27.27	138.74	90.52	205.91	209.84
PFS-14	271.8	116.7	131.5	20.9	53.4	16	8.86	5.15	32.83	85.29	89.47	129.28	56.64
PFS-15	358.4	236.5	231	10.21	185.2	15	20.43	1.52	23.24	188.9	91.96	225.97	278.86

gorithm, 15 Pareto Optimal Solutions (PFS) are achieved as the optimal BPP designs as presented in Table.7.1. As it can be seen, the obtained solutions are non-dominated with respect to each other, meaning that none of them is better than others in all objective functions. The magnetic mutual inductance of M_{p1s1} , and M_{p1s2} are added to the Table.7.1; due to identical geometry of RX_1 and RX_2 coils in the receiver, as well as that of TX_1 and TX_2 coils in the primary side,

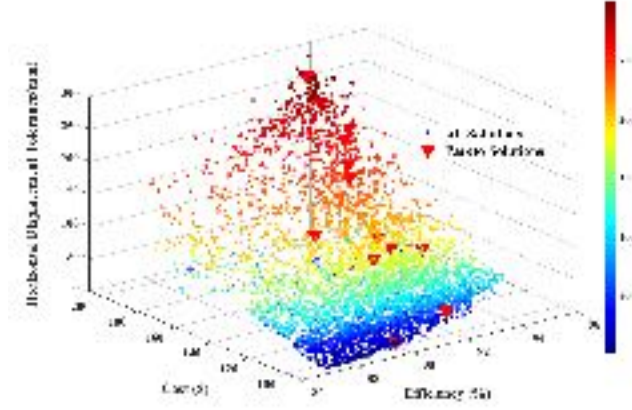


Figure 7.6: 3D-plot of objective function values of all the solutions along with Pareto optimal solutions

the inductance matrix has a symmetric feature, therefore, $M_{p2s2} = M_{p1s1}$, and $M_{p2s1} = M_{p1s2}$. The total coupling factor of IPT design with the BPP couplers is also added to the table, which is defined as k_{tot} . Moreover, η , and D_h which are the efficiency, and horizontal tolerance of each solution (PFS-#) is also included in the table. Decision maker can select any of the optimal solutions based on design preference. For instance, if the cost is of higher priority, the PFS-1 can be selected. On the other hand, if the misalignment tolerance is of more importance for the IPT application, the PFS-6 can be opted for, which is tolerant to misalignment as large as $285.91mm$.

By taking a thorough look at the optimal solutions, it can be easily seen that with higher values of overlapping length of coils (k_1) and ferrite length (L_f), the tolerance of IPT system increases, which unfavorably increases the price, showing the conflict of objective functions. Another observation from this study shows that with decrease of the inner length of coils (Dic) and increase of coil surface (W_c), the efficiency of IPT system can reach its maximum value. Fig. 7.6 is presented to show the 3D-plot of all three objective functions for all the feasible solutions found during the optimization process, along with the Pareto optimal solutions (distinguished from others with red-colored triangles). The MOOP took 7 hours and 43 min to be completed. During the optimization process, GA updated 158

generations before finding the final Pareto optimal surface, and, in total 4795 valid solutions (possible designs) were found and assessed during this long process.

7.5 Validation of the proposed Algorithm

To analyze the Pareto Solutions achieved through multi-objective optimization, a case study of two Pareto front solutions (PFS-1 and PFS-6) is presented. The receiving and transmitting pads' geometries are built with the parameters of PFS-6 and PFS-1 as shown in Figs 7.7 and 7.8 respectively.

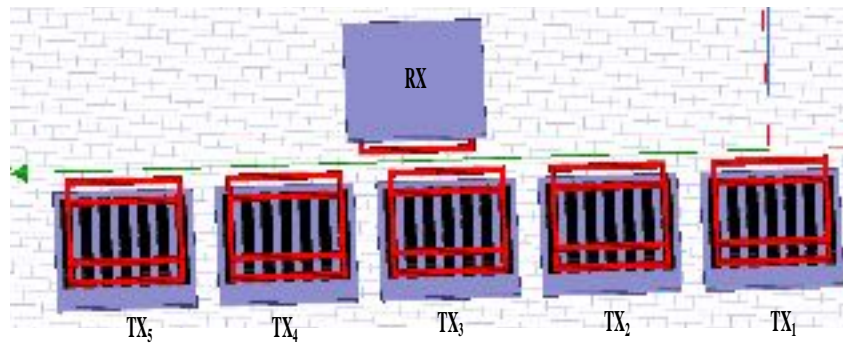


Figure 7.7: Validation study: receiver(RX) and IPT track(TX_i is set with PSF-6 design

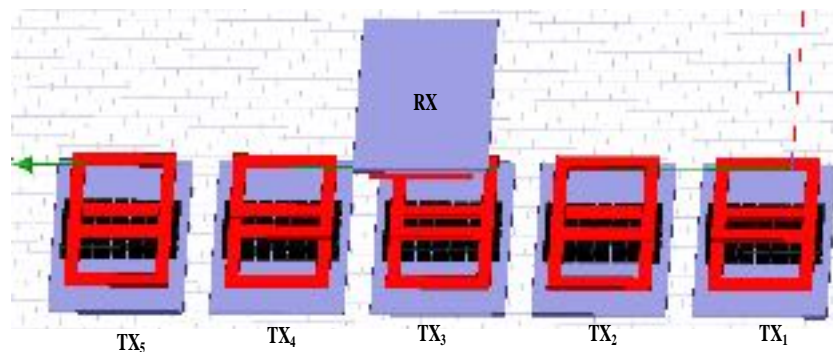


Figure 7.8: Validation study: receiver(RX) and IPT track(TX_i is set with PFS-1 design

The 3D-FEA analysis is carried out for both design in ANSYS MAXWELL, since the 3D model is much more accurate than 2D. In this case study, the dynamic

performance of IPT charger in the track is compared for the selected designs. The two IPT tracks composed of 5-transmitting couplers are shown in Figs.7.7 and 7.8, in which PFS-1 and PFS-6 designs are utilized in both receiving and transmitting couplers. The noticeable difference of these two design solutions is that PFS-6 has larger overlapping width (k_1) as well as ferrite length (L_f) than PFS-1 (as shown in Table 7.1).

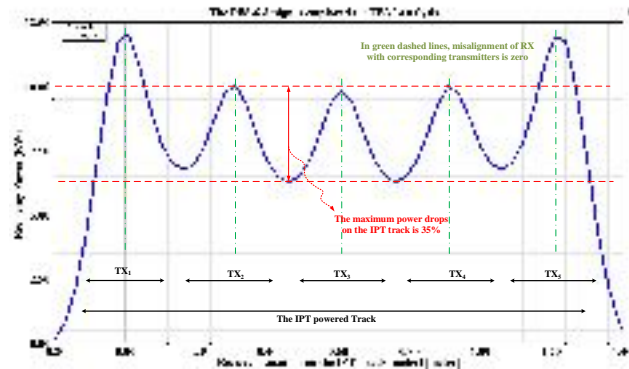


Figure 7.9: Receiver Power and coupling factor with PSF-6 design

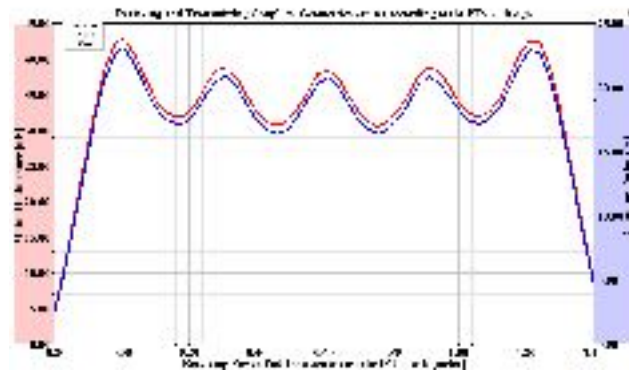


Figure 7.10: Receiver mutual inductance with PSF-6 design

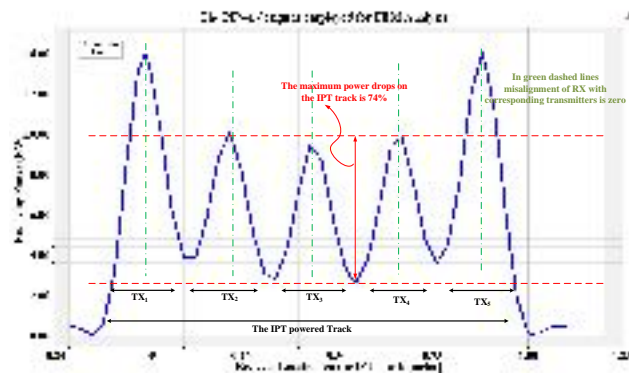


Figure 7.11: Receiver Power when IPT track is set with PSF-1

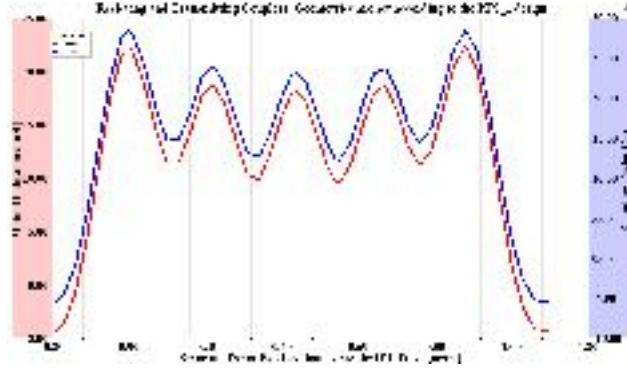
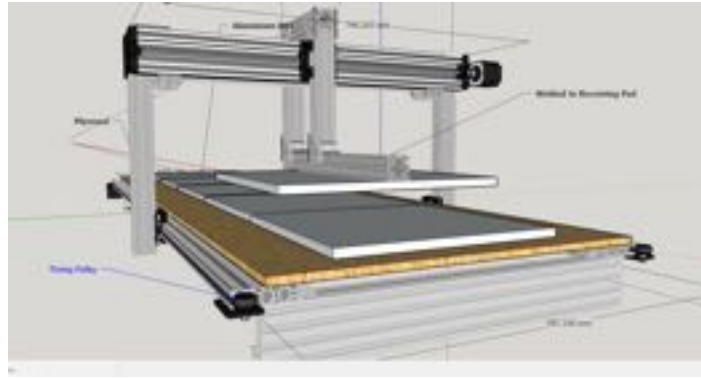


Figure 7.12: Mutual inductance and coupling factor when IPT track is set with PSF-1 design

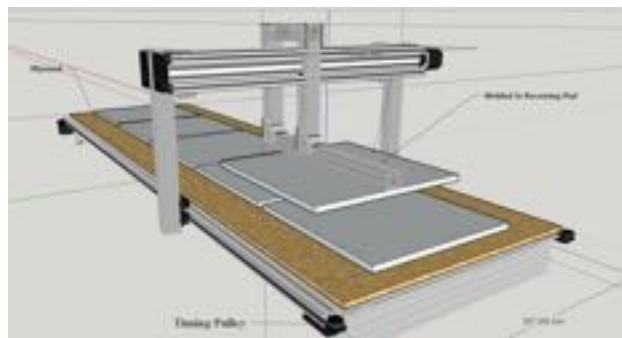
The electromagnetic and electrical results are presented when the transmitters and receiver geometries set according to the PFS-6 design. The plot of the output power in the receiver (RX) versus receiver location sweep over the IPT track is shown in Fig. 7.9 . Additionally, the mutual inductance of receiver and its coupling factor with the transmitters throughout the IPT track are shown in Fig. 7.10.

The green dashed lines in the power plot indicate the positions where the receiving pad (RX) is in zero misalignment with respect to the transmitting power pads (TX_i , $i=1:5$); therefore, the mutual inductance, the coupling factor and accordingly the power transfers are maximum ($10KW$) in these locations of the track, and in the rest of the track, the power transfer falls below the rated charging level ($10KW$) due to misalignment.

For comparison purpose, the same scenario is repeated when the couplers parameters are set according to the PFS-1 design; and, the power in the receiving power pad is shown in the Fig. 7.11, and the mutual inductance along with the coupling factor are represented in the same plot (see Fig. 7.12). It is evident that the power drop is lower when the couplers are set based on the PFS-6 design compared to that of PFS-1 design. As can be seen from Fig. 7.9, the difference of the maximum power (occurring in well alignment) and the minimum power (happening in maximum misalignment) in case of the PFS-6 design utilization is only 35%, which is significantly lower than the amount (74%) achieved for PFS-1 design re-



(a)



(b)

Figure 7.13: CNC design of the experimental setup according to "POS-6" design values

ferring to Fig. 7.11. This index (difference of power at the least misalignment and greatest misalignment) is a good indicator of power transfer capability over the track, however, one designer may compromise power transfer in favor of cost. For instance in this case, although, the PFS-1 design has relatively large power transfer variation as shown, it is very cost-effective design (cost=112.39\$) due to less ferrite bars used in this design compared to PFS-6 which is considerably expensive (cost=226.29\$). This is exactly where the practicality of the proposed multi-objective design algorithm lies in; that can be of great contribution for designers.

7.6 Dynamic IPT system based on "POS-6" parameters

The design parameters of "POS-6" is used to construct the IPT roadway powered track; which is composed of 5 transmitting BPP couplers juxtaposed with gap of $50mm$ with respect to each other. The CNC design via sketchup software is used to build the mechanical structure for mounting IPT track, and secondary mover that can bear mechanical load as much as receiving coupler weight. The pulley actuator run by two step motors mounted in either legs of handle can make movement for the pickup along the IPT track. Moreover, for applying misalignment to the IPT setup, the receiving pickup structure is equipped with a step motor mounted vertically which can add or remove misalignment. In the Fig.7.13, the CNC design of setup is shown, this helped us to find the exact dimensions for the IPT frame based on the available materials in the market before proceeding with the construction. In the Fig. 7.14, the experimental setup of the dynamic IPT system using "POS-6" is presented. The future dynamic tests will be carried out on this setup.



Figure 7.14: The experimental setup for dynamic IPT system which is built based on "POS-6" design values

7.7 Multi-Level Power Controller Design for Dynamic Wireless Electric Vehicle Charging Systems

The global use of electric vehicles (EV) is on the rise[1]. Several technologies for charging the EVs have been developed over the years namely: plug-in electric vehicles, static wireless charging systems. The problem with stationary wireless charging systems (SWSC) is that they should be parked in car garages for a long time which makes SWSC less acceptable by the society. Furthermore, other issues of SWSC like high battery size, bulky structure, high electromagnetic emission speed up the transition from static to dynamic wireless charging, and it brings up a user-friendly benefit for EVs' users by the ability to get charged in motion. Another advantage of dynamic wireless power transfer (DWPT) is less need to use the large size battery which is a must in static wireless charging systems. To realize wireless power transfer, there are three major methods: inductive power transfer (IPT) [1, 9, 130–132], the capacitive power transfer (CPT)[133], and combination of IPT with CPT systems [4]. IPT technology utilizes magnetic field to transfer power, and its DC source to DC load efficiency in some applications has reached to 96.6% [134]. Though the concept of dynamic wireless power transfer (DWPT) is still an emerging one, a couple of solutions have been proposed to address the challenges faced with DWPT systems. Generally, there are three major categories for primary coupler configuration for dynamic IPT systems, long-track-loop transmitters[5], and short-individual transmitters[6]. A long-track-loop transmitter structure has two problems: first, high self-inductance caused by long-track-loop transmitter can limit the IPT's resonant frequency, second, low coupling coefficient of this coil system decreases the IPT systems' efficiency and makes it impractical for dynamic IPT systems[5, 7, 116]. On the other hand, segmental array of couplers as the second configuration is introduced which can be connected in either parallel or series to the same primary converter. This kind of coupler

system can solve the high self-inductance problem of the long-loop coupler, however it can cause power pulsation problem as pickup move away transmitter by transmitter[9, 105, 135]. To solve this problem, several rectangular transmitter are composed side by side to form a tracking lane that realizes a continuous dynamic power transfer [8, 136, 137] with zero space between adjacent transmitting couplers. However, this kind of coil configuration wastes transferred energy through negative coupling created between adjacent couplers, thereby reducing the total efficiency of the IPT track.

This paper proposes a simple logic control control strategy for DWPT which tunes the primary resonant current in a real time. A soft-switched bidirectional single-phase direct ac-ac matrix converter(MC) is employed to apply the proposed multi-level power controller. The power transfer drop due to the misalignment is compensated by by multi-level power controller which increases the number of power transfer level; the number of power transfer level can be regulated from 0-*Level* to 16-*Level* according to the secondary pad's position. In the rest of the paper, FEA analysis for a dynamic receiver(*RX1*) pad moving along three road-embedded pads ($TX_{i,i=1,2,3}$) is given in section II. The formulation of the proposed 16-discretized current levels for the DWPT is given in section III. The single-phase direct AC/AC matrix converter(MC) with the multi-level power controller is illustrated in subsections(A, B, C, and D), and finally simulation results on a case study is presented.

7.8 Finite Element Analysis(FEA) for DWPT

In Fig. 1.1, a typical IPT system with multiple transmitters array connected in parallel is shown . This system is composed of power converters, loosely coupled magnetic structures and compensation components. This dynamic charging system is a dynamic contactless EV charging system while they are moving on the roadway powered tracking lane. Dynamic study of magnetic characteristics is of

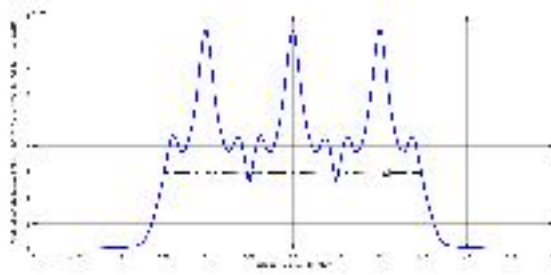
great importance when the receiver pad attached to the vehicle (RX_1) moves along the transmitter coils ($TX_1, TX_2,$ and TX_3) (as shown in Fig.1.1). The changeover's function is to de-energizes an active transmitter coil and energizes the next transmitter coil in specific times. The transition times happen at the efficient point where the mutual inductance of (RX_1 and TX_i) equals (RX_1 and TX_{i+1}), this avoids wireless power transfer from decreasing. FEA is studied for the dynamic wireless charging EVs using parameters given in the table. 7.2. The electric vehicle's speed is assumed $V = 20\text{mile}/\text{hour}$, the primary pad diameter, and the distance between primary pads are considered 700 mm and 200 mm respectively; accordingly, the time takes for vehicle to cross each transmitter coil surface (TX_i), and the gap between primary pads are 7.95 ms and 2.27 ms respectively.

Parameter	Value/type
Aluminum Shielding Diameter	800 mm
Air Gap	200 mm
Ferrite Diameter	380 mm
Distance between segmented transmitter coils ($TX_1, TX_2,$ and TX_3)	200 mm
Coils Diameter(RX_1 and $TX_{i=1:3}$)	700mm
number of turns	25
Velocity of vehicle	20 mile/h

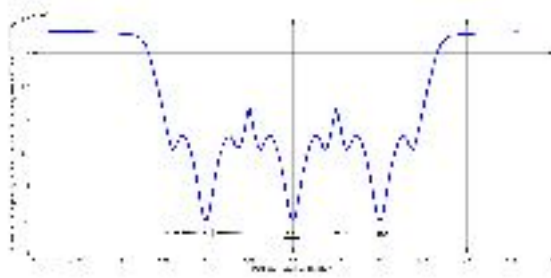
Table 7.2: Inductive power transfer setup characteristics

FEA analysis is done using ANSYS Maxwell for the DWPT and the results for mutual inductance and the resonant frequency (using Eq.7.12) are represented in figures (7.15a and 7.15b). As it can be seen from results, when mutual inductance gets maximized in complete alignments of RX and TX_i , correspondingly, the resonant frequency is nominal designed value (85KHz) in those mentioned positions.

$$\omega_r = \sqrt{\frac{1}{L_p C_p} - \frac{R_L^2}{4L_p^2}} \quad (7.12)$$



(a) Mutual inductance between RX and TX_i as vehicle moves all the way from TX_1 to TX_3



(b) resonant frequency as RX moves all the way from TX_1 to TX_3

Figure 7.15: FEA study for dynamic wireless power transfer

7.9 Proposed Control Methodology based on resonant current discretization

A series-series topology is recommended topology, first, because, in this configuration, the design of compensation tanks is independent of the coupling and secondary load changes, second, primary current tuning is easy in this topology compared to other typologies. The major problem of dynamic charging systems is how to address the coupling rate's change in wireless EV charging systems as vehicle moves along transmitter pads. The output power given in equation 7.13 clearly explains that the resonant frequency, secondary side quality factor, mutual inductance, and load could significantly affect the output power in dynamic charging system.

$$P_{out} = \omega_s \frac{M^2}{L_s} I_{rp}^2 Q_s. \quad (7.13)$$

Theoretically to compensate these reductions, the primary resonant current should be regulated at every location on track real-time. Considering the sec-

ondary side-battery specification as $P_{bat} = 24KW$, the reference of primary resonant current can be calculated using Eq.7.13 to deliver fixed power $P_{bat} = 24kw$ in each position on the roadway IPT. As it is shown in Fig.7.16, the reference primary resonant current (blue plot) with considering the fixed delivered output power(24KW) all across the roadway($TX_i, i = 1 : 3$) is calculated as continuous current signal(blue plot), and is discreteized using 16-different levels(red plot). In the next section, the current controller which can produce these 16-different current level is designed and explained.

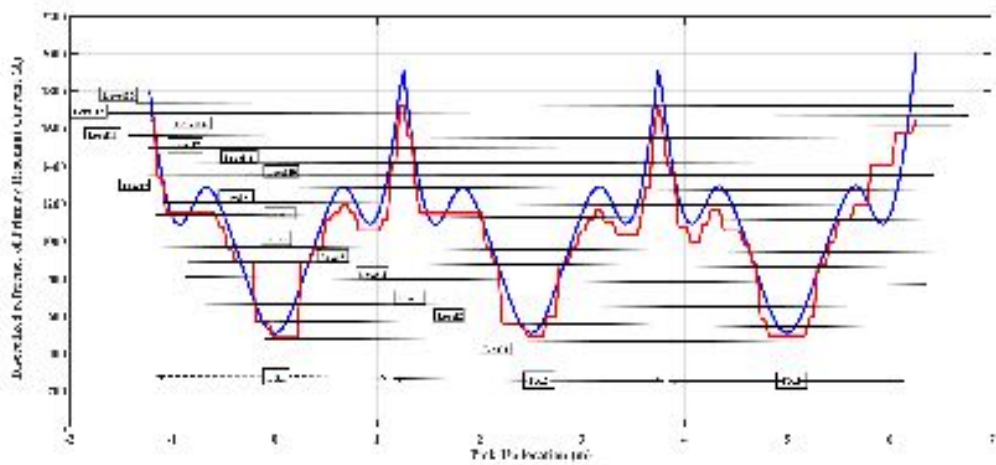


Figure 7.16: The depicted 16-discretized reference levels of the primary resonant current for IPT-roadway having three transmitters ($TX_i, i = 1 : 3$)

7.9.1 Control Logic Design

The section presents the design steps for the proposed controller using simple logic circuits with the theoretical formulations of the power transfer. The magnitude of primary resonant current can be regulated by the number of the energy quantum to be transferred from the primary resonant tank to the secondary side. The control circuit is designed this way that, the primary resonant current is considered as a clock signal (CLK)(high for positive values, and low for negative values). The controller design (as shown in 7.17 is the same as what presented at chapter3. 3.2,

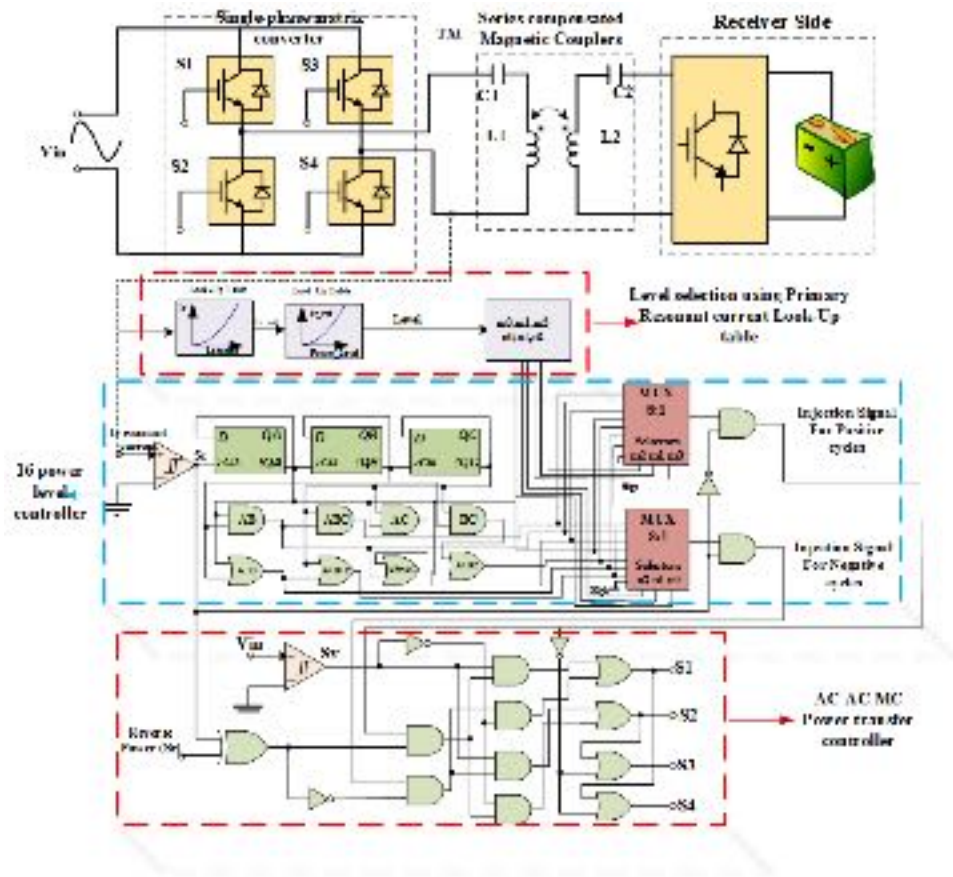


Figure 7.17: Proposed control of DWPT for matrix converter for primary current regulation according to pickup side position

therefore the excessive explanation will not be provided accordingly with only some few adjustments to make it applicable for AC-AC matrix Converter. It is worth to note that the values of multiplexers' selectors bits $((m_0, m_1, m_2)$ and $(n_0, n_1, n_2))$ are selected in a real time way corresponding to the pickup location. Location vs power level number is used as a reference look-up table which is included in control loop as shown in the Fig.7.17.

7.9.2 Matrix Converter power controller logic

The same switching logic of direct single-phase AC/AC matrix converter proposed in [106] is used in this paper for energy injection/regeneration modes; the sign of both input voltage (V_{in}) and primary resonant current is employed as a logic for energy injection when $S1$ and $S4$ conduct at the same time, and opposite signs

of these signals is used for regeneration mode $S1$ and $S4$ conduct at the simultaneously.

The outputs of two mentioned multiplexers as a negative half-cycle pulses and positive half-cycle pulses combined with input voltage signal are used to define the gate signals of switches ($S1, S2, S3$, and $S4$). For more detailed explanation about single-phase soft-switched AC-AC MC converter used in this paper, refer to [106].

7.9.3 output power Calculation for IPT as function of selected level

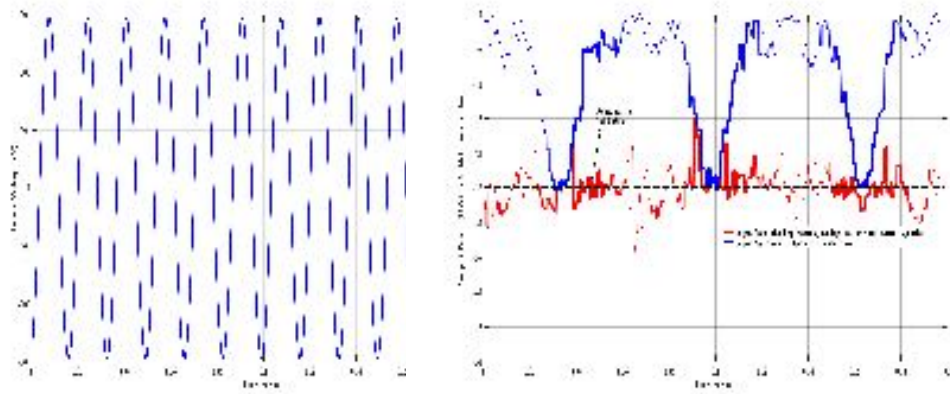
Fundamental harmonic approximation (FHA) is used to calculate the output power according to the specified power level. As explained with thorough details in reference([138]), the output power is calculated as function of m and n , which shows the output power relation when transfer power level is $L = m + n$.

$$P = \frac{4\sqrt{2}DV_{in}V_B}{\pi^2\omega M} \quad (7.14)$$

where, m number of positive half-cycles and n number of negative half-cycles, $D = (m + n)/16$ is duty cycle, V_B is battery voltage, V_{in} is input grid AC voltage, ω is resonance frequency.

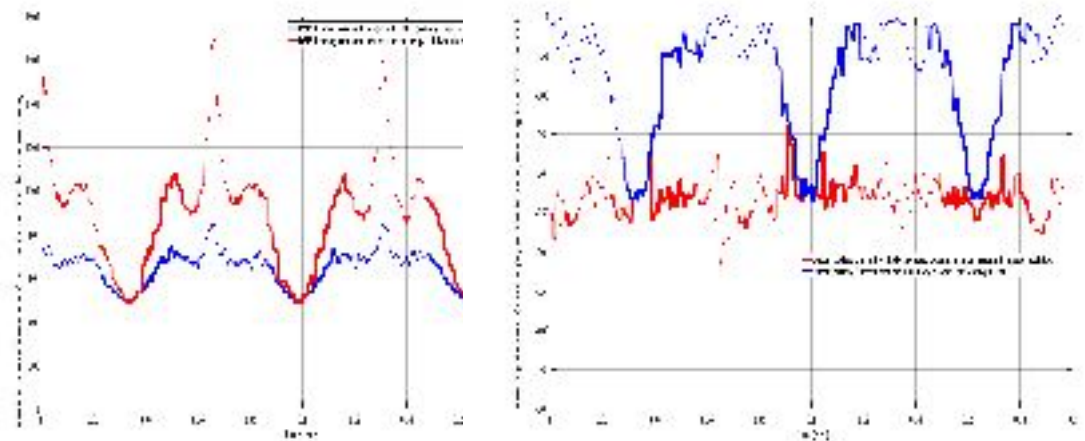
7.10 Simulation and Result Analysis

Dynamic wireless power transfer as shown in fig. 1.1 is modeled using combined MATLAB and ANSYS MAXWELL software to simulate the vehicle moving on embedded transmitters, this study is carried out to show the impact of the proposed multi-level power controller on dynamic wireless power transfer. The specifications of a DWPT for the simulation are presented in table.7.3. The Fig.4a, shows the the AC 60HZ input voltage's cycles as vehicle moving (RX_1) over $TX_{i=1:3}$



(a) Input AC 60HZ voltage cycles

(b) output power



(c) Resonant Current

(d) Battery Current

Figure 7.18: ANSYS combined with MATLAB simulation results as RX_1 moves all the way from TX_1 to TX_3

surface. In all the simulation results given in figure 7.18, the red plot shows the results obtained with the proposed primary resonant current regulation method on the DWPT, and the blue plot shows the results of studied DWPT with the constant primary current reference. The constant primary current reference is assumed ($I_r = 479A$), as with this reference current, the delivered output power of $P_{out} = 24kw$ to the secondary can be possible just in complete alignment of pads. Figure 4b clearly shows the $P_{out} = 24kw$ in almost all roadway-powered

Table 7.3: Specifications of the simulation for the dynamic IPT system

Parameter	Value
Grid voltage (V_{L-N})	208V
IPT system operating frequency at zero misalignment	20 kHz
Compensation capacitors (C_p, C_s)	20.38 μ F
Battery voltage (V_b)	100 V
Battery capacity (C_b)	24 kWh

WPT using the proposed real-time regulation of primary resonant current. However, with the fixed current control, the transferred output power decreases almost in all parts of track except in alignment locations. Figure 4c shows that the primary resonant currents is tuned in all locations by the multi-power level controller applied on DWPT; in locations other than alignments, the resonant current is relatively increased to compensate the lower coupling values. In other words, the multi-level power controller starts with 16th level of energy injection which means the power transfer happens in all positive and negative cycles; however, as vehicle moves toward the center of transmitter pad, the coupling rate increases, as a result the primary current reference decreases. The power level gradually decreases and reaches to 1st level at the complete alignment positions (according to the plot at $t_1 = 0.035, t_2 = 0.1, t_3 = 0.163$), and the power level again starts increasing from 1st level to 16th level when vehicle moves forwards, this is repeated as EV moves across either of transmitters. Figure 4d shows the battery current installed in vehicle. The battery Current of receiver (red plot) is kept fixed at about 250A with the use of the proposed multi-level power controller, however the battery current (blue plot) with the constant reference of primary resonant current method varies due to coupling change.

7.11 summary

A multi-objective optimization algorithm to find the optimal geometries of BPP coupler is proposed and implemented. The parametric optimal design of BPP is carried out through scripting in MATLAB interfaced with FEMM software.

In each iteration of NSGA-II algorithm for all generation of variables, the corresponding 2D-FEA model is created in FEMM software; the loss, and tolerance as objective functions are evaluated correspondingly. For practical feasibility, the cost of each design is also considered as another objective function in the MOOP. Finally, 15 Pareto optimal solutions were achieved for 10kW IPT system used as a case study. Two of the Pareto optimal solutions were further analyzed to validate the proposed algorithm. The achieved optimal solutions gives the designer a wide range of optimization results for IPT EV application . As a future work, the IPT roadway powered track will be constructed for dynamic EV application following "PFS-6" geometries.

FPGA-BASED IPT POWER CONTROLLER**8.1 Introduction**

Inductive Power Transfer(IPT) systems have taken more attention recently for charging applications including Electric Vehicles, scooter, electric aircraft, wheelchair and so on. This emerging technology has become marketable by different auto-manufacturers, which shows the pace of advance and progress of it. Most of advancements in IPT systems have been carried out on power transfer controller, and switching logic improvement. The necessity of designing multi-level converter which could change the IPT power level in a wide range is always sensed. This variable power level can make the wireless charger usable in different applications from a KiloWatt (such as scooter, wheelchair etc) to tens of KiloWatt such as EV. As an example, users may want to get their different devices charged using only one wireless charging system, this highlight the importance of having user-friendly adjustable IPT charging level controller.

Due to inherent dynamic of IPT systems, the constant power delivery to the secondary coupler is hard to achieve unless adaptive IPT power controller to be used. Among many dynamics, misalignment [139, 140], load variation[141] are much significant which makes IPT system run in off-tuned condition; leading to efficiency reduction as well as power transfer drop. Specially, for inductive EV chargers in dynamic operation (in motion), frequent misalignment experience is unavoidable as EV moving across IPT track comprised of array of multiple lumped couplers[124, 142]; leading to extreme coupling factor variation. To make up the load variation, different compensation topologies are introduced in different investigations including double-sided LCC [4], double-sided LCL [5], LC/S [6], S/LCC [7], S/CLC [8], and S/SP [9]; which resulted in appealing misalignment tolerance characteristics. Some other researches have proposed impedance network match-

ing to maximize the power transfer rate [143]. In [144], the impedance matching network in the secondary side is emulated using the phase shift control applied in the secondary converter. recent investigations are shifted toward self-tuned multi-power level IPT controller that lead to adaptive adjusting of the power level to make up the power dips in misalignment conditions[123, 145, 146]. The self-tune capability in these researches are realized through the resonant frequency-tracking design.

In this chapter, 32-Power level power controller synthesizable in HDL platforms such as FPGA will be explained. Some other challenges of switching such as how to add deadtime between upper and bottom switches of each leg of a high frequency AC-AC matrix converter will be discussed. finally the experimental results along with Modelsim simulation results will be shown to evaluate the proposed system.

8.2 Multi-Level Power level controller for AC-AC Matrix Converter

IPT systems for bidirectional operation require two series common-source switches in each module ($SW_{i=1:4}$) as shown in Fig.8.1. The shown topology can be connected to the main grid without any need of DC conversion or DC interface; reducing the cost as well as increasing the reliability of the IPT charging system. As shown in Fig. 8.1, only measurements of primary resonant current (I_r) and main AC voltage measurement (V_{AC}) are required. The *Sign* function is applied on measurement signals which results in $S_v = \text{Sign}(V_{AC})$ and $S_i = \text{Sign}(I_r)$ and inputted into the IPT power controller (in this case FPGA digital platform). The Matrix converter directly converts from AC 60Hz into high resonant frequency using primary full bridge inverter. The IPT power controller will be discussed in two major sections which are multi-power level resonant frequency-based power controller design and switching logic design.

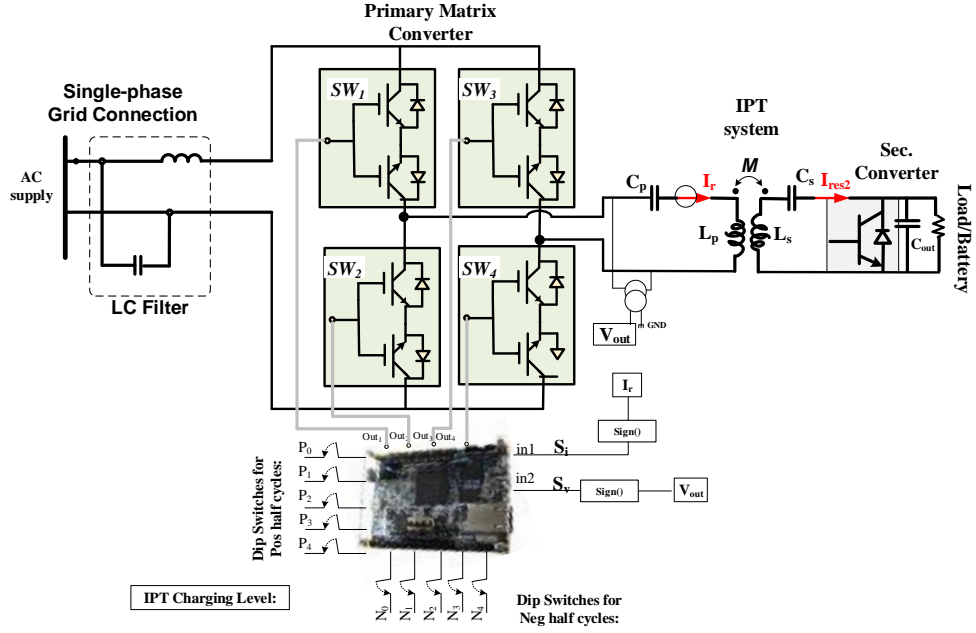


Figure 8.1: Conceptual Picture: AC-AC Matrix Converter and IPT system

8.2.1 Resonant Frequency-based Power controller Design

In this section, the controller is designed to adjust the charging level of IPT system over the control frequency which is considered sixteen times of the IPT resonant frequency ($f_{ctr} = 16 \times f_{res}$). As can be seen from Fig.8.1, using the four dip switches for negative half cycles (N_i), the frequency of $\overline{S_i}$ can be divided down by $\frac{k}{16}$ factors ($k = 1, 2, \dots, 16$). On the other hand, the four dip switches for positive half cycles (P_i) are defined as bits to divide frequency of the signed resonant current (S_i) in positive half cycles. It is worthy of note that in the digital controller which will be discussed later, S_i is defined the same as clk_{in} .

The algorithms ?? and ?? are written in VHDL script version (referring to the appendix), count2(i), count22(i), count3(i) and count33 are signals with size of 4-bit length that are synthesized using clk_{in} , $\overline{clk_{in}}$, $count0$, $\overline{count0}$, $count1$ and $\overline{count1}$ ($\forall i \in [0 \dots 3]$). Where, clk_{in} , $count0$, and $count1$ are the sign of resonant current, count number of negative half cycles and count number of positive half cycles respectively. The simulation is carried out using Modelsim and Quartus Prime Lite Edition, and the signals are as shown in Fig. 8.2.

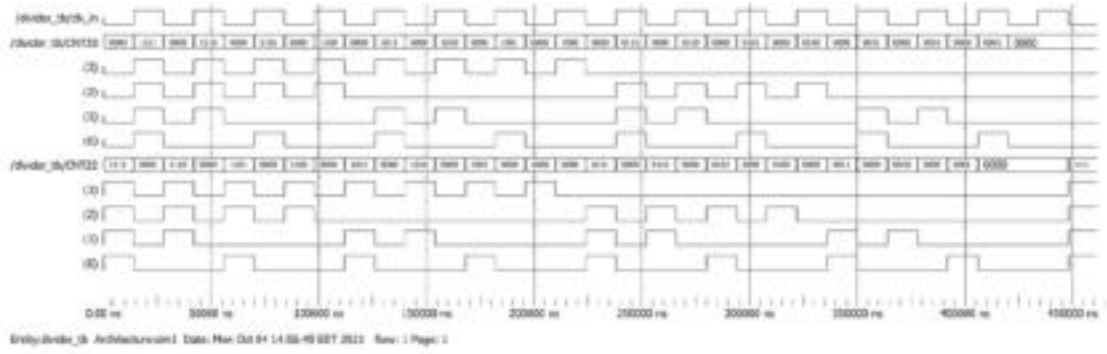


Figure 8.2: The simulation results for the signals $count2(i)$, $count22$, $count3$ and $count33$

By applying the AND, OR, and NOT Boolean logic operations on the obtained $count2(i)$, $count22(i)$, $count3(i)$ and $count33$, various number of pulses from one to 16 pulses for either positive and negative half cycles of clk_{in} are synthesized.

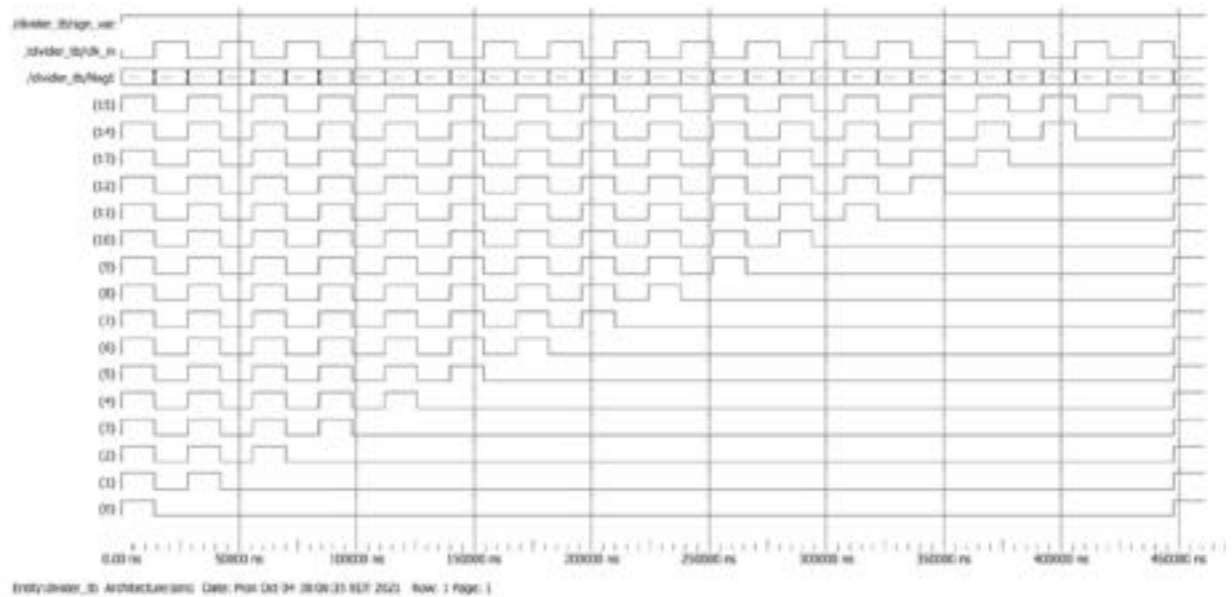


Figure 8.3: $Count4(t)$ ($\forall t \in [0 \dots 15]$) which contains $t + 1$ pulses in negative half cycles

Signals $count4(t)$ and $count5(k)$ ($\forall t, k \in [0 \dots 15]$) are synthesized in such a way that extract $L_{neg} = t + 1$ and $L_{pos} = k + 1$ number of pulses in either positive or negative half cycles. As can be seen from Figs. 8.3 and 8.4, $count4(t)$ and $count5(k)$ are 16-bit length signals which contain varying pulse number from 1 to 16 pulses in either negative half cycles of CLK or positive half cycles. As an

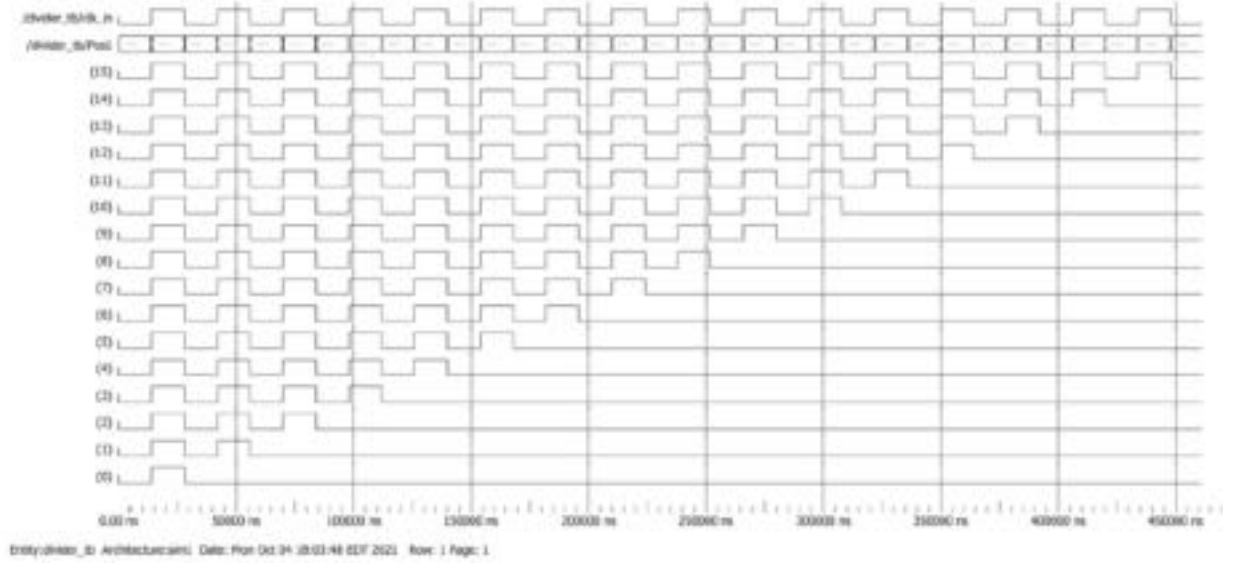


Figure 8.4: Count5(k) ($k = 0$ to 15) which contains the (k+1) pulses in positive half cycles

example, $count4(6)$ and $count5(6)$ keep 7 pulses out entire 16 pulses in clk_{in} and $\overline{clk_{in}}$ respectively, and eliminate the remaining pulses as illustrated in Figs. 8.3 and 8.4 respectively.

Table 8.1: Switching states based on signed voltage and signed current signals, and zero active modes

Mode	Type	S_{inj}	$S_v(V_{AC} > 0)$	$S_c(i_{res} > 0)$	SW1	SW2	SW3	SW4
1	Injection	1	1	1	count5(t)	0	0	count5(t)
2	Injection	1	1	0	0	count4(t)	count4(t)	0
3	Injection	1	0	1	0	count5(t)	count5(t)	0
4	Injection	1	0	0	count4(t)	1	1	count4(t)
5	zero Injection.	0	-	1	1	0	1	0
6	zero Injection.	0	-	0	0	1	0	1

8.2.2 Switching logic

The switching logic is defined to allow power flow from the grid to the vehicle (S_{inj}). As can be seen from Table.8.1, there are six possible operation modes; among them, four are power injection modes and two are zero injection (free oscillation) modes. Power flow direction in the four energy injections is set to be from Grid to Vehicle (G2V). Therefore, the output voltage and resonant current signs will be same (both signs will always be either positive or negative). As it can

be seen from the table 8.1 and Fig.8.5, when the voltage is positive and the current sign is high; or when the voltage is negative and the current sign in low, then the switches SW1 and SW4 conduct, and the switching gate signals of SW1 and SW4 are assigned on either $count5(k)$ or $count4(t)$ signals respectively. The charging level in positive half cycles (L_{pos}) and negative half cycles (L_{neg}) are specified based on values of dip switches P_i and N_i which are defined as the power level selectors in the FPGA Pinout.

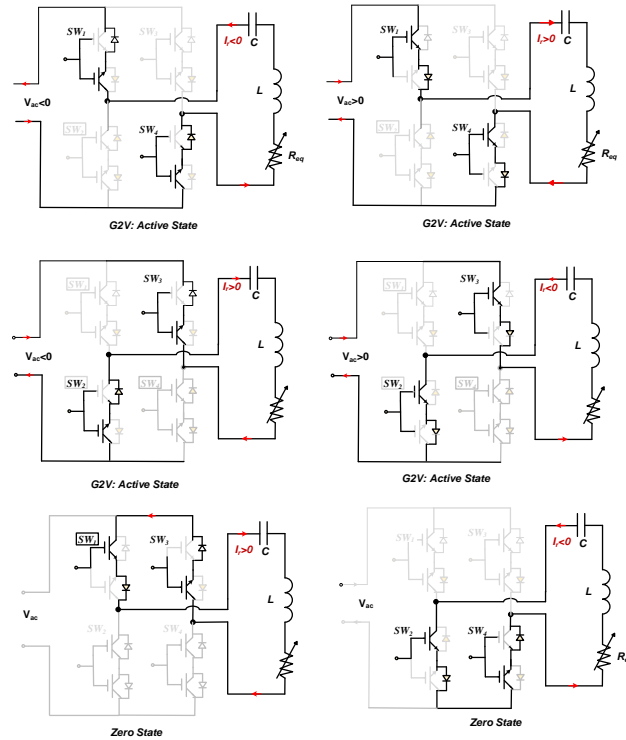


Figure 8.5: Equivalent circuit operations with active and zero states for Grid to Vehicle operational mode

On the other hand, when the voltage is negative and the current is in its positive half cycle or when the voltage is positive and the current sign in negative, then the switches SW2 and SW3 conduct, and, the switches SW1 and SW4 conduct, and the switching gate signals of SW2 and SW3 depending on the resonant current direction are assigned on either $count5(k)$ or $count4(t)$ signals respectively. However, in zero switching states, the converter output voltage is set to zero (shorted). This means that, in positive half cycles upper switches which are SW1 and SW3

conducts and for negative half cycles bottom switches (SW2 and SW4) conduct; and the switching gate signals depending on the resonant current direction are assigned on either CLK or \overline{CLK} signals respectively.

8.3 Power and Voltage Calculation using Fundamental Harmonic Analysis

To calculate the power transfer rates in different mentioned levels, Fundamental Harmonic Approximation (FHA) method is used. Applying the FHA method, the fundamental component of converter's voltage is derived at the resonance frequency ω as follows (equation (8.1)):

$$V_{Conv}^1 = \frac{\omega}{16\pi} \int_0^{\frac{32\pi}{\omega}} V_{Conv}^{out} \sin(\omega t) dt \quad (8.1)$$

where V_{Conv}^{out} is the output voltage of the primary AC/AC converter, ω is the resonance frequency, and V_1^{conv} is the converter's fundamental harmonic component. Considering L_{pos} and L_{neg} as energy injection signals in negative and positive half-cycles of resonant current respectively; the output voltage can be rewritten in a discrete way as shown in Eqs. (8.2) and (8.3) when either input AC voltage is in positive or negative half cycles:

$$V_{Conv}^{out} = \begin{cases} +V_{AC} & \frac{2(j-1)\pi}{\omega} < t < \frac{(2j-1)\pi}{\omega}, j = 1, \dots, L_P \\ -V_{AC} & \frac{(2i-1)\pi}{\omega} < t < \frac{2i\pi}{\omega}, j = 1, \dots, L_N \\ V_{AC} > 0 & \\ 0 & \text{otherwise} \end{cases} \quad (8.2)$$

$$V_{Conv}^{out} = \begin{cases} -V_{AC} & \frac{2(j-1)\pi}{\omega} < t < \frac{(2j-1)\pi}{\omega}, j = 1, \dots, L_P \\ +V_{AC} & \frac{(2i-1)\pi}{\omega} < t < \frac{2i\pi}{\omega}, j = 1, \dots, L_N \\ V_{AC} < 0 & \\ 0 & \text{otherwise} \end{cases} \quad (8.3)$$

Where V_{AC} is the input AC supply voltage, the L_{pos} and L_{neg} denote the energy injection pulse number in resonant current's positive or negative half cycle; And, the converter's output voltage V_{AC} are in all these active states. Since the resonant frequency (f_{res}) is extremely higher than the frequency of the input AC voltage ($f_{res}(90KHz) > f_{AC}(60Hz)$), therefore, input voltage magnitude (V_{AC}) over the control frequency ($f_{ctr} = 16 \times f_{res}$) can be considered constant. This means assuming the constant magnitude of input AC voltage in the first and second terms of Eqs. (8.2) and (8.3) is correct. Calculation of converter output voltage over the control frequency can be achieved based on either Eq. (8.2) or (8.3), and both give the same formulation; we have used Eq. (8.2) in this case.

As the third term of Eqs. (8.2) and (8.3), resonant converter operates in zero state which means that IPT operates in free-oscillation mode. By substituting Eq. (8.2) in (8.1) and expanding it, equation 8.4 can be achieved:

$$V_{Conv}^1 = \frac{\omega}{16\pi} \left(\sum_{j=1}^{L_{pos}} \int_{\frac{2(j-1)\pi}{\omega}}^{\frac{(2j-1)\pi}{\omega}} V_{AC} \sin(\omega t) dt + \sum_{i=1}^{L_{neg}} \int_{\frac{(2i-1)\pi}{\omega}}^{\frac{2i\pi}{\omega}} -V_{AC} \sin(\omega t) dt \right) \quad (8.4)$$

Equation (8.4) can be simplified to equation (8.5) as follows:

$$V_{Conv}^1 = \frac{(L_{pos} + L_{neg})V_{AC}}{8\pi} \quad (8.5)$$

As defined earlier, $D = (L_{pos} + L_{neg})/32$ can be substituted in equation (8.5) and simplify it as expressed in equation (8.6).

$$V_{Conv}^1 = \frac{4}{\pi} D V_{AC} \quad (8.6)$$

To calculate power transfer rate for this system, the fundamental harmonic of primary resonant current is calculated using equation (8.5) and expressed in equation (8.7):

$$I_{pr} = \frac{V_{Conv}^1}{R_{eq}} = \frac{(L_{pos} + L_{neg})V_{AC}}{4\pi R_{eq}} \quad (8.7)$$

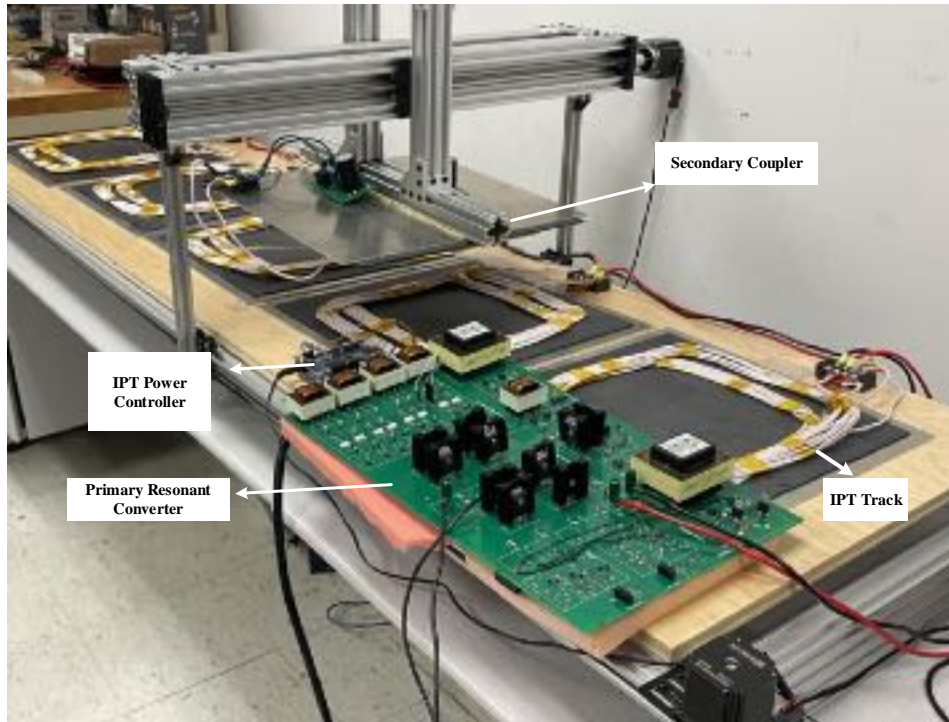


Figure 8.6: Dynamic IPT setup comprised of 5 bipolar transmitting couplers and a receiver

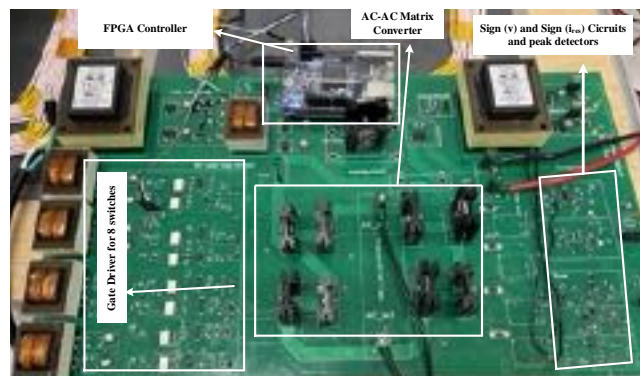


Figure 8.7: Resonant high frequency converter with FPGA-based IPT power controller

Table 8.2: Technical specification of IPT system Set up

Parameter	Value
Gap distance	200 mm
transmitter pad diameter	352 mm
Primary and Secondary Compensation capacitors (C_p, C_s)	82 nF
Primary/Secondary self inductance (L_{pos}, L_s)	38.3 μ H
AC Input voltage (V_{ac})	120 V
Input AC frequency (f_{ac})	60 Hz
IPT designed resonance frequency (f_r)	90 kHz

where R_{eq} (shown in Fig. 8.5) is the equivalent resistance reflected to the primary, because at resonant frequency, the secondary series compensation capacitor and secondary inductance cancels out each other. Then the output power can be presented as,

$$P = \frac{1}{2} R_{eq} I_{pr}^2 = \frac{(L_{pos} + L_{neg})^2 V_{AC}^2}{32\pi^2 R_{eq}} \quad (8.8)$$

As it can be seen from Eq. (8.8), and L_{neg} the L_{pos} as the energy injection pulses have direct relation to power transfer rate. As can be seen from 3d plot shown in Fig.8.8, the output power is in its maximum when the total energy injection is 32 ($L_{pos} = 16$ and $L_{neg} = 16$). Additionally, the power transfer is also dependent of load, and can be varied with load change, this means the proposed adjustable charging level can be of great functionality to keep the the power transfer rate fixed under load variation.

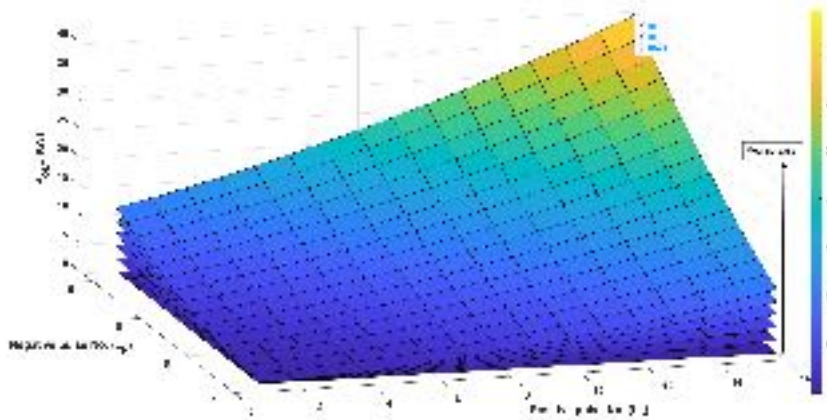
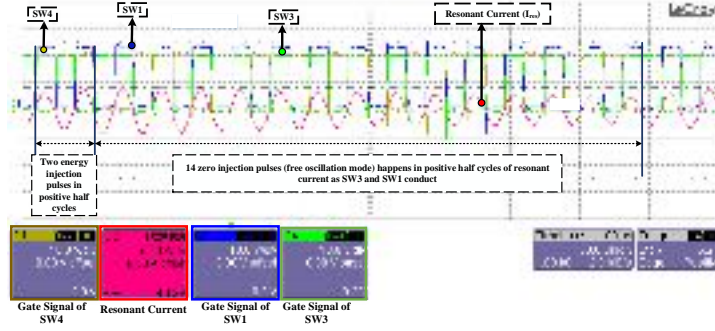
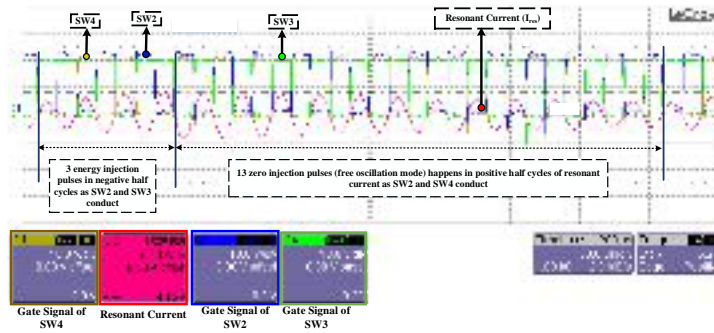


Figure 8.8: 3-d plot: output power vs energy injection in positive half cycle(L_{pos}) vs energy injection in positive half cycle(L_{neg})



(a)

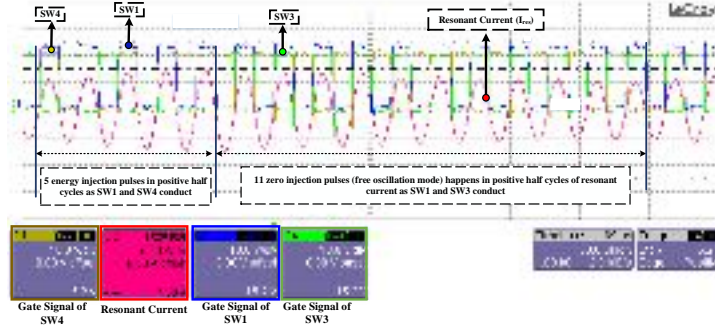


(b)

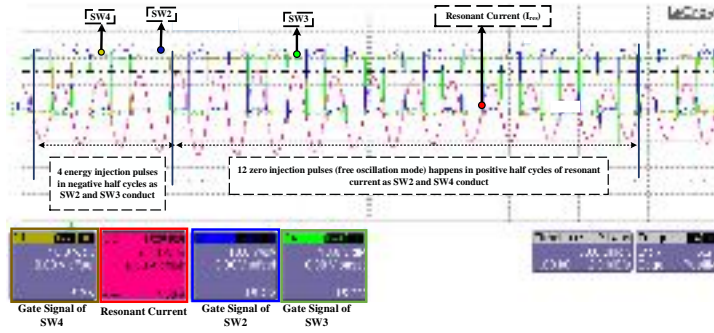
Figure 8.9: Switching signals when the multi-power level controller is set to operate in total level of 5 ($L_{neg} = 3$ and $L_{pos} = 2$) (a) Dip switches for power level selector for positive are set $P_3P_2P_1P_0 = "0001"$ (b) Dip switches for power level selector for negative are set $N_3N_2N_1N_0 = "0010"$

8.4 Experimental Validation for the multi-power level controller with Zero states

This setup is also equipped with two different DC motors which can move the secondary all across the IPT track, and further DC Motor is installed in the receiver side which produces lateral misalignment system (referring to the Fig.8.6). As shown using labels in the Fig.8.7, the PCB board is comprised of AC-AC high frequency converter, FPGA-based IPT power controller, gate drive circuit, peak detector circuit, and $sign()$ circuits. Experimental results are achieved for different values of power selectors (N_i and P_i) - which in total can adjust from 0 (no charge mode) to 32 (full charging level) - to verify the power regulation capability of the



(a)

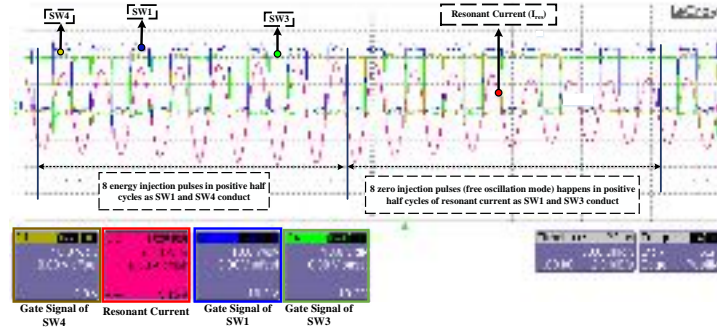


(b)

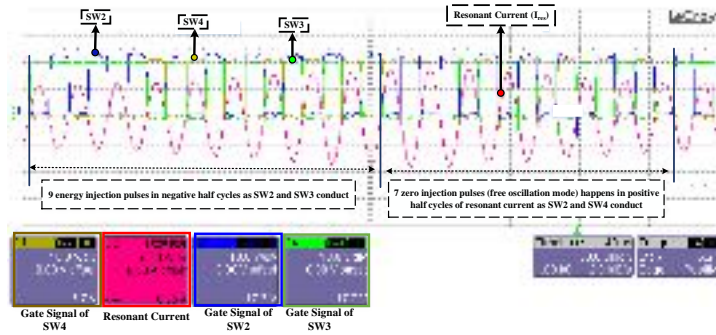
Figure 8.10: Power level controller is set to operate in total level of 9 ($L_{neg} = 5$ and $L_{pos} = 4$) (a)Power level selector for positive are set $P_3P_2P_1P_0 = "0101"$ (b)Power level selector for negative are set $N_3N_2N_1N_0 = "0100"$

proposed IPT power level controller.

In the Fig.8.9, the IPT charging level is set at 5 by considering 3 energy injection in negative half cycles, and 2 energy injection at positive half cycles ($L_{neg} = 3$ and $L_{pos} = 2$). For this mean, the dip switches defined as power level selectors are set as follows: $P_3P_2P_1P_0 = "0001"$ and $N_3N_2N_1N_0 = "0010"$. As can be seen from Fig. 8.9a, two energy injections happen during positive half cycles; accordingly, the Switches SW1 and SW4 conduct, while in the remaining 14 half cycles of the control frequency ($f_{ctr} = 16 \times f_{res}$), the free-oscillation (non injection) happen and the Switches SW1 and SW3 conduct. Moreover, referring to the Fig. 8.9b, three energy injections happen during negative half cycles; accordingly, the Switches SW2 and SW3 conduct, and 13 free-oscillation (non injection) happen during the remaining half cycles of control frequency, and Switches SW2 and SW4



(a)

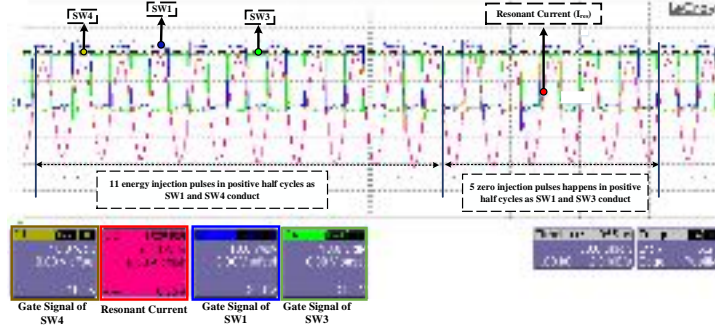


(b)

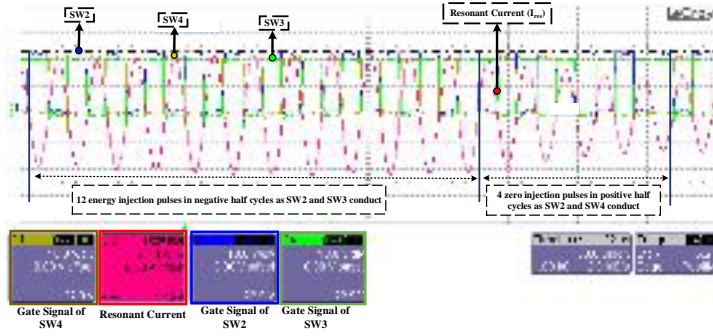
Figure 8.11: Power level controller is set to operate in total level of 17 ($L_{neg} = 8$ and $L_{pos} = 9$) (a) Power level selector for positive are set $P_3P_2P_1P_0 = "0111"$ (b) Power level selector for negative are set $N_3N_2N_1N_0 = "1000"$

conduct. It is evident from Figs.8.9a and 8.9b that during energy injection time intervals, the resonant current magnitude increases and reaches up to the peak value of 4.15A and during the zero injection time interval, the current magnitude start decreasing.

In the Fig.8.10, the IPT charging level is set at 9 by considering 5 energy injection in negative half cycles, and 4 energy injection at positive half cycles ($L_{neg} = 5$ and $L_{pos} = 4$).For this mean, the power level selectors are set as follows: $P_3P_2P_1P_0 = "0101"$ and $N_3N_2N_1N_0 = "0100"$. As can be seen from Fig. 8.10a, 4 energy injections happen during positive half cycles; accordingly, the switches SW1 and SW4 conduct, and 12 free-oscillation (non injection) happen in the remaining half cycles of control frequency; and the switches SW1 and SW3 conduct. According to the Fig. 8.10b, five energy injections happen during negative half cycles; and



(a)



(b)

Figure 8.12: Power level controller is set at 23 ($L_{neg} = 11$ and $L_{pos} = 12$) (a) Power level selector for positive are set $P_3P_2P_1P_0 = "1010"$ (b) Power level selector for negative are set $N_3N_2N_1N_0 = "1011"$

the switches SW2 and SW3 conduct. Moreover, 11 free oscillation pulses (non injection) happen during the rest of control cycle; and the switches SW2 and SW4 conduct. Again, it is evident that over the the resonant current magnitude increases during injection time, and reaches up to 7.6 A , however, it decreases during the free oscillation time interval.

In the Fig.8.11, the IPT charging level is set at 17 by considering 8 energy injection in negative half cycles, and 9 energy injection at positive half cycles ($L_{neg} = 8$ and $L_{pos} = 9$). For this mean, the power level selectors are set as follows: $P_3P_2P_1P_0 = "0111"$ and $N_3N_2N_1N_0 = "1000"$. As can be seen from Figs. 8.13a and 8.13b, 8 energy injections happen during positive half cycles, and 9 energy injections happen during negative half cycles respectively. And, the resonant current magnitude increases up to 8.85 A.

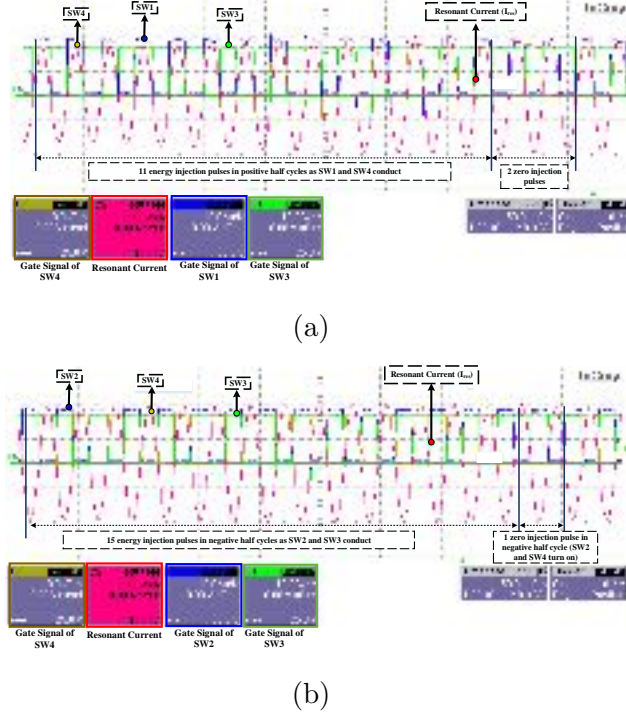
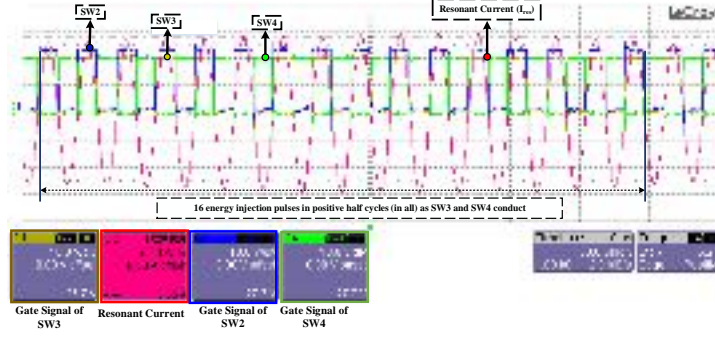


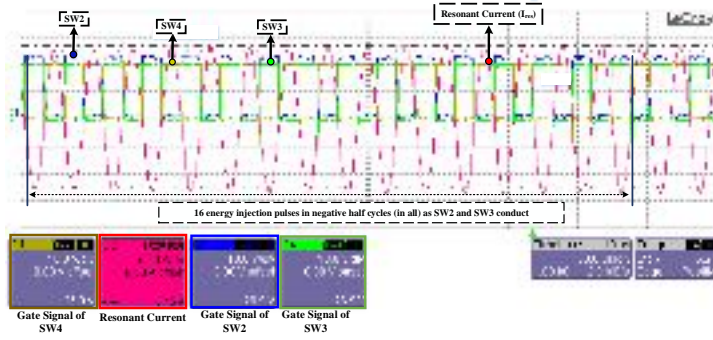
Figure 8.13: Power level controller is set at 29 ($L_{neg} = 14$ and $L_{pos} = 15$) (a) Power level selector for positive are set $P_3P_2P_1P_0 = "1101"$ (b) Power level selector for negative are set $N_3N_2N_1N_0 = "1110"$

As another experimental test, the IPT charging level is set at 23 by setting the negative energy injection at eleven, and positive energy injection at 12 ($L_{neg} = 11$ and $L_{pos} = 12$). Accordingly, the power level selectors are set as follows: $P_3P_2P_1P_0 = "1010"$ and $N_3N_2N_1N_0 = "1011"$. As can be seen from Figs. 8.12a and 8.12b, 11 energy injections happen during positive half cycles, and 12 energy injections happen during negative half cycles respectively. And, the resonant current magnitude increases up to 11.45 A.

In the Fig.8.13, the IPT charging level is set at 29 by considering 14 positive energy injection pulses, and 15 negative energy injection pulses by assigning the power level selectors on $P_3P_2P_1P_0 = "1101"$ and $N_3N_2N_1N_0 = "1110"$. The result obtained as shown in Figs. 8.13a and 8.13b verify the accurate performance of the proposed controller. And, the peak resonant current magnitude has increased up to 12.5 A. As the final experiment regarding the performance validation of



(a)



(b)

Figure 8.14: Power level controller is set 32 ($L_{neg} = 16$ and $L_{pos} = 16$) (a) Power level selector for positive are set $P_3P_2P_1P_0 = "1111"$ (b) Power level selector for negative are set $N_3N_2N_1N_0 = "1111"$

the proposed controller, the IPT charging level is set at the maximum charging level(32) by considering 16 positive energy injection pulses as well as 16 negative energy injection pulses ($L_{neg} = 16$ and $L_{pos} = 16$); this is applied by setting the defined input dip switches in the FPGA board at $P_3P_2P_1P_0 = "1111"$ and $N_3N_2N_1N_0 = "1111"$. As can be seen from the Figs. 8.14a and 8.14b, controller force the converter to operate only in active states over the all 32 half cycles control frequency. And, the resonant current magnitude increases up to 13.45 A.

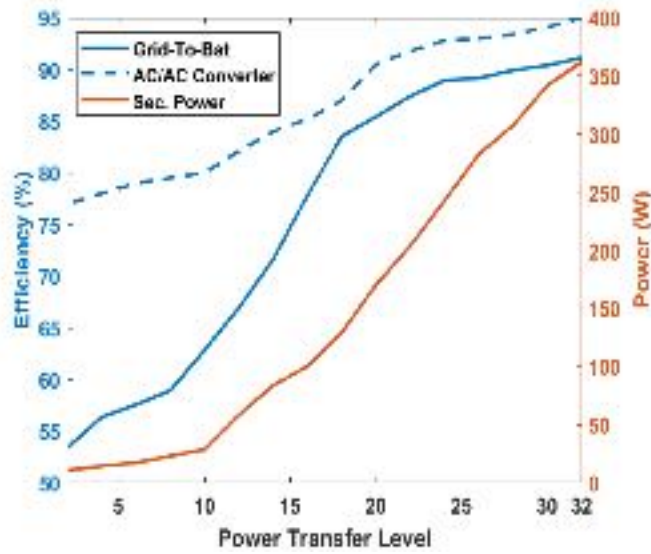


Figure 8.15: Efficiency plots at different power transfer levels

8.5 efficiency analysis of the proposed multi-power level IPT system

As explained, the primary converter is a single-stage matrix AC-AC converter connected to a 60-Hz single-phase supply controlled with the proposed multi-power level controller. And, in the receiver side, the diode rectifier is used for DC conversion. The Grid-to-Battery efficiency (η_{G2B}), the AC-AC resonant converter efficiency ($\eta_{Conv.}$) and rectified secondary power under various power transfer levels are shown in the same plot referring to Fig. 8.15. The experiments are carried out in low power range due to power supply limitation in the lab, however, it is expected to see higher efficiency if these are replicated in rated power for all power levels; the reason behind this is due to relatively lower switching loss, ferrite loss (eddy loss, proximity loss), and plate loss in high power range. As can be seen from Fig. 8.15, the η_{G2B} , $\eta_{Conv.}$, and the secondary rectified power (P_{rect}) increase as IPT's power transfer level increases, which reaches up to 91.135% at level=32. The low power efficiency of the charging system in lower charging level is because of the increased free oscillation counts, and decreased number of energy injections; in other words, free oscillation results in conduction loss as the resonant current flows through the short-circuited LC which increases loss.

8.6 summary

In this chapter, new multi-level IPT power controller is proposed which only uses current sensors to produce different power transfer level. Using Boolean operators (AND, OR, Not, ..), 16 power transfer levels for positive and 16 different power levels for negative half cycle of resonant current are designed; which in total can provide 32 different IPT power levels. Moreover, it was shown that creating dead-time between upper and bottom switches of the leg by turning off all the switches can cause unwanted reverse power. New switching logic is presented which not only solve the issue but also give more power control regulation capability for IPT systems. IPT power controller and switching logic are validated using simulation as well as experimental results.

CHAPTER 9

CONCLUSIONS AND FUTURE WORK

Inductive Power Transfer(IPT) systems have taken more attention recently due to its superior robustness, reliability and safety in comparison with the existing methods. This technology is applied widely as bio-medical implants, material handling, transportation systems. IPT charging applications are widespread in different range of power such as Electric Vehicles, scooter, electric aircraft, wheelchair and so on. This emerging technology has become marketable by different auto-manufacturers, which shows the pace of its advancement and progress. The researches has been concentrated on improving IPT systems' performance improvement in both static and dynamic operational modes. Most of the advancements of IPT systems have been carried out on power transfer level controller, optimal magnetic design of wireless charging stations for dynamic as well as stationary applications, resonant HF converter topologies, compensation configuration, design of various controller for addressing IPT related issues, and impedance network matching strategies. In this dissertation, many of above mentioned aspects of IPT systems for EV charging application are thoroughly discussed, evaluated and correspondingly controllers proposed.

In chapter second, a sensoreless technique based on resonance frequency deviation is introduced to detect conductive foreign objects in charging areas. The proposed method can be implemented on self-tuning controllers that use the IPT-system resonance frequency for switching frequency generation, therefore, this eliminates any need for extra sensors or structures. The FOD method can be applied either in low-power mode (standby) or in operational mode. Furthermore, the primary resonance current is introduced as the complementary signal to address the proposed FOD method's weakness to distinguish between the smaller conductive objects and vehicle positional variation. It is shown that the primary resonance current increases more for a misalignment case than FOI. The proposed FOD method is

applied on the IPT system to detect a 5-cent coin and a beverage can, and the results have shown that the FOD method is fast in detection of larger conductive objects (as tested on the beverage can) than smaller size conductive objects (as tested on the 5-cent coin). Experimental tests have further shown that the lower the detection speed, the greater the detection area, as a result, the smaller foreign objects detection can be realized. Also, a couple of experimental verification is done for discrimination of FOI from misalignment for a wide range of overlapping resonant frequencies, and the results have shown that the primary resonant current deviation is an effective way to differentiate these two scenarios.

In chapter three, the power-frequency model is used to implement VIC in IPT systems. An IPT multi-power level controller is designed using logic circuit gates which can produce 16-discretized power transfer levels in total. It is shown that VIC implemented via the firmware programming on microcontroller provides the appropriate power transfer level in a real time manner based on the grid frequency fluctuation. The IPT multi-power level controller accordingly regulates the quantum number of energy injection based on the power level set by the VIC. This allows the IPT EV system to appear as a high inertia load to the grid. Experimental results derived in an actual small-scale power grid(LabVolt system) verified that when frequency either increases or decreases, the proposed VIC sets IPT system either on higher or lower level respectively. The main advantages of the proposed are as follows: 1) Instead of user-defined power reference values, the IPT power reference is selected by VIC; contributing to grid stabilization 2) Simplicity and ease of implementation of multi-power level controller 3) the primary high frequency converter benefits from resonance frequency tracking capability due to the synchronization of switching operations with the resonant current and 4) The proposed VI IPT controller benefits from soft-switching operations (both ZCS and ZVS).

In chapter four, a new switching technique for single stage AC-AC matrix converter is proposed. Unlike conventional carrier-based PWM techniques, it employs predetermined switching vector to eliminate unnecessary switching such as shoot-through, and reduce THD as well as conduction loss. The proposed method improves the performance of IPT system in power regulation by adjusting the conduction angle in active state. This method modulates the power transfer level over a constant switching frequency when there is no load variation or misalignment, furthermore, it can always provide resonance condition in IPT system as the switching frequency is synchronized with resonant current. A simulation study carried out clearly showed the self-tuned performance of the proposed converter in tracking the IPT power reference.

In chapter five, an online parameter estimation method that can simultaneously determine the magnetic coupling coefficient and the load at the secondary has been introduced. The proposed method is developed based on the analytical formulations for the magnetic coupling, battery charging current and battery voltage that are expressed in terms of primary side measurements and system specifications. The proposed method is simulated and experimentally validated and the results are presented. The simulation and experimental results verify that the proposed method can accurately estimate the magnetic coupling factor, secondary battery charging current and voltage in inductive charging systems simultaneously in real-time. The developed method can find immediate applications for the development of adaptive controllers for static and dynamic inductive charging systems.

In chapter six, the 3D-FEA model of DD and BPP coupler (being the most effective topologies) for dynamic IPT EV chargers is thoroughly investigated. It was shown that BPP power pads outperform DD power pads in all respects such as electromagnetic compliance, better misalignment tolerance performance, higher coupling factor, and greater power transfer capability.

In chapter seven, a multi-objective optimization algorithm to find the optimal geometries of BPP coupler is proposed and implemented. The parametric opti-

mal design of BPP is carried out through scripting in MATLAB interfaced with FEMM software. In each iteration of NSGA-II algorithm for all generation of variables, the corresponding 2D-FEA model is created in FEMM software; the loss, and tolerance as objective functions are evaluated correspondingly. For practical feasibility, the cost of each design is also considered as another objective function in the MOOP. Finally, 15 Pareto optimal solutions were achieved for 10kW IPT system used as a case study. Two of the Pareto optimal solutions were further analyzed to validate the proposed algorithm. The achieved optimal solutions gives the designer a wide range of optimization results for IPT EV application . As a future work, the IPT roadway powered track will be constructed for dynamic EV application following "PFS-6" geometries.

In chapter eight, new multi-level IPT power controller is proposed which only uses current sensors to produce different power transfer level. Using Boolean operators(AND,OR,Not,..), 16 power transfer levels for positive and 16 different power levels for negative half cycle of resonant current are designed; which in total can provide 32 different IPT power levels. Moreover, it was shown that creating dead-time between upper and bottom switches of the leg by turning off all the switches can cause unwanted reverse power. New switching logic is presented which not only solve the issue but also give more power control regulation capability for IPT systems. IPT power controller and switching logic are validated using simulation as well as experimental results.

9.1 Future Works

- **Power Transfer Capability Improvement of IPT System using Adjustable Inductor.**

The coupling coefficient of the power pads and load conditions are sensitive to changes in the environment, component aging and temperature drifts, which dramatically decrease the power transfer capabilities of the system.

Reducing the sensitivity of the WPT system to variations can be alleviated by designing matching networks that provide loose coupling between the transmitting and receiving sides. To improve power transfer of IPT system, recent research studies has introduced different methods which are frequency tuning, compensation networks impedance matching, and post regulation DC-DC conversion [147–152]. Utilizing frequency tracking method to minimize the dependency of the IPT system to distance, misalignment and load variations has been discussed in this dissertation for power transfer regulation. However, the frequency tracking method can only be practical for small ranges, as the allowed frequency range is narrow. The future work is to place adjustable inductor in both primary and secondary with a control that guarantee the phase difference of 90 degree phase shift between the compensation tank voltage and primary or secondary voltage. This 90 phase shift using the adjustable inductor can provide continuous tuning of the operating frequency to the resonant one, and adjusts both the transmitter’s and receiver’s matching networks such that the best power transfer conditions are obtained for any given combination of distance, displacement misalignment or component values.

- **Bidirectional DC-DC converter design for secondary side of IPT EV charging station**

The secondary rectified voltage in IPT systems has very wide range of variation depending on the compensation topology employed (parallel-parallel , series-series, parallel-series, series-parallel, LCC-parallel, LCC-LCC,). Additionally, the power transfer direction can be either V2G or G2V. Therefore, design of bidirectional DC-DC converter to step down the highly variable DC level to battery requirement is new challenge.

- **Self-tuned IPT power Controller using estimated parameters of secondary side** The online estimation method of IPT secondary side pa-

parameters using primary side measurements is proposed in this dissertation, this method can estimate charging current and voltage, and the coupling factor only using the primary resonant current, primary compensation voltage and primary input voltage. The application of this estimation method for online adjustment of power level can be of great use in IPT system. As future work, the estimated parameters can be used for power reference generation in the existing IPT power controller, this can help to regulate power level with respect to the estimated parameters. Especially, the proposed IPT power level controller using the estimated parameters of secondary can be a great functionality in dynamic IPT application as the coupling varies constantly.

- **Power Factor Correction converter Topologies in IPT EV Battery charger**

Corporation of electric vehicle (EV) to the recent transportation may persuade adverse impacts on overall power quality. The power quality situation can be even worsen in case of inductive IPT chargers, therefore, the power factor correction converter has become vital to the researchers due to presence of electromagnetic interference noise with high frequency content in wireless EV charging stations. Basic power factor correction converters are mainly boost, interleaved boost, buck-boost which allow wide range of load and line variation, however, they all suffer from considerable conduction loss. Therefore, the proposed future work for PFC stage converter in IPT systems is non-isolated bridgeless DC-DC converter such as Cuk and SEPIC (Single Ended Primary Inductor Converter).

- **Control Method to Minimize the Negative Inter Coupling of Transmitters in IPT track in Dynamic Application**

The IPT track made up of several lumped discrete transmitting couplers suffers from cross coupling between couplers; as the equivalent mutual in-

ductance could make the IPT system to operate in the detuned condition as pickup is moving across the track. As the future work, a comprehensive design of compensation tank considering the self coupling of transmitting coupler can improve power transfer capability all over the track.

- **Living Object Detection Methods in IPT Systems by Detection of the Capacitance Between the Transmitter Structure and Ground**

In this dissertation, metal object detection based on resonant frequency deviation is proposed and evaluated. Using FEA analysis, it was shown that metal object intruded into the IPT system can cause significant change in the primary self-inductance and accordingly in the resonant frequency. However, the resonant frequency tracking method can be effective for detection of living object intrusion. As future work, another method based on the estimation of equivalent capacitance between transmitter and receiver magnetic structures should be utilized. The reason for this incidence is the high amounts of water inside the living bodies which will affect the electric field distribution once intruded into power transfer area. In the proposed method, the equivalent capacitance of primary pad with respect to the ground - mainly impacted by living object intrusion- is used as part of a circuit to synthesize a pulse wave. Since the equivalent capacitance change can cause frequency change of the pulse wave, therefore, the proposed detection method can work for any kind of objection intrusion with any properties.

REFERENCE

- [1] G. A. Covic and J. T. Boys, “Modern trends in inductive power transfer for transportation applications,” *IEEE Journal of Emerging and Selected Topics in Power Electronics*, vol. 1, no. 1, pp. 28–41, March 2013.
- [2] D. Patil, M. K. McDonough, J. M. Miller, B. Fahimi, and P. T. Balsara, “Wireless power transfer for vehicular applications: Overview and challenges,” *IEEE Transactions on Transportation Electrification*, vol. 4, no. 1, pp. 3–37, March 2018.
- [3] C. Panchal, S. Stegen, and J. Lu, “Review of static and dynamic wireless electric vehicle charging system,” *Engineering Science and Technology, an International Journal*, vol. 21, 06 2018.
- [4] F. Lu, H. Zhang, H. Hofmann, and C. Mi, “An inductive and capacitive combined wireless power transfer system with lc-compensated topology,” *IEEE Transactions on Power Electronics*, vol. 31, pp. 1–1, 12 2016.
- [5] P. Venugopal and P. Bauer, “Distributed ipt systems for dynamic powering–misalignment analysis,” *IEEE Transactions on Industrial Electronics*, 12 2014.
- [6] J. Miller, O. Onar, C. White, S. Campbell, C. Coomer, L. Seiber, R. Sepe, and A. Steyerl, “Demonstrating dynamic wireless charging of an electric vehicle: The benefit of electrochemical capacitor smoothing,” *Power Electronics Magazine, IEEE*, vol. 1, pp. 12–24, 03 2014.
- [7] O. Onar, J. Miller, S. Campbell, C. Coomer, C. White, and L. Seiber, “A novel wireless power transfer for in-motion ev/phev charging,” 03 2013, pp. 3073–3080.

- [8] F. Lu, H. Zhang, H. Hofmann, and C. Mi, “A dynamic charging system with reduced output power pulsation for electric vehicles,” *IEEE Transactions on Industrial Electronics*, vol. 63, pp. 1–1, 10 2016.
- [9] Z. U. Zahid, Z. M. Dalala, C. Zheng, R. Chen, W. E. Faraci, J. S. J. Lai, G. Lisi, and D. Anderson, “Modeling and control of series-series compensated inductive power transfer system,” *IEEE Journal of Emerging and Selected Topics in Power Electronics*, vol. 3, no. 1, pp. 111–123, March 2015.
- [10] International Energy Agency, “Global EV outlook 2018: towards cross-model electrification,” *Electric Vehicles Initiative*, p. 143, 2018.
- [11] C.-S. Wang, O. H. Stielau, and G. A. Covic, “Design considerations for a contactless electric vehicle battery charger,” *IEEE Trans. Ind. Electron.*, vol. 52, no. 5, pp. 1308–1314, Oct 2005.
- [12] S. Lukic and Z. Pantic, “Cutting the cord: Static and dynamic inductive wireless charging of electric vehicles,” *IEEE Electrification Magazine*, vol. 1, no. 1, pp. 57–64, Sep. 2013.
- [13] J. P. K. Sampath, D. M. Vilathgamuwa, and A. Alphones, “Efficiency enhancement for dynamic wireless power transfer system with segmented transmitter array,” *IEEE Transactions on Transportation Electrification*, vol. 2, no. 1, pp. 76–85, March 2016.
- [14] K. L. Hall, M. P. Kesler, R. Fiorello, D. A. Schatz, K. J. Kulikowski, and M. Soljacic, “Vehicle charger safety system and method,” Mar. 31 2011, uS Patent App. 12/899,281.
- [15] S. Y. Jeong, V. X. Thai, J. H. Park, and C. T. Rim, “Self-inductance-based metal object detection with mistuned resonant circuits and nullifying induced voltage for wireless ev chargers,” *IEEE Transactions on Power Electronics*, vol. 34, no. 1, pp. 748–758, Jan 2019.

- [16] H. Jafari, M. Mahmoudi, A. Fatehi, M. H. Naderi, and E. Kaya, "Improved power sharing with a back-to-back converter and state-feedback control in a utility-connected microgrid," in *2018 IEEE Texas Power and Energy Conference (TPEC)*, Feb 2018, pp. 1–6.
- [17] M. Mahmoudi, A. Fatehi, H. Jafari, and E. Karimi, "Multi-objective micro-grid design by nsga-ii considering both islanded and grid-connected modes," in *2018 IEEE Texas Power and Energy Conference (TPEC)*, Feb 2018, pp. 1–6.
- [18] H. Jafari, M. Mahmodi, and H. Rastegar, "Frequency control of micro-grid in autonomous mode using model predictive control," in *Iranian Conference on Smart Grids*, May 2012, pp. 1–5.
- [19] M. Mahmoudi, H. Jafari, and R. Jafari, "Frequency control of micro-grid using state feedback with integral control," in *2015 20th Conference on Electrical Power Distribution Networks Conference (EPDC)*, April 2015, pp. 1–6.
- [20] M. Amini and M. Almassalkhi, "Trading off robustness and performance in receding horizon control with uncertain energy resources," in *2018 Power Systems Computation Conference (PSCC)*, June 2018, pp. 1–7.
- [21] M. Moghaddami and A. I. Sarwat, "A Sensorless Conductive Foreign Object Detection for Inductive Electric Vehicle Charging Systems Based on Resonance Frequency Deviation," *2018 IEEE Industry Applications Society Annual Meeting (IAS)*, pp. 6–11, 2018.
- [22] M. Moghaddami and A. Sarwat, "Time-Dependent Multi-Physics Analysis of Inductive Power Transfer Systems," *2018 IEEE Transportation and Electrification Conference and Expo, ITEC 2018*, pp. 280–285, 2018.

- [23] W. H. Von Novak, P. Monat, and E. Kallal, “Wireless power system with capacitive proximity sensing,” Oct. 6 2015, uS Patent 9,154,189.
- [24] M. R. Sonapreetha, S. Y. Jeong, S. Y. Choi, and C. T. Rim, “Dual-purpose non-overlapped coil sets as foreign object and vehicle location detections for wireless stationary ev chargers,” in *2015 IEEE PELS Workshop on Emerging Technologies: Wireless Power (2015 WoW)*, June 2015, pp. 1–7.
- [25] N. Kuyvenhoven, C. Dean, J. Melton, J. Schwannecke, and A. E. Umenei, “Development of a foreign object detection and analysis method for wireless power systems,” in *2011 IEEE Symposium on Product Compliance Engineering Proceedings*, Oct 2011, pp. 1–6.
- [26] V. A. Muratov and E. G. Oettinger, “Systems and methods of wireless power transfer with interference detection,” Mar. 22 2016, uS Patent 9,294,153.
- [27] X. Liu, L. H. Swaans, K. W. P. Chan, H. K. Low, and W. K. Chan, “Methods and systems for detecting foreign objects in a wireless charging system,” Nov. 3 2015, uS Patent 9,178,361.
- [28] P. F. Hoffman, R. J. Boyer, and R. A. Henderson, “Foreign object detection system and method suitable for source resonator of wireless energy transfer system,” Apr. 5 2016, uS Patent 9,304,042.
- [29] S.-j. Huang, J.-l. Su, S.-h. Dai, C.-c. Tai, and T.-s. Lee, “Enhancement of Wireless Power Transmission with Foreign-Object Detection Considerations,” no. Gece, pp. 2–3, 2017.
- [30] J. Pávó, Z. Badics, S. Bilicz, and S. Gyimóthy, “Efficient perturbation method for computing two-port parameter changes due to foreign objects for wpt systems,” *IEEE Transactions on Magnetics*, vol. 54, no. 3, pp. 1–4, March 2018.

- [31] M. Moghaddami and A. I. Sarwat, "A sensorless conductive foreign object detection for inductive electric vehicle charging systems based on resonance frequency deviation," in *2018 IEEE Industry Applications Society Annual Meeting (IAS)*, Sep. 2018, pp. 1–6.
- [32] S. Lukic and Z. Pantic, "Cutting the cord: Static and dynamic inductive wireless charging of electric vehicles," *IEEE Electrific. Mag.*, vol. 1, no. 1, pp. 57–64, Sept 2013.
- [33] J. P. K. Sampath, D. M. Vilathgamuwa, and A. Alphones, "Efficiency enhancement for dynamic wireless power transfer system with segmented transmitter array," *IEEE Trans. Transport. Electrific.*, vol. 2, no. 1, pp. 76–85, March 2016.
- [34] J. M. Miller and A. Daga, "Elements of wireless power transfer essential to high power charging of heavy duty vehicles," *IEEE Trans. Transport. Electrific.*, vol. 1, no. 1, pp. 26–39, June 2015.
- [35] A. Zaheer, M. Neath, H. Z. Z. Beh, and G. A. Covic, "A dynamic ev charging system for slow moving traffic applications," *IEEE Trans. Transport. Electrific.*, vol. PP, no. 99, pp. 1–1, 2016, (early access).
- [36] G. R. Nagendra, G. A. Covic, and J. T. Boys, "Sizing of inductive power pads for dynamic charging of evs on ipt highways," *IEEE Trans. Transport. Electrific.*, vol. PP, no. 99, pp. 1–1, 2017, (early access).
- [37] J. Schneider, "Wireless power transfer for light-duty plug-in/ electric vehicles and alignment methodology," *SAE International J2954 Taskforce*, 2016.
- [38] J. P. C. Smeets, T. T. Overboom, J. W. Jansen, and E. A. Lomonova, "Inductance calculation nearby conducting material," *IEEE Trans. Magn.*, vol. 50, no. 11, pp. 1–4, Nov 2014.

- [39] S. Y. Hui, “Planar wireless charging technology for portable electronic products and qi,” *Proceedings of the IEEE*, vol. 101, no. 6, pp. 1290–1301, June 2013.
- [40] F. Turki, A. Körner, J. Tlatlik, and A. Brown, “Compact, safe and efficient wireless and inductive charging for plug-in hybrids and electric vehicles,” *SAE International Journal of Alternative Powertrains*, vol. 3, no. 2014-01-1892, pp. 139–151, 2014.
- [41] P. Hoffman, R. Boyer, and R. Henderson, “Foreign object detection system and method suitable for source resonator of wireless energy transfer system,” Apr. 5 2016, uS Patent 9,304,042. [Online]. Available: <https://www.google.com/patents/US9304042>
- [42] A. Roy, N. Katz, A. Kurs, C. Buenrostro, S. Verghese, M. Kesler, K. Hall, and H. Lou, “Foreign object detection in wireless energy transfer systems,” Aug. 2 2016, uS Patent 9,404,954. [Online]. Available: <https://www.google.com/patents/US9404954>
- [43] A. Karanth, K. Hara, and R. Kumar, “Foreign object detection in inductive coupled wireless power transfer environment using thermal sensors,” Jan. 12 2012, wO Patent App. PCT/EP2011/059,839. [Online]. Available: <https://www.google.com/patents/WO2012004092A2?cl=en>
- [44] Y. Bu, M. Nishiyama, T. Ueda, Y. Tashima, and T. Mizuno, “Examination of wireless power transfer combined with the utilization of distance detection,” *IEEE Trans. Magn.*, vol. 50, no. 11, pp. 1–4, Nov 2014.
- [45] S. Verghese, M. Kesler, K. Hall, and H. Lou, “Foreign object detection in wireless energy transfer systems,” Mar. 21 2013, uS Patent App. 13/608,956. [Online]. Available: <https://www.google.com/patents/US20130069441>

- [46] W. Von Novak, P. Monat, and E. Kallal, “Wireless power system with capacitive proximity sensing,” Oct. 6 2015, uS Patent 9,154,189. [Online]. Available: <https://www.google.com/patents/US9154189>
- [47] X. Liu, L. Swaans, K. Chan, H. Low, and W. Chan, “Methods and systems for detecting foreign objects in a wireless charging system,” Nov. 3 2015, uS Patent 9,178,361. [Online]. Available: <http://www.google.ch/patents/US9178361>
- [48] M. R. Sonapreetha, S. Y. Jeong, S. Y. Choi, and C. T. Rim, “Dual-purpose non-overlapped coil sets as foreign object and vehicle location detections for wireless stationary ev chargers,” in *2015 IEEE PELS Workshop on Emerging Technologies: Wireless Power (2015 WoW)*, June 2015, pp. 1–7.
- [49] N. Kuyvenhoven, C. Dean, J. Melton, J. Schwannecke, and A. E. Umenei, “Development of a foreign object detection and analysis method for wireless power systems,” in *Product Compliance Engineering (PSES), 2011 IEEE Symposium on*, Oct 2011, pp. 1–6.
- [50] V. Muratov and E. Oettinger, “Systems and methods of wireless power transfer with interference detection,” Mar. 22 2016, uS Patent 9,294,153. [Online]. Available: <https://www.google.com/patents/US9294153>
- [51] X. Dai and Y. Sun, “An accurate frequency tracking method based on short current detection for inductive power transfer system,” *IEEE Trans. Ind. Electron.*, vol. 61, no. 2, pp. 776–783, Feb 2014.
- [52] M. Moghaddami and A. Sarwat, “Single-phase soft-switched ac-ac matrix converter with power controller for bidirectional inductive power transfer systems,” *IEEE Trans. Ind. Appl.*, 2018, (in press).
- [53] M. Moghaddami, A. Cavada, and A. I. Sarwat, “Soft-switching self-tuning h-bridge converter for inductive power transfer systems,” in *2017 IEEE Energy Conversion Congress and Exposition (ECCE)*, Oct 2017, pp. 4388–4392.

- [54] M. Moghaddami and A. Sarwat, "Self-tuned single-phase ac-ac converter for bidirectional inductive power transfer systems," in *2017 IEEE Industry Applications Society Annual Meeting*, Oct 2017, pp. 1–6.
- [55] M. Moghaddami, H. Jafari, and A. Sarwat, "Virtual inertia control of inductive electric charging system using a power transfer controller," in *2019 IEEE Transportation Electrification Conference and Expo (ITEC)*, June 2019, pp. 1–6.
- [56] M. Lu and K. D. T. Ngo, "Systematic design of coils in series-series inductive power transfer for power transferability and efficiency," *IEEE Transactions on Power Electronics*, vol. 33, no. 4, pp. 3333–3345, 2018.
- [57] H. Zeng and F. Z. Peng, "Sic-based z-source resonant converter with constant frequency and load regulation for ev wireless charger," *IEEE Transactions on Power Electronics*, vol. 32, no. 11, pp. 8813–8822, 2017.
- [58] Z. Huang, C. Lam, P. Mak, R. P. d. S. Martins, S. Wong, and C. K. Tse, "A single-stage inductive-power-transfer converter for constant-power and maximum-efficiency battery charging," *IEEE Transactions on Power Electronics*, vol. 35, no. 9, pp. 8973–8984, 2020.
- [59] J. Fang, H. Li, Y. Tang, and F. Blaabjerg, "On the inertia of future more-electronics power systems," *IEEE Journal of Emerging and Selected Topics in Power Electronics*, vol. 7, no. 4, pp. 2130–2146, 2019.
- [60] Q. Zhong and G. Weiss, "Synchronverters: Inverters that mimic synchronous generators," *IEEE Transactions on Industrial Electronics*, vol. 58, no. 4, pp. 1259–1267, 2011.
- [61] A. Karimi, Y. Khayat, M. Naderi, T. Dragičević, R. Mirzaei, F. Blaabjerg, and H. Bevrani, "Inertia response improvement in ac microgrids: A fuzzy-based virtual synchronous generator control," *IEEE Transactions on Power Electronics*, vol. 35, no. 4, pp. 4321–4331, 2020.

- [62] S. Negri, E. Tironi, and D. Danna, “Integrated control strategy for islanded operation in smart grids: Virtual inertia and ancillary services,” *IEEE Transactions on Industry Applications*, vol. PP, pp. 1–1, 02 2019.
- [63] A. Adib and B. Mirafzal, “Virtual inductance for stable operation of grid-interactive voltage source inverters,” *IEEE Transactions on Industrial Electronics*, vol. 66, no. 8, pp. 6002–6011, 2019.
- [64] X. Meng, J. Liu, and Z. Liu, “A generalized droop control for grid-supporting inverter based on comparison between traditional droop control and virtual synchronous generator control,” *IEEE Transactions on Power Electronics*, vol. 34, no. 6, pp. 5416–5438, 2019.
- [65] E. Rakhshani and P. Rodriguez, “Inertia emulation in ac/dc interconnected power systems using derivative technique considering frequency measurement effects,” *IEEE Transactions on Power Systems*, vol. 32, no. 5, pp. 3338–3351, 2017.
- [66] T. Kerdphol, F. S. Rahman, Y. Mitani, M. Watanabe, and S. K. Küfeoğlu, “Robust virtual inertia control of an islanded microgrid considering high penetration of renewable energy,” *IEEE Access*, vol. 6, pp. 625–636, 2018.
- [67] H. Bevrani, *Robust Power System Frequency Control*, 01 2009.
- [68] W. Wu, Y. Chen, A. Luo, L. Zhou, X. Zhou, L. Yang, Y. Dong, and J. M. Guerrero, “A virtual inertia control strategy for dc microgrids analogized with virtual synchronous machines,” *IEEE Transactions on Industrial Electronics*, vol. 64, no. 7, pp. 6005–6016, July 2017.
- [69] K. Shi, H. Ye, W. Song, and G. Zhou, “Virtual inertia control strategy in microgrid based on virtual synchronous generator technology,” *IEEE Access*, vol. 6, pp. 27 949–27 957, 2018.

- [70] J. Alipoor, Y. Miura, and T. Ise, "Power system stabilization using virtual synchronous generator with alternating moment of inertia," *IEEE Journal of Emerging and Selected Topics in Power Electronics*, vol. 3, no. 2, pp. 451–458, 2015.
- [71] A. Hosseinipour and H. Hojabri, "Virtual inertia control of pv systems for dynamic performance and damping enhancement of dc microgrids with constant power loads," *IET Renewable Power Generation*, vol. 12, no. 4, pp. 430–438, 2018.
- [72] K. Knezović, S. Martinenas, P. B. Andersen, A. Zecchino, and M. Marinelli, "Enhancing the role of electric vehicles in the power grid: Field validation of multiple ancillary services," *IEEE Transactions on Transportation Electrification*, vol. 3, no. 1, pp. 201–209, March 2017.
- [73] A. Zecchino, S. D'Arco, A. G. Endegnanew, M. Korpås, and M. Marinelli, "Enhanced primary frequency control from evs: a fleet management strategy to mitigate effects of response discreteness," *IET Smart Grid*, vol. 2, no. 3, pp. 436–444, 2019.
- [74] W. Jiang, Z. Lv, Q. Zhong, B. Zeng, and G. Li, "Virtual synchronous motor based control scheme of electric vehicle charger," in *2014 International Conference on Power System Technology*, Oct 2014, pp. 2686–2692.
- [75] F. Wang, L. Zhang, X. Feng, and H. Guo, "An adaptive control strategy for virtual synchronous generator," *IEEE Transactions on Industry Applications*, vol. 54, no. 5, pp. 5124–5133, 2018.
- [76] J. A. Suul, S. D'Arco, and G. Guidi, "Virtual synchronous machine-based control of a single-phase bi directional battery charger for providing vehicle-to-grid services," *IEEE Transactions on Industry Applications*, vol. 52, no. 4,

pp. 3234–3244, 2016.

- [77] K. Dhingra and M. Singh, “Frequency support in a micro-grid using virtual synchronous generator based charging station,” *IET Renewable Power Generation*, vol. 12, no. 9, pp. 1034–1044, 2018.
- [78] A. Latif, D. C. Das, S. Ranjan, and A. K. Barik, “Comparative performance evaluation of wca-optimised non-integer controller employed with wpg–dspg–phev based isolated two-area interconnected microgrid system,” *IET Renewable Power Generation*, vol. 13, no. 5, pp. 725–736, 2019.
- [79] A. Namadmalan, “Self-oscillating pulsewidth modulation for inductive power transfer systems,” *IEEE Journal of Emerging and Selected Topics in Power Electronics*, vol. 8, no. 2, pp. 1813–1820, 2020.
- [80] W. A. Khan, S. Vahid, M. R. Rahman, R. Katebi, A. EL-Refaie, and N. Weise, “An optimized phase shifted pwm for flying capacitor multi-level converter,” in *2019 IEEE Energy Conversion Congress and Exposition (ECCE)*, 2019, pp. 5104–5108.
- [81] B. X. Nguyen, D. M. Vilathgamuwa, G. H. B. Foo, P. Wang, A. Ong, U. K. Madawala, and T. D. Nguyen, “An efficiency optimization scheme for bidirectional inductive power transfer systems,” *IEEE Transactions on Power Electronics*, vol. 30, no. 11, pp. 6310–6319, 2015.
- [82] M. Moghaddami, H. Jafari, and A. Sarwat, “Virtual inertia control of inductive electric charging system using a power transfer controller,” in *2019 IEEE Transportation Electrification Conference and Expo (ITEC)*, 2019, pp. 1–6.
- [83] M. Moghaddami, A. Anzalchi, A. Moghadasi, and A. Sarwat, “Pareto optimization of circular power pads for contactless electric vehicle battery charger,” in *2016 IEEE Industry Applications Society Annual Meeting*, 2016,

pp. 1–6.

- [84] I. Roasto and D. Vinnikov, “Analysis and evaluation of pwm and psm shoot-through control methods for voltage-fed qzsi based dc/dc converters,” in *Proceedings of 14th International Power Electronics and Motion Control Conference EPE-PEMC 2010*, 2010, pp. T3–100–T3–105.
- [85] S. Samanta and A. K. Rathore, “A new inductive power transfer topology using direct ac–ac converter with active source current waveshaping,” *IEEE Transactions on Power Electronics*, vol. 33, no. 7, pp. 5565–5577, 2018.
- [86] A. D. Arioni, T. S. Padilha, and S. V. G. Oliveira, “Expanded space vector modulation of direct matrix converters including hidden rotating pairs,” *IEEE Transactions on Industrial Electronics*, vol. 66, no. 11, pp. 8296–8307, 2019.
- [87] H. Jafari, M. Moghaddami, T. O. Olowu, A. Sarwat, and M. Mahmoudi, “Virtual inertia-based multi-power level controller for inductive electric vehicle charging systems,” *IEEE Journal of Emerging and Selected Topics in Power Electronics*, pp. 1–1, 2020.
- [88] M. Moghaddami and A. I. Sarwat, “Single-phase soft-switched ac–ac matrix converter with power controller for bidirectional inductive power transfer systems,” *IEEE Transactions on Industry Applications*, vol. 54, no. 4, pp. 3760–3770, 2018.
- [89] H. L. Li, A. P. Hu, and G. A. Covic, “A direct ac–ac converter for inductive power-transfer systems,” *IEEE Transactions on Power Electronics*, vol. 27, no. 2, pp. 661–668, 2012.
- [90] H. Jafari, M. Moghaddami, T. O. Olowu, A. Sarwat, and M. Mahmoudi, “Virtual inertia-based multi-power level controller for inductive electric vehicle charging systems,” *IEEE Journal of Emerging and Selected Topics in*

Power Electronics, pp. 1–1, 2020.

- [91] M. Moghaddami, H. Jafari, and A. Sarwat, “Virtual inertia control of inductive electric charging system using a power transfer controller,” in *2019 IEEE Transportation Electrification Conference and Expo (ITEC)*, 2019, pp. 1–6.
- [92] H. Hu, T. Cai, S. Duan, X. Zhang, J. Niu, and H. Feng, “An optimal variable frequency phase shift control strategy for zvs operation within wide power range in ipt systems,” *IEEE Transactions on Power Electronics*, vol. 35, no. 5, pp. 5517–5530, 2020.
- [93] Z. Zhang, W. Ai, Z. Liang, and J. Wang, “Topology-reconfigurable capacitor matrix for encrypted dynamic wireless charging of electric vehicles,” *IEEE Transactions on Vehicular Technology*, vol. 67, no. 10, pp. 9284–9293, 2018.
- [94] J. Zhang, J. Zhao, Y. Zhang, and F. Deng, “A wireless power transfer system with dual switch-controlled capacitors for efficiency optimization,” *IEEE Transactions on Power Electronics*, vol. 35, no. 6, pp. 6091–6101, 2020.
- [95] D.-H. Kim, S. Kim, S.-W. Kim, J. Moon, I. Cho, and D. Ahn, “Coupling extraction and maximum efficiency tracking for multiple concurrent transmitters in dynamic wireless charging,” *IEEE Transactions on Power Electronics*, vol. 35, no. 8, pp. 7853–7862, 2020.
- [96] Z. Zhang and H. Pang, “Continuously adjustable capacitor for multiple-pickup wireless power transfer under single-power-induced energy field,” *IEEE Transactions on Industrial Electronics*, vol. 67, no. 8, pp. 6418–6427, 2020.
- [97] E. Abramov and M. M. Peretz, “Multi-loop control for power transfer regulation in capacitive wireless systems by means of variable matching networks,” *IEEE Journal of Emerging and Selected Topics in Power Electronics*, vol. 8,

no. 3, pp. 2095–2110, 2020.

- [98] M. Moghaddami, A. Anzalchi, and A. I. Sarwat, “Single-stage three-phase ac–ac matrix converter for inductive power transfer systems,” *IEEE Transactions on Industrial Electronics*, vol. 63, no. 10, pp. 6613–6622, 2016.
- [99] H. Jafari, T. O. Olowu, M. Mahmoudi, M. Moghaddami, and A. Sarwat, “Comparison analysis of bipolar and double d-shape configurations in inductive power transfer electric vehicle chargers,” in *2021 IEEE Power Energy Society Innovative Smart Grid Technologies Conference (ISGT)*, 2021, pp. 1–5.
- [100] V. Jiwariyavej, T. Imura, and Y. Hori, “Coupling coefficients estimation of wireless power transfer system via magnetic resonance coupling using information from either side of the system,” *IEEE Journal of Emerging and Selected Topics in Power Electronics*, vol. 3, no. 1, pp. 191–200, March 2015.
- [101] L. Liu, Q. Li, L. Liu, and X. Yuan, “Parameter identification of wireless power transfer system using parallel chaos optimization algorithm,” in *2017 Chinese Automation Congress (CAC)*, Oct 2017, pp. 7549–7554.
- [102] K. Hata, T. Imura, and Y. Hori, “Simultaneous estimation of primary voltage and mutual inductance based on secondary-side information in wireless power transfer systems,” in *2016 IEEE Wireless Power Transfer Conference (WPTC)*, May 2016, pp. 1–3.
- [103] M. Iordache, L. Iordache, R. G. Voiculescu, L. Dumitriu, and L. Mandache, “Parameter estimation of magnetic coupled resonators used in power wireless transfer,” in *2014 International Conference on Applied and Theoretical Electricity (ICATE)*, Oct 2014, pp. 1–6.
- [104] X. Dai, X. Li, and Y. Li, “Cross-coupling coefficient estimation between multi-receivers in wpt system,” in *2017 IEEE PELS Workshop on Emerging*

Technologies: Wireless Power Transfer (WoW), 2017, pp. 1–4.

- [105] J. Schneider, “Sae j2954 overview and path forward,” 2013.
- [106] M. Moghaddami and A. I. Sarwat, “Single-phase soft-switched ac–ac matrix converter with power controller for bidirectional inductive power transfer systems,” *IEEE Transactions on Industry Applications*, vol. 54, no. 4, pp. 3760–3770, July 2018.
- [107] M. Moghaddami, H. Jafari, and A. Sarwat, “Virtual inertia control of inductive electric charging system using a power transfer controller,” in *2019 IEEE Transportation Electrification Conference and Expo (ITEC)*, 2019, pp. 1–6.
- [108] H. Jafari, M. Mahmoudi, T. O. Olowu, and A. Sarwat, “Multi-level power controller design for dynamic wireless electric vehicle charging systems,” in *2020 IEEE Transportation Electrification Conference Expo (ITEC)*, 2020, pp. 986–991.
- [109] P. Darvish, S. Mekhilef, and H. A. Illias, “A novel s-s-lclcc compensation for three-coil wpt to improve misalignment and energy efficiency stiffness of wireless charging system,” *IEEE Transactions on Power Electronics*, pp. 1–1, 2020.
- [110] J. Zhang, X. Yuan, C. Wang, and Y. He, “Comparative analysis of two-coil and three-coil structures for wireless power transfer,” *IEEE Transactions on Power Electronics*, vol. 32, no. 1, pp. 341–352, 2017.
- [111] S. Moon, B. Kim, S. Cho, and G. Moon, “Analysis and design of wireless power transfer system with an intermediate coil for high efficiency,” in *2013 IEEE ECCE Asia Downunder*, 2013, pp. 1034–1040.
- [112] M. Budhia, J. T. Boys, G. A. Covic, and C. Huang, “Development of a

- single-sided flux magnetic coupler for electric vehicle ipt charging systems,” *IEEE Transactions on Industrial Electronics*, vol. 60, no. 1, pp. 318–328, 2013.
- [113] M. Budhia, G. A. Covic, and J. T. Boys, “Design and optimization of circular magnetic structures for lumped inductive power transfer systems,” *IEEE Transactions on Power Electronics*, vol. 26, no. 11, pp. 3096–3108, 2011.
- [114] S. Y. R. Hui and W. C. Ho, “A new generation of universal contactless battery charging platform for portable consumer electronic equipment,” in *2004 IEEE 35th Annual Power Electronics Specialists Conference (IEEE Cat. No.04CH37551)*, vol. 1, 2004, pp. 638–644 Vol.1.
- [115] J. Pries, V. P. N. Galigekere, O. C. Onar, and G. Su, “A 50-kw three-phase wireless power transfer system using bipolar windings and series resonant networks for rotating magnetic fields,” *IEEE Transactions on Power Electronics*, vol. 35, no. 5, pp. 4500–4517, 2020.
- [116] F. Pijl, M. Castilla, and P. Bauer, “Adaptive sliding-mode control for a multiple-user inductive power transfer system without need for communication,” *Industrial Electronics, IEEE Transactions on*, vol. 60, pp. 271–279, 01 2013.
- [117] J. T. Boys, G. A. Covic, and A. W. Green, “Stability and control of inductively coupled power transfer systems,” *IEE Proceedings - Electric Power Applications*, vol. 147, no. 1, pp. 37–43, Jan 2000.
- [118] Chwei-Sen Wang, O. H. Stielau, and G. A. Covic, “Design considerations for a contactless electric vehicle battery charger,” *IEEE Transactions on Industrial Electronics*, vol. 52, no. 5, pp. 1308–1314, 2005.
- [119] M. G. S. Pearce, G. A. Covic, and J. T. Boys, “Robust ferrite-less double d topology for roadway ipt applications,” *IEEE Transactions on Power*

Electronics, vol. 34, no. 7, pp. 6062–6075, 2019.

- [120] J. T. Boys, G. A. Covic, and A. W. Green, “Stability and control of inductively coupled power transfer systems,” *IEE Proceedings - Electric Power Applications*, vol. 147, no. 1, pp. 37–43, 2000.
- [121] J. Lin, R. Saunders, K. Schulmeister, P. Söderberg, B. Stuck, A. Swerdlow, M. Taki, B. Veyret, G. Ziegelberger, M. Repacholi, R. Matthes, A. Ahlbom, K. Jokela, and C. Roy, “Icnirp guidelines for limiting exposure to time-varying electric and magnetic fields (1 hz to 100 khz).” *Health Phys.*, vol. 99, 01 2010.
- [122] M. Moghaddami, A. Anzalchi, and A. Sarwat, “Single-stage three-phase ac-ac matrix converter for inductive power transfer systems,” *IEEE Transactions on Industrial Electronics*, vol. 63, pp. 6613 – 6622, 05 2016.
- [123] H. Jafari, M. Moghaddami, T. O. Olowu, A. Sarwat, and M. Mahmoudi, “Virtual inertia-based multi-power level controller for inductive electric vehicle charging systems,” *IEEE Journal of Emerging and Selected Topics in Power Electronics*, pp. 1–1, 2020.
- [124] H. Jafari, T. O. Olowu, M. Mahmoudi, and A. Sarwat, “Optimal design of ipt bipolar power pad for roadway-powered ev charging systems,” *IEEE Canadian Journal of Electrical and Computer Engineering*, vol. 44, no. 3, pp. 350–355, 2021.
- [125] N. Rasekh, J. Kavianpour, and M. Mirsalim, “A novel integration method for a bipolar receiver pad using lcc compensation topology for wireless power transfer,” *IEEE Transactions on Vehicular Technology*, vol. 67, no. 8, pp. 7419–7428, 2018.
- [126] M. Mahmoudi, A. Fatehi, H. Jafari, and E. Karimi, “Multi-objective micro-grid design by nsga-ii considering both islanded and grid-connected modes,”

- in *2018 IEEE Texas Power and Energy Conference (TPEC)*, 2018, pp. 1–6.
- [127] C. R. Sullivan, “Optimal choice for number of strands in a litz-wire transformer winding,” *IEEE Trans. Power Electron.*, vol. 14, no. 2, pp. 283–291, Mar 1999.
- [128] K. Ishibashi, “Eddy current analysis by boundary element method utilizing impedance boundary condition,” *IEEE Transactions on Magnetics*, vol. 31, no. 3, pp. 1500–1503, 1995.
- [129] *Wireless Power Transfer for Light-Duty Plug-In/Electric Vehicles and Alignment Methodology*, nov 2017. [Online]. Available: https://doi.org/10.4271/J2954_201711
- [130] M. Budhia, G. Covic, and J. Boys, “Design and optimization of circular magnetic structures for lumped inductive power transfer systems,” *IEEE Trans. Power Electron.*, vol. 26, no. 11, pp. 3096–3108, Nov 2011.
- [131] Z. Pantic, S. Bai, and S. M. Lukic, “Zcs lcc -compensated resonant inverter for inductive-power-transfer application,” *IEEE Trans. Ind. Electron.*, vol. 58, no. 8, pp. 3500–3510, Aug 2011.
- [132] H. Jafari, M. Moghaddami, and A. Sarwat, “Foreign object detection in inductive charging systems based on primary side measurements,” *IEEE Transactions on Industry Applications*, vol. PP, pp. 1–1, 08 2019.
- [133] F. Lu, H. Zhang, H. Hofmann, and C. Mi, “A double-sided lclc-compensated capacitive power transfer system for electric vehicle charging,” *Power Electronics, IEEE Transactions on*, vol. 30, pp. 6011–6014, 11 2015.
- [134] J. Deng, F. Lu, S. Li, T. D. Nguyen, and C. Mi, “Development of a high efficiency primary side controlled 7kw wireless power charger,” *2014 IEEE International Electric Vehicle Conference, IEVC 2014*, 03 2015.

- [135] M. Castilla, L. G. de Vicuna, J. M. Guerrero, J. Matas, and J. Miret, “Sliding-mode control of quantum series-parallel resonant converters via input-output linearization,” *IEEE Trans. Ind. Electron.*, vol. 52, no. 2, pp. 566–575, April 2005.
- [136] X. Zhang, Z. Yuan, Q. Yang, Y. Li, J. Zhu, and Y. Li, “Coil design and efficiency analysis for dynamic wireless charging system for electric vehicles,” *IEEE Transactions on Magnetics*, vol. 52, pp. 1–1, 07 2016.
- [137] S. Zhou and C. Mi, “Multi-paralleled lcc reactive power compensation networks and its tuning method for electric vehicle dynamic wireless charging,” *IEEE Transactions on Industrial Electronics*, vol. 63, pp. 1–1, 01 2015.
- [138] M. Moghaddami, H. Jafari, and A. Sarwat, “Virtual inertia control of inductive electric charging system using a power transfer controller,” in *2019 IEEE Transportation Electrification Conference and Expo (ITEC)*, June 2019, pp. 1–6.
- [139] R. Mai, B. Yang, Y. Chen, N. Yang, Z. He, and S. Gao, “A misalignment tolerant ipt system with intermediate coils for constant-current output,” *IEEE Transactions on Power Electronics*, vol. 34, no. 8, pp. 7151–7155, 2019.
- [140] Y. Chen, R. Mai, Y. Zhang, M. Li, and Z. He, “Improving misalignment tolerance for ipt system using a third-coil,” *IEEE Transactions on Power Electronics*, vol. 34, no. 4, pp. 3009–3013, 2019.
- [141] Y. Yao, Y. Wang, X. Liu, Y. Pei, D. Xu, and X. Liu, “Particle swarm optimization-based parameter design method for s/cle-compensated ipt systems featuring high tolerance to misalignment and load variation,” *IEEE Transactions on Power Electronics*, vol. 34, no. 6, pp. 5268–5282, 2019.
- [142] V. Z. Barsari, D. J. Thrimawithana, and G. A. Covic, “An inductive coupler

- array for in-motion wireless charging of electric vehicles,” *IEEE Transactions on Power Electronics*, vol. 36, no. 9, pp. 9854–9863, 2021.
- [143] A. S. Jurkov, A. Radomski, and D. J. Perreault, “Tunable matching networks based on phase-switched impedance modulation1,” *IEEE Transactions on Power Electronics*, vol. 35, no. 10, pp. 10 150–10 167, 2020.
- [144] C. Liu, D. J. Thrimawithana, G. A. Covic, and M. Kesler, “Active impedance control for inductive charging of electric vehicles,” in *2020 IEEE PELS Workshop on Emerging Technologies: Wireless Power Transfer (WoW)*, 2020, pp. 16–20.
- [145] M. Moghaddami and A. Sarwat, “Self-tuning variable frequency controller for inductive electric vehicle charging with multiple power levels,” *IEEE Transactions on Transportation Electrification*, vol. 3, no. 2, pp. 488–495, 2017.
- [146] M. Moghaddami, A. Sundararajan, and A. I. Sarwat, “A power-frequency controller with resonance frequency tracking capability for inductive power transfer systems,” *IEEE Transactions on Industry Applications*, vol. 54, no. 2, pp. 1773–1783, 2018.
- [147] J. Dai and D. C. Ludois, “A survey of wireless power transfer and a critical comparison of inductive and capacitive coupling for small gap applications,” *IEEE Transactions on Power Electronics*, vol. 30, no. 11, pp. 6017–6029, 2015.
- [148] B. Lee, M. Kiani, and M. Ghovanloo, “A triple-loop inductive power transmission system for biomedical applications,” *IEEE Transactions on Biomedical Circuits and Systems*, vol. 10, no. 1, pp. 138–148, 2016.
- [149] Y. Lim, H. Tang, S. Lim, and J. Park, “An adaptive impedance-matching network based on a novel capacitor matrix for wireless power transfer,” *IEEE*

Transactions on Power Electronics, vol. 29, no. 8, pp. 4403–4413, 2014.

- [150] T. C. Beh, M. Kato, T. Imura, S. Oh, and Y. Hori, “Automated impedance matching system for robust wireless power transfer via magnetic resonance coupling,” *IEEE Transactions on Industrial Electronics*, vol. 60, no. 9, pp. 3689–3698, 2013.

- [151] H. Li, J. Li, K. Wang, W. Chen, and X. Yang, “A maximum efficiency point tracking control scheme for wireless power transfer systems using magnetic resonant coupling,” *IEEE Transactions on Power Electronics*, vol. 30, no. 7, pp. 3998–4008, 2015.

- [152] T.-D. Yeo, D. Kwon, S.-T. Khang, and J.-W. Yu, “Design of maximum efficiency tracking control scheme for closed-loop wireless power charging system employing series resonant tank,” *IEEE Transactions on Power Electronics*, vol. 32, no. 1, pp. 471–478, 2017.

VITA
HASSAN JAFARI

Born in, Tarom, Zanjan, Iran

- 2008 B.Sc., Electrical and Computer Engineering
University of Tabriz, Tabriz City
Iran
- 2010 M.Sc., Electrical and Computer Engineering
Amirkabir University of Technology, Tehran City
Iran
- 2021 PhD, Electrical Engineering
Florida International University, Miami, FL
Miami, United States

PUBLICATIONS AND PRESENTATIONS

1. H. Jafari, T. O. Olowu, M. Mahmoudi and A. Sarwat, "Optimal Design of IPT Bipolar Power Pad for Roadway-Powered EV Charging Systems," in IEEE Canadian Journal of Electrical and Computer Engineering, vol. 44, no. 3, pp. 350-355, Summer 2021, doi: 10.1109/ICJECE.2021.3075639.
2. H. Jafari, T. O. Olowu, M. Moghaddami and A. Sarwat, "An Accurate On-line Parameter Estimation Technique for Inductive Electric Vehicle Charging Systems," 2021 IEEE Transportation Electrification Conference and Expo (ITEC), 2021.
3. H. Jafari, T. O. Olowu, M. Mahmoudi and A. Sarwat, "AC-AC Matrix Converter Using Lookup-Based PWM for Inductive Power Transfer Systems" in IEEE Transportation Electrification Conference and Expo (ITEC), 2021 .
4. H. Jafari, T. O. Olowu, M. Mahmoudi and A. Sarwat, "Optimal Design of Bipolar Power Pad for Dynamic Inductive Electric Vehicle Charging Systems" in IEEE Transportation Electrification Conference and Expo (ITEC), 2021.
5. T. O. Olowu, H. Jafari, and A. Sarwat, "Voltage Controlled Resonant DC/DC Converter for Solid State Transformer Applications" in IEEE Transportation Electrification Conference and Expo (ITEC), 2021.
6. T. O. Olowu, H. Jafari, I. Pierano, and A. Sarwat, "Parasitic Parameter Analysis of High Frequency Transformer for Series Resonant Converter with Experimental Validation" in IEEE Transportation Electrification Conference and Expo (ITEC), 2021.
7. T. O. Olowu, H. Jafari, M. Moghaddami and A. I. Sarwat, "Multiphysics and Multiobjective Design Optimization of High-Frequency Transformers for Solid-State Transformer Applications," in IEEE Transactions on Industry Applications, vol. 57, no. 1, pp. 1014-1023, Jan.-Feb. 2021.

8. T. O. Olowu, H. Jafari, and A. Sarwat, "Multiphysics-based Design Optimization of Medium Frequency Transformer with Experimental Validation" in The Applied Power Electronics Conference (APEC) 2021.
9. T. O. Olowu, H. Jafari, M. Moghaddami and A. I. Sarwat, "Multiphysics and Multiobjective Design Optimization of High-Frequency Transformers for Solid-State Transformer Applications," in IEEE Transactions on Industry Applications, vol. 57, no. 1, pp. 1014-1023, Jan.-Feb. 2021
10. H. Jafari, M. Moghaddami, T. O. Olowu, A. Sarwat and M. Mahmoudi, "Virtual Inertia-Based Multi-Power Level Controller for Inductive Electric Vehicle Charging Systems," in IEEE Journal of Emerging and Selected Topics in Power Electronics, doi: 10.1109/JESTPE.2020.3032898
11. T. O. Olowu, S. Dharmasena, H. Jafari and A. Sarwat, "Investigation of False Data Injection Attacks on Smart Inverter Settings," 2020 IEEE CyberPELS (CyberPELS), 2020
12. H. Jafari, M. Mahmoudi, T. O. Olowu and A. Sarwat, "Multi-Level Power Controller Design for Dynamic Wireless Electric Vehicle Charging Systems," 2020 IEEE Transportation Electrification Conference and Expo (ITEC), 2020
13. H. Jafari, T. O. Olowu, M. Mahmoudi and A. Sarwat, "Design and Implementation of Estimating Algorithm for Foreign Object Location in Wireless Charging EV Systems," 2020 IEEE Applied Power Electronics Conference and Exposition (APEC), 2020
14. H. Jafari, M. Moghaddami and A. I. Sarwat, "Foreign Object Detection in Inductive Charging Systems Based on Primary Side Measurements," in IEEE Transactions on Industry Applications, vol. 55, no. 6, pp. 6466-6475, Nov.-Dec. 2019
15. M. Moghaddami, H. Jafari and A. Sarwat, "Virtual Inertia Control of Inductive Electric Charging System Using a Power Transfer Controller," 2019 IEEE Transportation Electrification Conference and Expo (ITEC), 2019.
16. H. Jafari, and A. Sarwat, "Resonant AC-AC Converter with Phase Modulation Based Power Controller for IPT Systems", IEEE Journal of Emerging and Selected Topics in Power Electronics (submitted)
17. H. Jafari, and A. Sarwat, "Resonant AC-AC Converter with Multi-Power Level Controller for Inductive EV Charging Systems", IEEE Transactions on Vehicular Technology (submitted)